Application of microwave sidebands from an optically injected diode laser to atomic physics and the construction of a magnetic trap for neutral atoms.

Laidler, Christopher I

Swansea University
Prifysgol Abertawe

SWANSEA UNIVERSITY

PHD. THESIS

Application of Microwave Sidebands from an Optically Injected Diode Laser to Atomic Physics and the Construction of a Magnetic Trap for Neutral Atoms

Author:
Christopher I. LAIDLER

Supervisor:
Dr. Stefan ERIKSSON

Submitted to Swansea University in fulfilment of the requirements for the Degree of Doctor of Philosophy

May 2013

Abstract

Optically injected diode lasers produce a diverse range of non-linear dynamics. One of these dynamics - the period one oscillation - is demonstrated as a useful tool for atomic physics experiments by using the two frequencies that result to create a magneto-optical trap in rubidium. Other applications are also discussed.
In the second part of this thesis progress towards the creation of a cold atoms experiment is described with the successful construction of a magnetic trap for ^{87}Rb atoms.
Construction methods for both experiments are also described.

Declarations

This work has not previously been accepted in substance for any degree and is not being concurrently submitted in candidature for any degree.

Signed... ..... Date 17/5/13

This thesis is the result of the author's own investigations, except where otherwise stated and other sources are acknowledged by explicit references for which a bibliography is appended.

Signed.. ..... Date 17/5/13

Consent is given by the author for this thesis, to be available for photocopying and for inter-library loan, and for the title and abstract to be made available to outside organisations.

Signed.. ..... Date 17/5/13

Contents

Acknowledgements

First and foremost my thanks go to Stefan Eriksson who supervised and guided me through this work. I was extremely lucky to have a supervisor who always had time to discuss plans and problems, and who was always around to help me out when I was stuck. I have also learnt a great deal from you.

Thanks to Rhys Jenkins, who only joined in the last six months of my work in the lab, but your help was the last push I needed to get the magnetic trap to work, it was also great to have another person to bounce ideas off and I hope you have learnt things from me in return.

To Julian Kivell, I really appreciate your advise on materials and designs and also the time you spent manufacturing parts for me, most notably the G10 components which I realise are not pleasant to machine and took many hours work. Also thanks for your assistance winding coils - although I have to admit I quite enjoyed doing this! Also thanks to Hugh Thomas for loan of equipment, mechanical and electronic advice, and for machining some parts for me.

For loan of other equipment and miscellaneous advice thanks to Will Bryan, Dirk van der Werf, Mike Charlton, Graham Shore and Helmut Telle.

Thanks to my mum and dad (and their associated bank) for their moral and financial support over the last few years, loans with negative interest rates were much appreciated and I would not be where I am today without the nudges in the right direction you have given me throughout my life. Thanks to my friends for their support of whom there are too many to name but most notably to Jeni, Chris, Rhodri and Becky.

Finally to Hannah for being my rock(!) for the last couple of years and for getting me through several tough periods. However, despite your best efforts, and a fantastic trip to see the geology of Torridon, I'm afraid I remain a Physicist.

List of Figures

Chapter 1

Introduction

1.1 A Bit of History

1.1.1 Lasers and Laser Injection Effects

In 1865 Christian Huygens observed that two wall clock pendulums would 'lock' to asynchronous motion of one another when placed close together on the same wall, but they would remain independent if one clock was moved away from the other. Huygens suggested that small movements in the beam from which the clocks were hung facilitated the effect and this was demonstrated to be correct in 2002 [1]. Huygens' observation is generally accepted as the first recorded study of oscillators phase locking together. The phase (or anti-phase in the case of reference [1]) locking phenomena discovered by Huygens was not employed in any useful application until the 1940s when electronic communications explored the use of phase locking in frequency modulated (FM) receivers [2, 3]. The first to mathematically describe the phenomena in detail was Robert Adler in 1946 [4].

The mid 20th century also saw the development of the laser system which had been hypothesised since Einstein had predicted stimulated emission of radiation by atoms [5]. This theory described how an atom in an excited state could be stimulated into emitting a photon and falling to a lower state by a passing photon with energy corresponding to the difference between the excited and lower state energies. For light amplification to occur a population inversion needs to be obtained. The most obvious pumping method was absorption of radiation but this would also induce stimulated emission, hence, for a two level system, it was impossible to pump more than 50% of the population into a higher level due to saturation.

In 1955 Gordon, Zeiger and Townes successfully overcame this problem with their 'MASER', Microwave Amplification by Stimulated Emission of Radiation [6]. They overcame the population inversion problem by using an electrostatic lens which would selectively focus ammonia atoms in the excited state and this focussed atomic beam could then be used as a gain medium. For their work related to MASERs Charles Townes, Nicolay Basov and Aleksandr Prokhorov were awarded the 1964 Nobel prize.

Many scientists including Gordon Gould, Charles Townes & Arthur Schawlow [7] and Theodore Maiman [8] attempted to develop the idea for the visible spectrum and the 'LASER' (Light Amplification by Stimulated Emission of Radiation) was given its name by Gordon Gould in his notebook [9]. The design of the laser was a (Fabry Perot) laser cavity with two mirrors at each end and a gain medium which could be pumped through transparent walls.

Theodore Maiman built on the theoretical work of Schawlow and Townes [7] to produce the first 3 level ruby laser [8] - solving the problem of optical pumping above population inversion threshold by pumping the gain medium on a different transition to lasing. This was made more efficient with the invention of the four level laser by Sorokin and Stevenson in 1960 [10] where the ground state of the pumping is not the ground state for lasing making a population inversion obtainable without having to pump more than 50% of the atoms to an excited state. This opened the door for lasers to be constructed from any medium where a four level system could be pumped to give a population inversion.

In 1962 R. N. Hall successfully used a p-n junction as a laser [11]. An electric current passing over the junction injects electrons and holes from the n and p type layers causing a population inversion in a transition region which forms the gain medium. This was improved upon over the next few years to finally give the hetero-junction laser which could be operated at room temperature [12]. Many other substances and materials can be used as a gain medium such as Ruby, Dye or various gasses. For the purpose of this thesis we will focus mainly on the laser diode.

With science now able to build lasers some attention was turned to studying the devices themselves and the dynamics which occur within the laser cavity.

In 1966 H. L. Stover and W. H. Steier became the first to couple two lasers together by injecting the beam from one (master) laser into another (slave) laser [13] and they observed that 'laser locking' occurred. When laser locking occurs the phase and frequency of the slave laser jumps to that of the master laser. This was expected

and can be predicted using Adler's equation which describes the coupling of two oscillators [4]. For a master oscillation of frequency ω_1 and oscillation amplitude E_1 coupled to a slave oscillation (ω_0 and E_0) the Adler equation can be written in the form [14],

$$\frac{d\phi(t)}{dt} + \omega_1 - \omega_0 = -\gamma_e \frac{E_1}{E_0} \sin\phi(t) = -\omega_m \sin\phi(t) \tag{1.1}$$

where $\phi(t)$ is the phase between the two oscillations, and γ_e is the coupling rate between the two oscillations. For the case where the oscillations become locked to the same phase (injection locked) we can neglect the first term because $d\phi/dt = 0$. We also know that $-1 \leq \sin(\phi(t)) \leq 1$ and hence equation (1.1) reduces to

$$-\omega_m \leq (\omega_1 - \omega_0) \leq \omega_m \tag{1.2}$$

This gives the locking bandwidth range which is described by ω_m.
Here it is worth noting a convention used throughout this thesis for frequency where the injection frequency ω_i is given as the difference between the master and slave oscillator frequencies ω_{MO} and ω_{SO} as

$$\omega_i = \omega_{MO} - \omega_{SO} \tag{1.3}$$

A consequence of this is that the injection frequency can appear negative.
Research into the full potential of optical injection in laser diodes did not gain momentum until the 1980's when research groups started to study the non-linear dynamics which also result. Reference [15] demonstrated the laser behaviour when an external mirror reflected light back into the laser diode, and the resulting external cavity caused undulations in the laser's output intensity as the laser current was increased or decreased. The undulations were caused by the mirror providing optical feedback which was optimised when the cavity length was equal to a multiple of the laser wavelength, causing a peak in laser output power and dips in the output power when the cavity was sub-optimal for the wavelength. They also note how the relaxation oscillation (see section 2.1.1) of the laser is enhanced when the external cavity is de-optimised for the lasing wavelength and suppressed when the cavity is optimised. This study would lead on to classify the different dynamics which occur in an optically injected laser diode, such as periodic oscillations which could lead to chaos [16], these phenomena are explained in more detail in section 2.1.2. Regions of modulation had previously been observed [17].

Many other examples of these dynamics, in particular the locking of coupled oscillators, have been observed in coupled oscillator systems across all branches of science, for example in the locking of electronic oscillators [4] or in neuroscience [18].
Analytical models have been used to characterise these dynamics in lasers, [19, 20, 21, 22] and maps such as references [23, 24, 25] can be used to predict for which controllable parameters they will occur.
Studies have resulted in the discovery of many new techniques and applications such as chaos synchronisation [26, 27, 28] and photonics applications resulting from microwave beat frequencies generated by the period one state (which is explained in more detail in section 2.1.1) [29, 30]. Reference [30] was published during the course of this work and is explained in this thesis in more detail.

1.1.2 Laser Cooling and Trapping

Since the early days of the laser it had always been known that coherent narrow linewidth laser light would be a useful tool for spectroscopy [6]. The tuneable, coherent, narrow linewidth nature of laser light makes it ideal for exciting single transitions within atomic species. The possibility that this light could also be used for cooling was suggested in 1975 by Hänsch and Schawlow [31] and Wineland and Dehmelt [32]. The motivation for creating cold atoms was to remove the atomic Doppler linewidth broadening caused by temperature, this would enable many hyperfine transitions to be studied and would generally improve spectroscopic techniques. The first traps for cold atoms were realised in 1978 [33, 34] when magnesium ions held in a Penning trap were successfully cooled to below 40 K, and Barium ions held in an RF Paul trap were observed to be cooled by lasers. However, up until now only ions confined in ion traps were used, and the lasers were used only to provide cooling. Theories of how to trap and cool using just optical techniques were being developed, these techniques would enable neutral atoms to also be cooled because the trapping force would be provided by the photon recoil force [35].
The first observation of slowing an atomic beam of neutral atoms by lasers was in 1981 [36], a single laser beam provided radiation force to decelerate a sodium beam to 1.5 K. This was closely followed in 1982 by Phillips and Metcalf [37], who later also reported the 'stopping' of atoms with laser light [38]. Unlike reference [36], they used a tapered solenoid to create a spatially varying magnetic field and hence a spatially varying Zeeman shift which compensated for the decreasing Doppler shift

as the atoms slowed. This prevented the atoms Doppler shifting away from the red-detuned trap laser. However this still only decelerated in one dimension and 'stopped' atoms were in fact atoms with a temperature of less than 100 mK.

The obvious extension to this was to slow the sodium atoms in all three spatial dimensions in a so-called optical molasses. In 1985 Steven Chu and his team at Bell Laboratories reported the 'viscous confinement and cooling of neutral sodium atoms in three dimensions' [39]. Six beams intersected with a pre-cooled beam of atomic sodium and created a cloud consisting of slow moving atoms which had been cooled to a few hundred microkelvin. Whilst not strictly trapped because the atoms could slowly move outside the trapping area by a 'random walk' they were moving slow enough to remain in the beam intersection for significant time.

Meanwhile the first purely magnetic trap was used to confine neutral sodium atoms [40]. A beam of atoms was slowed in one dimension by the laser cooling technique and at the point where the atoms almost stopped they were loaded into a magnetic trap which uses a quadrupole field created from two anti-Helmholtz coils. In an inhomogeneous magnetic field atoms with magnetic sub-level m_F equal to zero are untrapped and feel no force, atoms with $g_F m_F < 0$ feel a force in the direction of the positive field gradient and are hence called high field seeking states, and atoms with $g_F m_F > 0$ feel a force opposed to the field gradient and are hence called low field seeking states. Here g_F is the Landé g-factor. In a quadrupole field low field seeking atoms will move towards the centre where the field is at a minimum, see section 3.2.2 for more details on magnetic trapping. Reference [40] cleverly used the slowing beam to also pump the atoms into low field seeking states using σ^+ polarised light.

The first true optical trap came in 1986 [41]. Atoms were pre-cooled using an optical molasses and loaded into a shallow optical trap formed by the focussing of a laser beam. The dipole force F_{Dipole} on an atom due to light of intensity I is created by the a.c. Stark shift (shift in atomic energy levels due to an electric field). Light of frequency ω is detuned from a nearby atomic transition of frequency ω_0, linewidth Γ and saturation intensity I_{sat} by $\delta = \omega - \omega_0$. This gives a dipole force of [42]:

$$\begin{aligned} F_{Dipole} &= -\nabla U_{Dipole} \\ U_{Dipole} &\backsimeq \frac{\hbar \Gamma^2 I}{8 \delta I_{sat}} \end{aligned} \tag{1.4}$$

A focussed laser beam creates a local maximum in $\frac{I}{I_{sat}}$, and by choosing the detuning to be either negative or positive (red or blue), we can create a force which either points towards or away from the focal point. Hence a trap is created in the focus of a beam when δ is negative. It is also possible to trap atoms in a local minimum when δ is positive.

Finally in 1987 the first trap was created which combined a Zeeman shift with an optical molasses to trap atoms for many seconds, and cool them to a few hundred microkelvin [43]. This was the magneto-optical trap (MOT) or Zeeman optical trap (ZOT) as it was often called initially. The six molasses lasers were circularly polarised and a quadrupole magnetic field applied which was zero at the trap centre and increased radially. The magnetic field creates a Zeeman shift to the magnetic sub-levels of an atom: if the atom drifts away from the centre of the trap, the magnetic field creates a Zeeman shift which would bring the atom closer to resonance with the circulary polarised counter-propagating laser beam (see section 2.1.6 for more detail). Typically the magnetic field gradient in a magnetic trap is around ten times that of a MOT, however they rely on the relatively weak force produced by the alignment of the atoms magnetic moment which in one dimension is given by $F_{zBtrap} = -g_F \mu_B m_F \frac{dB}{dz}$. The trapping force in the MOT (F_{MOT}) is due to radiation pressure from the scattering force F_{Scatt} and depends on the atoms velocity v, detuning and the magnetic field, $F_{MOT} = -2\frac{dF_{Scatt}}{d\omega}(kv + \frac{g\mu_B}{\hbar}\frac{dB}{dz}z)$. The capture velocity for a MOT depends on the size of the laser beams but is typically several tens of m/s [42]. Large capture velocities make it easy for a MOT to be loaded from room temperature vapour, the atoms are instantly cooled to the microkelvin regime - this works particularly well with the heavier and slower alkali atoms rubidium and caesium. Monroe *et al.* [44] created the first MOT to be loaded directly from atoms in a vapour cell and this was improved upon over the years to a MOT which could load 10^{10} atoms [45]. Today the simplicity and effectiveness of the MOT makes it the first step for many laser cooling experiments.

The first temperature measurements of MOTs and optical mollasses were done by the so-called release and recapture method. The trap was momentarily switched off, allowing the atom cloud to thermally expand, and then switched on again some variable time afterwards reloading the MOT from the expanded cloud. The difference in the number of atoms in the re-loaded MOT compared to the initial MOT would enable the determination of the number of atoms which had remained in the trapping region during the switch off time, and calculation of the mean velocity

distribution of the atoms and hence their temperature. When the first MOTs were created this was the main technique used and it yielded temperatures around the predicted 'Doppler cooling limit' but with a large uncertainty. During Doppler cooling an atom repeatedly absorbs and emits a photon. The recoil force on an atom from each spontaneous emission of a photon occurs in random directions, this causes a diffusion of the atomic velocity and hence heating. There are also fluctuations in the absorption and emission rates in time which also lead to heating. Hence, (it was thought in 1988,) this energy limit given by $E_{Dopplerlimit} = k_B T_D = \frac{\hbar\Gamma}{2}$ was the limit of laser cooling and was dubbed the 'Doppler cooling limit'. A different method called time of flight (TOF) measurement was implemented which released the atoms and allowed them to fall under gravity into a probe beam which imaged the absorption of the cloud. The expansion of the cloud could again be used to estimate the temperature. Surprisingly many research groups found they were measuring a temperature well below the Doppler limit [46, and references 20, 21 therein]. This sub-Doppler cooling was a significant violation of the accepted theory previously studied by many authors [47, 48, 49]. It was clear that the simple model of a two level atom system in six red detuned beams was insufficient and needed to be developed further to include the other atomic levels and the laser polarisation. The theory was developed by J. Dalibard and C. Cohen-Tannoudji in 1989 [50] and became known as Sisyphus cooling. Sisyphus cooling allows cooling below the Doppler limit and is described in more detail in section 3.2.3. Over the subsequent years this technique was used to laser cool atoms to just a few microkelvin [51, 52]. Sisyphus cooling is sensitive to magnetic fields which would Zeeman shift the magnetic sub-levels and hence is not usually efficient in a MOT. However significant Sisyphus cooling can be achieved in an optical molasses.

The next major step in the cooling of atoms came in 1995 with the creation of a Bose-Einstein condensate (BEC) in rubidium [53], the result was two thousand atoms cooled to around 20 nK. Within a few months BECs had also been achieved in lithium [54] and sodium [55]. At such cold temperatures bosons condense at the centre of the trap into the lowest energy state. Seventy years earlier Bose and Einstein had published a theoretical paper on the quantum interaction that would result between very cold atoms, this theory correctly predicted the BEC [56] but until laser cooling techniques were refined it had been difficult to conclusively test this theory. To make a BEC, atoms from a MOT were transferred into a trap where they were evaporatively cooled allowing the hotter atoms with more energy

to escape, and the remaining atoms to re-thermalise. This is more difficult than it sounds because collisions are key to the re-thermalisation. As evaporation progresses the size of the trap falls by several orders of magnitude and so it is important to maximise the trap lifetime and initial size. Techniques such as compressed MOTs [57] where the magnetic field gradient is ramped up to compress the MOT can be used to increase the number of atoms transferred to the magnetic trap due to a better match in cloud shape. The lifetime is greatly improved with better vacuum but also, for magnetic traps, by preventing Majorana spin flips which are non-adiabatic changes of an atoms spin to an un-trapped high field seeking state ($g_F m_F < 0$). These can occur in a quadrupole magnetic trap if the rate of change of the magnetic field direction, from the perspective of the atom at position z from the centre of the trap, is greater than, or comparable to, the Larmor frequency $\omega_{Lar} = \frac{\mu_B g_F m_F z}{\hbar} \frac{dB}{dz}$. When this occurs the atoms magnetic moment can no longer adiabatically follow the magnetic field direction and spin flips become allowed. Inconveniently this occurs at the centre of the trap where the coldest atoms exist. For the creation of the first BEC in rubidium this was solved with a TOP (Time Orbiting Potential) trap where the magnetic field minimum precesses around the trap centre [58]. The first sodium BEC used a repulsive (blue detuned) laser focussed at the central minimum of the quadrupole field to repel atoms from the region where spin flips are allowed [55], and the Lithium BEC used six permanent magnets [59, 54].

A BEC is a coherent cloud of atoms behaving like one matter wave, interactions between two adjacent BECs have been studied and interference fringes were observed [60], essentially this is a double slit experiment for atoms. The BEC was converted into an 'atom laser' able to release coherent pulses of atoms or 'atom waves' [61], -this was dubbed an atom laser due to the nature of the matter waves pulses being analogous in appearance to that of a pulsed laser. Pulses were formed using a resonant RF pulse which cause a controllable fraction (depending on pulse time) of the atoms to evolve to an un-trapped state, the un-trapped BEC falls under gravity to form an atom pulse.

Simplification of the BEC setup and the development of atom optics led to the use of micro chips, which are commonly produced by lithography for the electronics industry and allow a designer to etch almost any pattern of wires, for use with cold atoms. These 'atom chips' can be used to magnetically trap atoms [62, 63, 64] and create a BEC [65, 66] which can be easily transported [67] or used for applications such as an atom beam splitter [68].

Other notable studies of the BEC are the observation of vortices which result when the BEC is rotated due to the quantum nature of the gas requiring that rotational paths are integer factors of the de Broglie wavelength [69] and studies relating to the Feshbach resonance [70]. Feshbach resonances are used to tune the s-wave scattering length and hence the elastic collision cross sections which can aid the evaporative cooling process for creating a BEC, but also used to manipulate atoms to produce Feshbach molecules. A Feshbach resonance occurs where the energy of two colliding atoms is equal to the energy of a bound molecular state which can be adjusted by tuning the scattering length which is dependent on the magnetic field. A magnetic field sweep was first used to create diatomic Feshbach molecules by Carl Wieman's group in 2002 [71], they found they could switch an atomic BEC between an atomic and molecular state by oscillating the magnetic field close to a Fesbach resonance. Diatomic molecules can also be produced optically by photoassociation [72].

Bose-Einstein condensate technology was extended to molecules and for the creation of a degenerate Fermi gas. Evaporative cooling of a Fermi gas is not possible directly due to the Pauli principle reducing the re-thermalisation collisions and so cooling is normally done using a buffer gas for sympathetic cooling [73]. Direct laser cooling of molecules is difficult due to the lack of a strong cycling transition caused by the complex number of vibrational and rotational states, however a BEC was used to cool the rubidium atoms which were then induced by Feshbach resonance to form bound states and create diatomic molecules . A BEC of molecules was achieved in 2003 [74, 75, 76].

Using constructive and destructive interference between counter-propagating laser beams it is possible to create an optical lattice with regions of intense light surrounded by regions of weaker intensity. Using the dipole force it is possible to load trapped atoms into the areas of intense light to form an optical array or 'lattice' (of lattice sites), the optical lattice in 2D and 3D was developed in 1993 [77, 78] and can be loaded from a BEC [79]. Optical lattices can also be used for cooling [80]. Mixtures of cold atoms have been loaded into optical lattices [81] creating an interesting and tunable way to study the properties of a crystal lattice.

Over the last ten years homonuclear and heteronuclear molecules have been formed by Feshbach resonances. Homonuclear molecules include ^{87}Rb [82], ^{40}K [75] and ^{40}K (p-wave) [83] and heteronuclear molecules include ^{85}Rb^{87}Rb (boson-boson) [84], ^{40}K^{87}Rb (fermion-boson) [85] and ^{6}Li^{40}K (fermion-fermion) [86]. Much of the motivation towards recent cold atoms research has been to develop a quantum computing

system [87], such a system could use the dipole moment of cold diatomic molecules as quantum bits of information (qubits) by aligning the dipole moment along or against an electric field. Quantum computing is still in its infancy. Recent developments include using cold atoms as memory [88, 89] and a spin orbit coupling (coupling spin and motion,) in a BEC to create a BEC with regions of spin-up and spin-down [90, 91]. Quantum information processing using trapped atoms received further recognition in 2012 with the Nobel prize in physics being awarded to D. J. Wineland and S. Haroche for work which involved trapped ions and cavity QED. For example using cold trapped ions to create entangled states [92] and using a single atom inside a cavity to create a quantum phase gate [93].
It has been proposed that cold atoms could be used for the study of quantum chromodynamics (QCD) [94], this would use boson fermion heteronuclear molecules as a model for diquark-quark system for a baryon (two quarks considered to be interacting with a third via the strong force). The coupling strength could easily be tuned using the Feshbach resonance.

1.2 Thesis Outline

1.2.1 Optical Injection Meets Atomic Physics

In the late 1980s diode lasers started to be manufactured for use in CD players. The mass production of these diodes made them cheap and readily available, and conveniently for atomic physicists 780 nm diodes were being used which corresponds to the D2 line in Rubidium. Previous optical molasses experiments had relied on dye lasers. The use of diode lasers for an optical molasses was demonstrated in 1988 [95] by Carl Wieman's group which would later become the first group to create a rubidium BEC. Despite the abundance of diode lasers in atomic physics experiments, few people have employed the dynamics from optical injection to atomic physics experiments with the exception of the common practice of using an injection locked laser as a beam power amplifier. A more detailed review of applications to date is given in section 2.1.5.
This thesis is divided into two main topics; demonstrating how dynamics created by optical injection can simplify some atomic physics experiments and the construction of a magnetic trap for rubidium atoms. The setup used for both experiments were constructed from scratch.

1.2.2 Thesis Structure

Chapter 2 describes the theory of optically injected diode lasers and the dynamics which result, these are then demonstrated as useful tools for the simplification of atomic physics experiments by using an optically injected diode laser to provide the two frequencies of laser light required for the creation of a MOT. Other applications are also discussed. Some technical details of the setup which may be required for atomic physics are also presented, for example the linewidth of the frequency components.

Chapter 3 describes progress towards creation of a BEC and an ultra-cold Fermi gas. A magnetic trap is constructed, into which rubidium atoms which have been pre-cooled in a MOT, are transferred. The theory of magnetic traps and future experiment plans are also presented to aid understanding of certain experimental design aspects.

The conclusion discusses these future applications and designs further and summarises achievements. The appendix contains details of many of the equipment designs and other technical notes.

Chapter 2

The Period One MOT Experiment

2.1 Background Theory

2.1.1 Diode Laser Subject to Optical Injection

In this section a model of the laser diode will be used to demonstrate the effects of optical injection. In order to construct a theoretical model of a laser diode subject to external optical injection we must first have a model of a laser diode. Despite their relatively simple principle of operation describing them fully would require a full quantum mechanical description. However for a laser diode a much simpler semi-classical approach has been found to predict the behaviour of the electric field and population inversion with extraordinary accuracy [20, 21]. This approximation ignores effects such as quantum fluctuations, squeezed states of light and polarisation effects. For this model we will treat the light within the laser cavity as a classical electric field but the atoms in the gain medium as quantum mechanical.

Rate Equations

Additional details of the rate equations derivation described here can be found in reference [22]. Let us consider a simple model of a laser cavity where the population inversion N, is a number density given by the pumping from the bias field created by the laser diode current J, minus the losses due to spontaneous and stimulated emission. The loss due to spontaneous emission is simply given by $\gamma_s N$ where γ_s is the spontaneous carrier decay rate and the loss due to stimulated emission to the

electric field is given by $N\gamma_{stim}$:

$$\dot{N} = J - \gamma_s N - N\gamma_{stim} \tag{2.1}$$

The dot denotes a derivative with respect to time. We can approximate the stimulated emission term by considering the gain in the electric field, since spontaneous emission occurs in all spatial directions this does not contribute significantly. The energy density of an electric field in a vacuum is described by:

$$\mu = \frac{1}{2}\epsilon_0 E^2 \tag{2.2}$$

Using the fact that the gain in energy due to one stimulated emission at a frequency ω_o is given by $\hbar\omega_o$, we can write the loss in population inversion per unit time to the two counter-propagating waves of the electric field as:

$$N\gamma_{stim} = -2n_r^2\epsilon_0\frac{|E|^2}{\hbar\omega_o}g \tag{2.3}$$

Where n_r is the refractive index in the gain medium, $|E|$ is the amplitude of the electric field and g is the gain in the electric field amplitude per unit time which is itself a function of the population inversion and electric field strength. Equation (2.1) then becomes:

$$\dot{N} = J - \gamma_s N - \frac{2|E|^2\epsilon_0 n_r^2}{\hbar\omega_o}g \tag{2.4}$$

Lets now consider a complex electric field $\hat{E}$ propagating through a gain medium inside a cavity. The field is of the form:

$$\hat{E} = E\exp^{i((\Omega-\Omega_{cold})t+\phi)} \tag{2.5}$$

Where Ω and Ω_{cold} are the cavity and cold cavity eigenfrequencies respectively. Here the term 'cold cavity' describes the properties of the laser cavity in the absence of a gain medium. The change in phase ϕ with respect to time is given by:

$$\begin{aligned}\dot{\phi} &= \Omega_{cold} - \Omega(\frac{1}{n_r}\delta n_r + 1)\\ \delta n_r &= \frac{g\alpha n_r\Gamma}{2\Omega}\end{aligned} \tag{2.6}$$

The change in the refractive index due to the population inversion is described by

δn_r. Γ is the confinement factor - fraction of the total field power confined to the active mode, for semiconductor diode lasers it is typically $0.02 \sim 0.04$ [96]. The alpha factor (α), also known as the linewidth enhancement factor, is a unit-less constant for a given laser which quantifies the relation between refractive index and population inversion. Originally used to describe the unexplained increase in the laser linewidth, the alpha factor was shown by C.H. Henry [97] to describe a coupling between intensity and phase noise fluctuations, via changes in the refractive index. The alpha factor can be written as [98]:

$$\alpha = -\frac{-4\pi}{\lambda}\frac{\partial(\delta n_r)/\partial N}{\partial g/\partial N} \tag{2.7}$$

Where λ is the light wavelength. In semiconductor lasers α is typically between 1 and 10 and can be determined experimentally. Combining equations (2.5) and (2.6) we can express how the electric field evolves with time as it passes through the gain medium:

$$\dot{\hat{E}} = i\hat{E}(\Omega - \Omega_{cold}) - \frac{1}{2}i\hat{E}\alpha\Gamma g \tag{2.8}$$

For a field within a real laser cavity the electric field has a decay rate γ_c caused by losses due to the cavity properties, for example, due to transmssion through the cavity mirrors, and there is also a gain in electric field strength from the population inversion. Hence the change in the field with respect to time within a laser cavity is given by:

$$\dot{\hat{E}} = -\frac{\gamma_c}{2} + i\hat{E}(\Omega - \Omega_{cold}) - \frac{1}{2}\Gamma(1 + i\hat{E}\alpha)g \tag{2.9}$$

Equations (2.4) and (2.9) form two coupled equations which describe a semiconductor diode laser without optical injection. The gain is related to both population inversion and electric field, and is given by equation (2.10). The gain is assumed to equal the cavity losses when the population inversion and electric field are at their stable states $N = N_s$ and $E = E_s$.

$$g(N, E) = \frac{1}{\Gamma}\left(\gamma_c + \frac{\gamma_n\gamma c}{\gamma_s J}\frac{N - N_s}{N_s} - \gamma_p\left(\left(\frac{E}{E_s}\right)^2 - 1\right)\right) \tag{2.10}$$

The differential carrier relaxation rate γ_n, and non-linear carrier relaxation rate γ_p quantify the change in the gain with respect to the carrier density and photon density respectively [99].

Steady States

We can solve equations (2.9) and (2.4) to find the steady state values. First these equations are written in terms of the intensity $I = \frac{1}{2}\epsilon_0 c|E|^2$:

$$\begin{aligned} \dot{N} &= J - \gamma_s N - \frac{4In_r^2}{\hbar\omega_o c} g \\ \dot{I} &= I(\Gamma g - (1+\Gamma)\gamma_c) \end{aligned} \tag{2.11}$$

We can write a simplified expression for the gain linearised with the population inversion around transparency by considering the gain to equal cavity losses at $N = N_{Thr}$:

$$\hat{g} = (-\gamma_c + \xi(N - N_{Thr})) \tag{2.12}$$

where $\xi = \frac{\gamma_n \gamma_c}{\Gamma \gamma_s J}$. Inserting equation (2.12) into (2.11) and solving we obtain the stable states N_s and I_s:

$$\begin{aligned} N_s &= \frac{\gamma_c + 2\Gamma\gamma_c + N_{Thr}\Gamma\xi}{\Gamma\xi} \\ I_s &= \frac{(\gamma_c\gamma_s + 2\Gamma\gamma_c\gamma_s - J\Gamma\xi + N_{Thr}\Gamma\gamma_s\xi)\hbar\omega_o c}{4n_r^2(1+\Gamma)\gamma_c\xi} \end{aligned} \tag{2.13}$$

Relaxation Oscillation

When lasers are subject to some small perturbation to either the population inversion or electric field the laser will not immediately return to a steady state, this will instead cause oscillations of frequency ω_{RO} around the steady states. Under normal conditions these oscillations are damped by a rate Γ_{RO}. These relaxations oscillations can be demonstrated by modelling the population inversion and field intensity using equations (2.9) and (2.4). We can describe the relaxation oscillation as:

$$s = -\Gamma_{RO} + i\Omega_{RO} \tag{2.14}$$

Now making a small perturbation to the population inversion and intensity away from the stable state we can insert $N = N_s + \delta N$ and $I = I_s + \delta I$ into equation (2.11). Since this perturbation is assumed to be small we can neglect terms containing two

δ terms:

$$\begin{aligned} \delta\dot{N} &= I_s\Gamma\delta N\xi \\ \delta\dot{I} &= \frac{k(-\gamma_c\delta I + I_s(\gamma_c + 2\Gamma\gamma_c - \Gamma\delta N\xi))}{\Gamma} \end{aligned} \tag{2.15}$$

Combining equations into one second order derivative we get:

$$\ddot{I} = -\frac{k_c(-\gamma_c I_s\Gamma\delta I\xi - I_s\Gamma\xi\dot{\delta I})}{\Gamma} \tag{2.16}$$

Here we have used the simplification that $k_c = \frac{2n_r^2\epsilon_0}{\hbar\omega_o c}$. The small perturbation causes a small oscillation around the stable state so we can write $\delta I = \frac{d}{dt}e^{st}$. Inserting this into the equation above we can obtain an equation for s:

$$s^2 + k_c(-I_s\xi s - I_s\gamma_c\xi) = 0 \tag{2.17}$$

Solving this equations we obtain expressions for Ω_{RO} and Γ_{RO}:

$$\begin{aligned} \Gamma_{RO} &= \frac{1}{2}I_S k_c\xi \\ \Omega_{RO} &= \sqrt{k_c I_s\gamma_c\xi + \frac{1}{4}I_s^2k_c^2\xi^2} \end{aligned} \tag{2.18}$$

Since in practise a laser under normal operating conditions satisfies $k_c I_s\gamma_c\xi \gg \frac{1}{4}I_s^2k_c^2\xi^2$ the oscillation frequency is described as

$$\omega_{RO} = \sqrt{k_c I_s\gamma_c\xi} \tag{2.19}$$

The oscillation appears in both the population inversion and intensity offset by $\frac{\pi}{2}$, it represents an exchange of energy between the electric field and population inversion. The $\frac{\pi}{2}$ offset is likely to vary slightly in a real laser depending on properties of the laser cavity and gain medium which are not accounted for in this idealised model.

Modulation Limitations

Crucially for this work the relaxation oscillation sets a limit of the rate at which the intensity can respond to a change in population inversion, hence it is also the limit at which a laser can be modulated in frequency or intensity by modulation of the pump current. Since ω_{RO} is related to the intensity, which is dependent on the

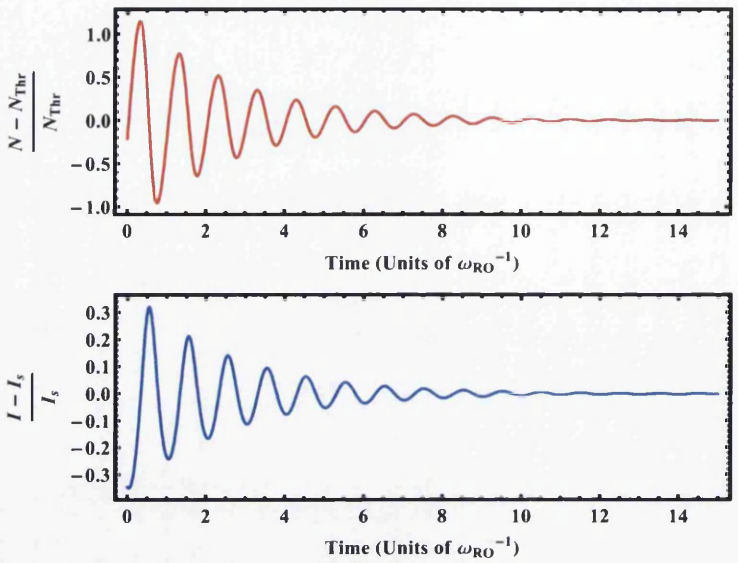

Figure 2.1: Population inversion (red) and intensity (blue) immediately after a change in pump current.

pump current, ω_{RO} scales like $\sqrt{J}$. Typically for a laser diode above threshold, the relaxation oscillation is in the range of a few GHz to a few tens of GHz. In this thesis a novel way of overcoming this modulation limit using optical injection will be applied to atomic physics.

Adding Optical Injection

Next we can add in an external injected field to the rate equations which has a frequency Δf relative to the laser without injection. If the injected field is of the form $\tilde{E_{inj}} = E_{inj}\cos(\Delta f t + \phi_{inj})$ then the field and amplitude ($\hat{E_{inj}}$) can be written as:

$$\begin{aligned} \tilde{E_{inj}} &= E_{inj}e^{i\Delta f t} \\ \hat{E_{inj}} &= E_{inj}e^{i\phi_{inj}} \end{aligned} \tag{2.20}$$

Adding this injected field to equations (2.4) and (2.9) with coupling strength η we arrive at equations which describe a single mode laser under external optical

injection

$$\begin{aligned}\dot{\hat{E}} &= -\frac{\gamma_c}{2} + i\hat{E}(\Omega - \Omega_{cold}) - \frac{1}{2}\Gamma(1 + i\hat{E}\alpha)g + \eta\hat{E_{inj}}e^{i\Delta ft} \\ \dot{N} &= J - \gamma_s N - \frac{2|E|^2\epsilon_0 n_r^2}{\hbar\omega_o}g\end{aligned} \tag{2.21}$$

2.1.2 The Dynamical Regions of Lasers Subject to Optical Injection

In this section the diode laser rate equations will be rescaled into a form convenient for numerical modelling. The population inversion and electric field can be rescaled relative to their steady state values N_s and E_s respectively. The injected field E_{inj} and current J are also rescaled as follows to simplify the equations:

$$\begin{aligned} n &= \frac{N - N_s}{N_s}, & A &= \frac{|E|}{|E_s|}, \\ A_{inj} &= \frac{\eta E_{inj}}{\gamma_c E_s}, & J_c &= \frac{J - \gamma_s n_s}{\gamma_s n_s} \end{aligned} \tag{2.22}$$

The gain also simplifies to equation (2.23).

$$g = \frac{1}{\Gamma}(\gamma_c + \frac{\gamma_n\gamma_c}{\gamma_s J}n - \gamma_p(A^2 - 1)) \tag{2.23}$$

Inserting equations (2.23) and (2.22) into (2.21), and splitting the electric field $A = a + ib$ into the real and imaginary parts we obtain equations (2.24).

$$\begin{aligned} \dot{a} &= -\frac{1}{2}(a + \alpha b)\left(-(a^2 + b^2 - 1)\gamma_p + \frac{n\gamma_c\gamma_n}{J_c}\right) + A_{inj}\gamma_c\cos(2\pi t\Delta f) \\ \dot{b} &= -\frac{1}{2}(-\alpha a + b)\left(-(a^2 + b^2 - 1)\gamma_p + \frac{n\gamma_c\gamma_n}{J_c}\right) - A_{inj}\gamma_c\sin(2\pi t\Delta f) \\ \dot{n} &= -(\gamma_s + \gamma_n(a^2 + b^2)) - \gamma_s J_c(a^2 + b^2 - 1) + \frac{\gamma_s\gamma_p}{\gamma_c}J_c(a^2 + b^2)(a^2 + b^2 - 1) \end{aligned} \tag{2.24}$$

The above equations can now be used to demonstrate the main features and dynamics which occur within an optically injected laser diode. The map of dynamical regions in reference [100] was created using these equations and hence it is used as a guide. For the purposes of modelling we set the laser diode constants to be at typical values listed in table 2.1.

Parameter	Symbol	Value used for modelling
Linewidth enhancement factor	α	3
Cavity decay rate	γ_c	5.36×10^{11} s^{-1}
Spontaneous carrier relaxation rate	γ_s	5.96×10^{9} s^{-1}
Differential carrier relaxation rate	γ_n	7.53×10^{9} s^{-1}
Non Linear carrier relaxation rate	γ_p	1.91×10^{10} s^{-1}
Normalised current above threshold	J_c	1.2

Table 2.1: Table of laser parameters.

The sections below show the main dynamics which occur within the laser. We find these dynamical regions by varying A_{Inj} and Δf which are experimentally accessible, note that the values in table 2.1 are fixed except for J_c. The boundary between dynamical regions are discrete transitions from one dynamic to another and most boundaries are fixed points for a given laser, however hysteresis has been observed on some region boundaries depending on whether A_{Inj} or Δf are being increased or decreased [24].

Several dynamical regions are presented in three panels showing: the optical spectrum, a combined 3D phase-space plot of the real and imaginary parts of the electric field with the population inversion, and the laser intensity $I \propto |E|^2$ relative to the steady state intensity. The optical frequency spectrum is formed from a normalised fourier transform of the electric field to give the power distribution over frequency and is shown relative to the free running slave laser frequency. Note that this spectrum can only be used to demonstrate the distribution of power and not linewidth due to the idealised nature of the model which, for example, does not account for some quantum effects. For clarity the 3D plots of n and the electric field A are given in the reference frame of the injected laser:

$$\hat{A} = (\hat{a} + i\hat{b}) = (a + ib)e^{i\Delta f t} \tag{2.25}$$

Unlocked

For very weak or zero injection the laser is unaffected and remains unlocked. As shown in figure 2.2 there are no noticeable changes to the spectrum and the population inversion and electric field amplitudes remain at their steady state values. The optical spectrum is a single peak at the free running laser frequency and the intensity remains constant at the stable state. There is no peak in the optical spectrum at the injection frequency.

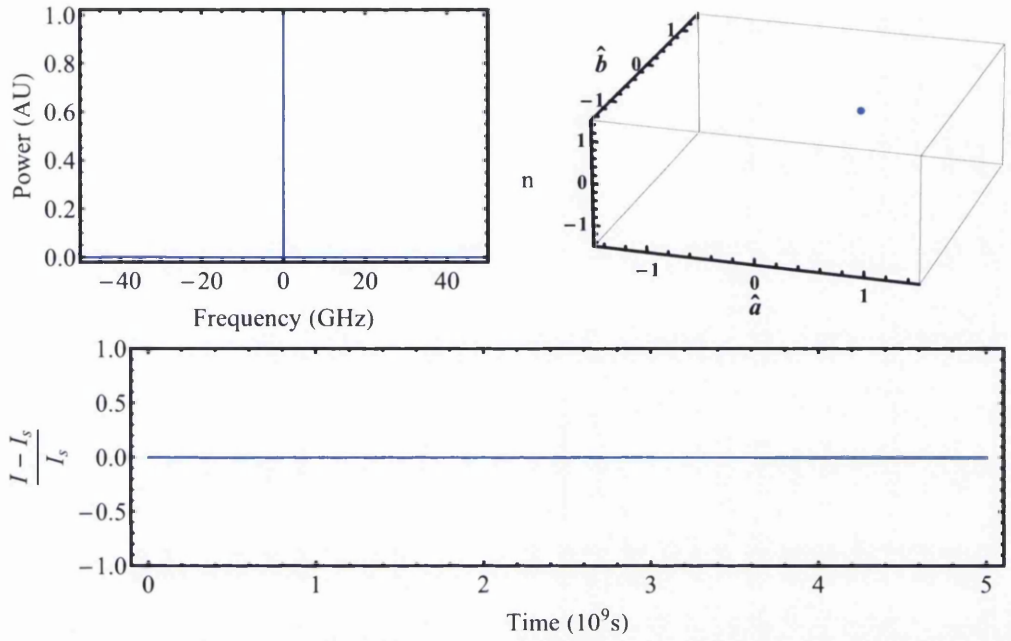

Figure 2.2: $A_{inj} = 0.00001$ and Δf =15 GHz. At very low injection the slave laser is not affected and remains unlocked.

Injection Locked

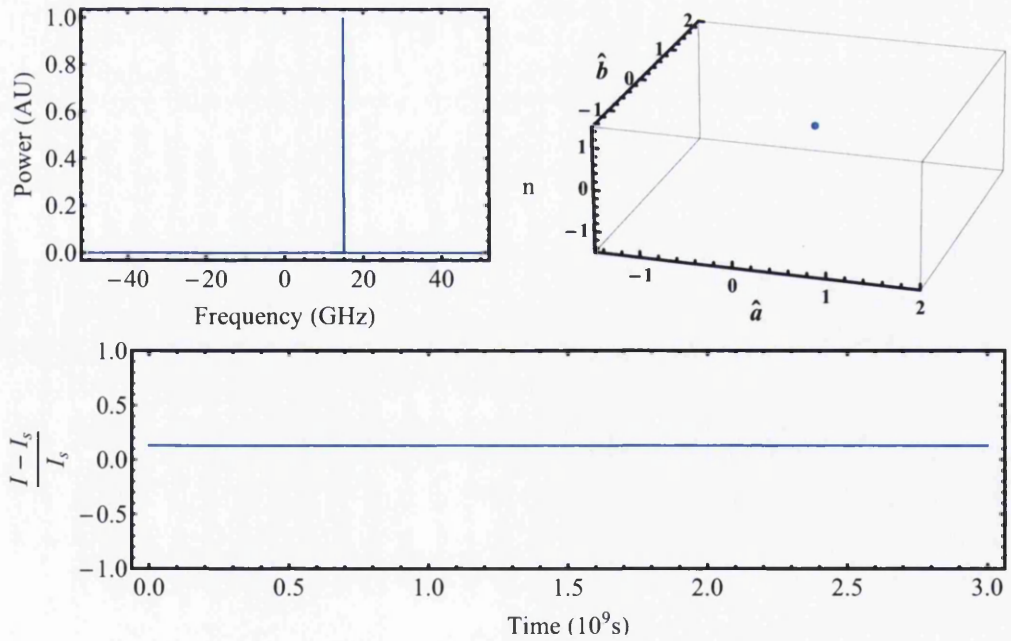

Figure 2.3: $A_{inj} = 0.31$ and Δf =15 GHz. The increased power causes the slave laser to become locked to the master laser however the laser is stable.

At higher values of injection (figure 2.3) the slave laser becomes locked to the frequency of the master laser frequency at 15 GHz. The population inversion, electric field and intensity are steady but shifted slightly relative to the free running slave laser.

Period One State - Locked and Unlocked

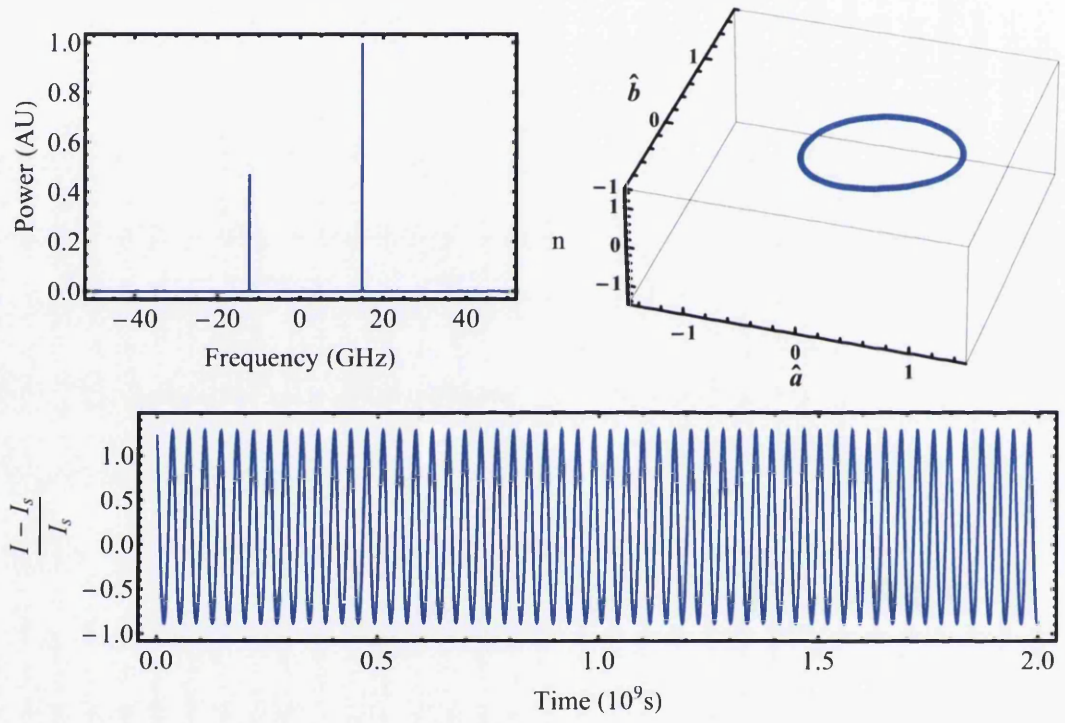

Figure 2.4: An almost single sideband locked P1 oscillation forms at $A_{inj} = 0.23$ and Δf =15 GHz. The electric field ($\hat{a}$,$\hat{b}$) and population inversion n create a closed loop in the phase space which is not in a plane and crosses the $n = 0$ plane twice in an orbit. This creates a periodic oscillation in the laser intensity. The spectrum is assymetric with the high frequency sideband only just visible at 42 GHz.

In figure 2.4 the optical injection creates a beat frequency in the slave laser cavity between the master and slave laser which causes the relaxation oscillation to become undamped and shift to higher frequencies. The field is locked to the injection frequency at which there is most of the laser power, however population inversion and field amplitudes oscillate relative to the locked field causing frequency sidebands. Energy is oscillating between the real and imaginary electric field and

population inversion in a single periodic motion causing intensity to also oscillate. Hence this is called 'period one' (P1) oscillation. In this locked period one oscillation the spectrum consists of a strong peak at the injection frequency with weaker sidebands detuned from the main peak by the shifted relaxation oscillation. Weaker higher harmonics are also just visible. A semiconductor laser diode undergoing P1 oscillation typically has an asymmetric spectrum with the high (or low) frequency sidebands being much higher in intensity than the low (or high) frequency sideband. This can be tuned in amplitude to some degree with adjustment of A_{Inj} and Δf. It is therefore common to have one sideband far more intense than the others as shown in figure 2.4 which can be considered as negligible intensity and hence this is referred to as a single sideband P1. The reason for the assymetric spectrum is that the low frequency side band is closest to the cavity resonance without optical injection and so the gain curve favours one sideband - a result of the linewidth enhancement factor causing a detuned cavity effect [101]. The suppression ratio of the weaker sideband has been mapped out for Δf and A_{Inj} [102]. These sidebands are typically described as microwave sidebands since they are in the GHz regime, they can also be tuned in frequency by tuning either the master/slave detuning Δf or the injection power A_{inj}. Figure 2.5 shows the spectrum after the injection power has been increased slightly from figure 2.4.

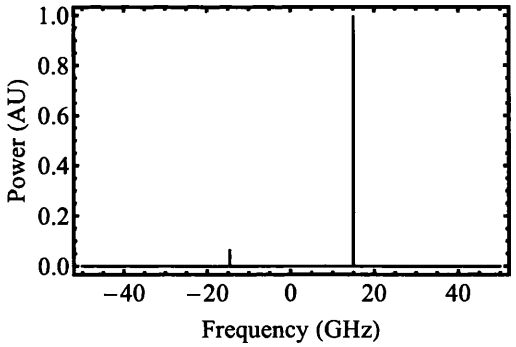

Figure 2.5: $A_{inj} = 0.275$ and $\Delta f = 15$ GHz. A single sideband P1 oscillation after the frequency / intensity of the sideband has been tuned by increasing the injection power from figure 2.4.

For weaker injection (and typically smaller detunings) it is possible to create an unlocked P1 oscillation. The injection does not create a large peak at the injection frequency, instead the injection causes the slave laser frequency to shift whilst the beat frequency causes the relaxation oscillation to become undamped and also shift

in frequency. Similar to the locked case the electric field and population inversion oscillate and exchange energy. The resulting optical spectrum of this dynamic can vary somewhat but typically it consists of a weak peak at the injection frequency (the shifted relaxation oscillation) and stronger peaks detuned by some GHz to higher and lower frequencies. Higher peak harmonics are also generally visible. The amplitude and frequency of the shifted peaks can be tuned by adjustment of the injection power or master-slave detuning. The spectrum is not symmetric around the injection frequency, high and low frequency sidebands can have very different amplitudes, as with the locked P1 oscillation it is possible to reduce the amplitude of either the high or low frequency sideband to almost zero.

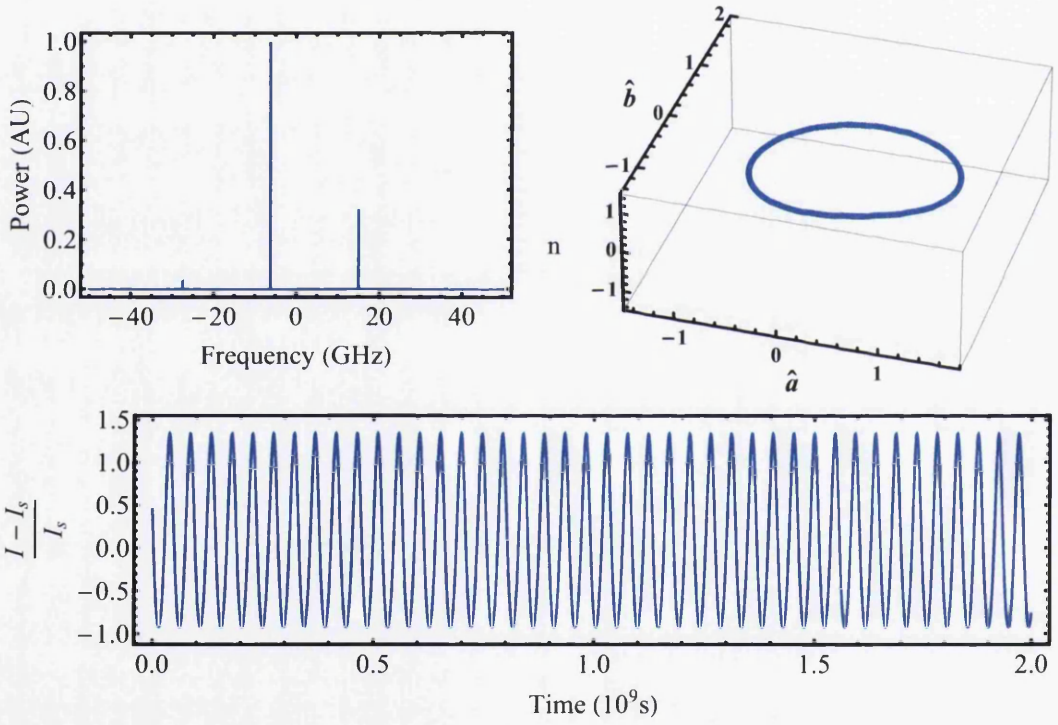

Figure 2.6: $A_{inj} = 0.12$ and Δf =15 GHz. An unlocked P1 oscillation. The laser exhibits very similar properties to those shown in figure 2.4 however the majority of the slave laser power is not locked to that of the master laser but is shifted to lower frequency. A sideband forms at the injection frequency.

Chaos and Other Dynamics

It is possible for the injection to induce a quasi-periodic oscillation in the electric field and population inversion which has 2,3,4 or even higher number of periods (P2,

P3, P4 etc). Figure 2.7 shows an example of period two (P2) oscillation.

Higher order periodic oscillations are shown in figures 2.8 and 2.9 before the competing frequencies cause the laser to become chaotic in figure 2.10, this is known as the period doubling route to chaos. When the laser is chaotic the optical spectrum and intensity become very noisy and do not follow any periodic pattern, however the spectrum is not devoid of structure, in figure 2.10 a strong peak is still visible and often sidebands are visible too.

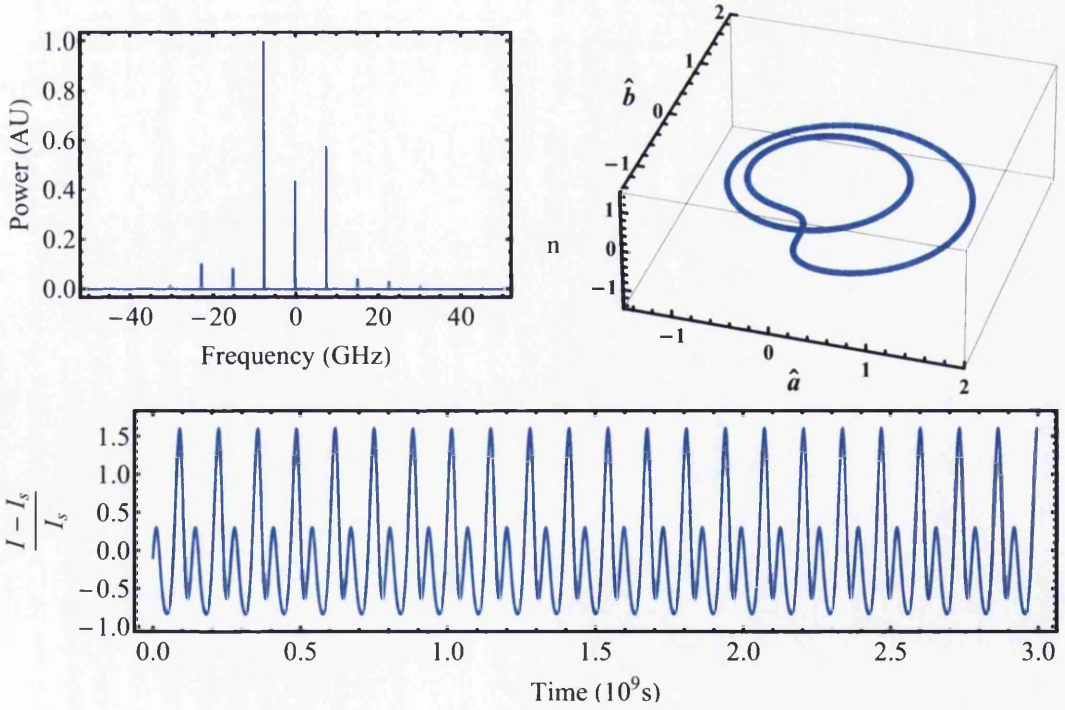

Figure 2.7: $A_{inj} = 0.06$ and Δf =15 GHz. P2 oscillation. Additional peaks appear in the frequency spectrum midway between P1 sidebands. The phase space plot of the electric field and population inversion now contains two loops which do not intesect and cross the $n = 0$ plane 4 times in one complete period.

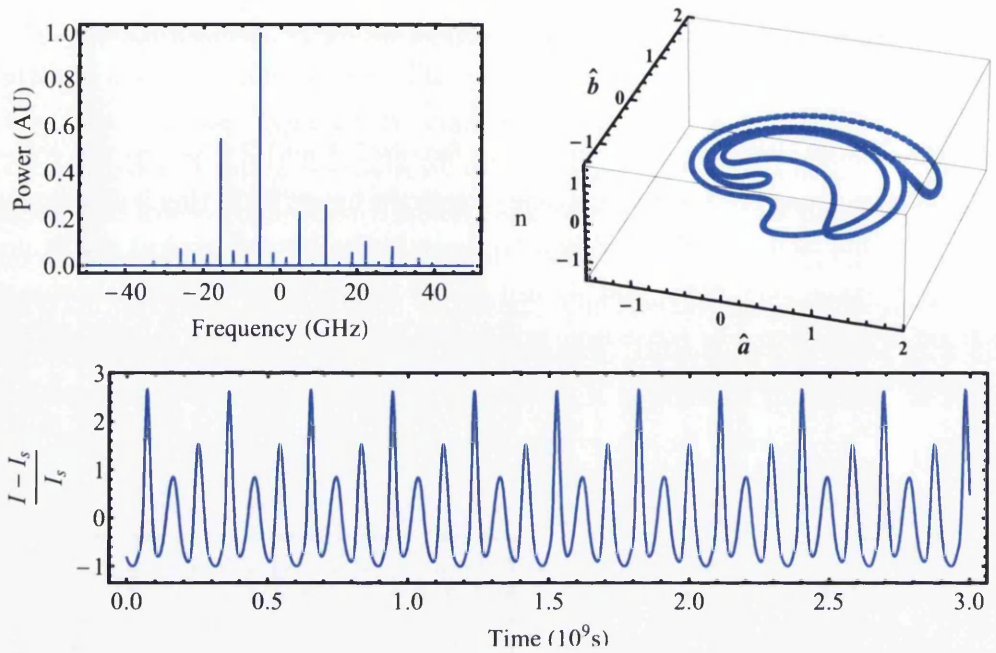

Figure 2.8: $A_{inj} = 0.045$ and $\Delta f = 5$ GHz. P3 oscillations are observed. Further peaks appear in the spectrum and the lines in the phase space plot of the electric field and population inversion do not cross.

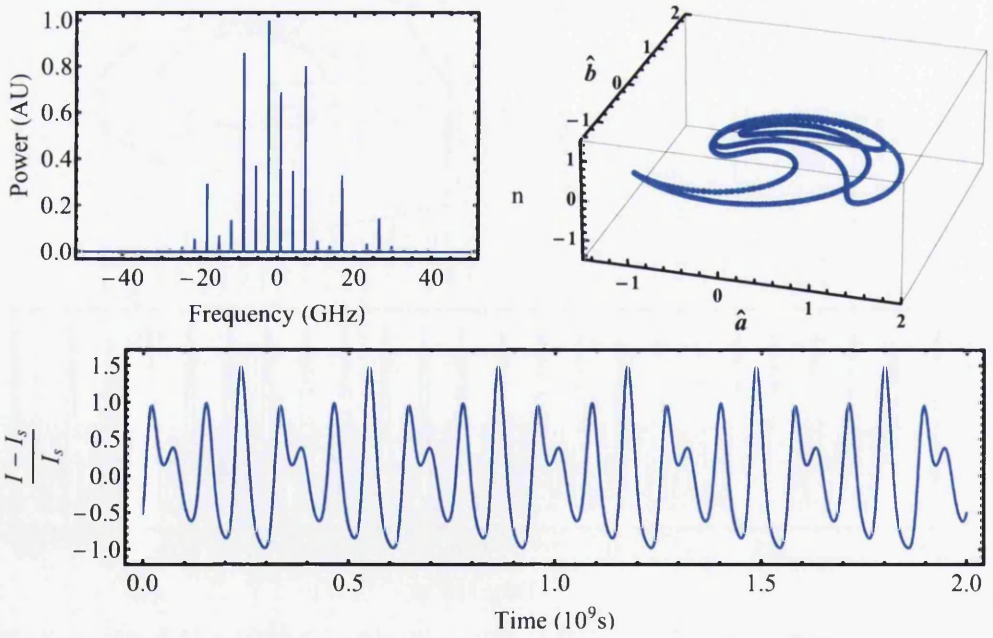

Figure 2.9: $A_{inj} = 0.042$ and $\Delta f = 4.05$ GHz. P4 oscillations are observed. The electric field and population inversion phase space plot is a closed orbit made of 4 loops which do not cross. The laser is still stable.

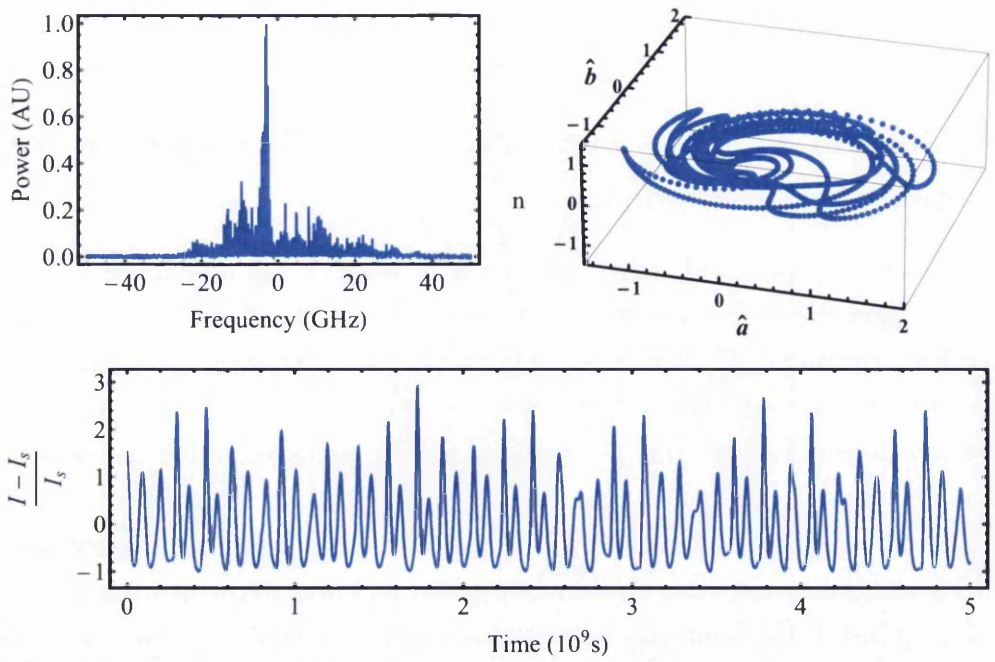

Figure 2.10: $A_{inj} = 0.05$ and Δf =8 GHz. A chaotic laser. The electric field and population inversion phase space plots show an open loop. The frequency spectrum is chaotic but not completely devoid of structure - a large central peak is still visible.

2.1.3 Re-scaling the Injection Power and Injection Frequency

From now on we define the injection power k relative to the slave output power since this is simpler to measure experimentally and is proportional to the field amplitude. We also rename the slave laser detuning f_i to follow convention.

$$k = P_{Inj}/P_{SL} \tag{2.26}$$

$$f_i = \Delta f = f_{ML} - f_{SL} \tag{2.27}$$

In our experiment injection power P_{Inj} and slave power P_{SL} were always measured at the aperture of the slave laser. Note that:

$$\begin{aligned} I_{Inj} &= \frac{1}{2}\epsilon_0 c|E_{Inj}|^2 \\ P_{Inj} &= \int I_{Inj} dxdy \end{aligned} \tag{2.28}$$

where the x-y plane is the cross sectional plane of the injected field propagation direction.

2.1.4 General Features and Similarities of Dynamical Regions in Laser Diodes

Theoretical and experimental maps have been created of the dynamical regions occurring in laser diodes for varying values of k and f_i [21, 23, 24, 25, 100, 102]. The map from reference [23] is shown in figure 2.11. Some features are common to all maps. A large region of P1 oscillation dominates the positive f_i region, as $k \to 0$ and $f_i \to 0$ regions of higher order periodic oscillation, chaos and other instabilities are observed. At high injection power the P1 region gives way to a locked region. The negative f_i region is dominated by a locked region which forms a narrow band between P1 oscillation and other dynamical regions for lower values of k and f_i. On a map of k against f_i the boundary between locked and P1 oscillation creates a line which is locally almost parabolic in shape and can clearly be seen in reference [23], figure 3 and [25], figure 4. The parabola has a minimum point known as the Hopf minimum.

2.1.5 Optical Injection Applications and Proposed Applications to Date

Of all the dynamics which result within an optically injected diode laser the two which have been most widely used in applications are the stable injection locking region and the chaotic region. As well as acting as an amplifier of a weak injection laser and for linewidth reduction [103], stable injection locking can also be used to: increase the modulation bandwidth of a laser diode [104, 105], reduce the broadband noise of a laser [104] and for chirp reduction (change in the instantaneous laser radiation frequency with time for a pulsed laser) [106]. In atomic physics experiments injection locking has been used, for example, to create two laser beams with a relative linewidth of less than 10 Hz for probing transitions in strontium ions [107] and to create higher power narrow linewidth light for a lithium MOT [108]. The chaotic dynamic has been successfully used in chaos synchronisation [27, 28] which has important applications in secure communications. The chaotic region was observed in the course of this work but not used for any application. As described

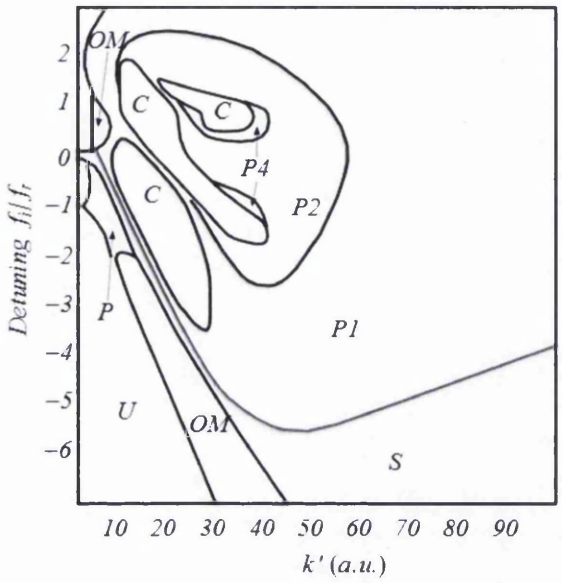

Figure 2.11: Map of the dynamical regions from reference [23]. S = Stable locking, P1 = Period one oscillation, P2 = Period two oscillation, C = Chaos, U = unlocked. Other dynamical region are explained in reference [23]. Since k is reserved for the setup described in this thesis the injection power k' is as defined in reference [23].

in the theory section above microwave sidebands can be created in the slave laser optical spectrum creating a P1 oscillation. Crucially these sidebands can be tuned by adjustment of the master slave detuning f_i or the injection power k.

Potential applications of the P1 oscillation are discussed by S.-C. Chan *et al.* in reference [29]. In this paper the P1 oscillation is presented as a method of generating microwave sidebands and compared to other methods such as optical heterodyning [109, 110] (creating a microwave beat from two detuned co-propagating laser beams), an optical phase locked loop [111] (optical feedback used to lock the phase of two heterodyne lasers) or dual mode lasers [112]. Reference [29] demonstrates how the amplitude variation of the injection beam causes a frequency variation in the sideband frequency and therefore it can also be used as an amplitude modulation to frequency modulation (AM to FM) converter. Also in reference [29] the P1 oscillation is demonstrated as a suitable source for LiDAR capable of velocity and position measurement. This is done by back scattering a sample of the beam from a target, and after detection, combining the microwave envelopes on an RF mixer

to determine the Doppler shift on the back scattered beam and hence the target velocity. A similar principle can be used to find the target position if the power spectrum of the mixer is used to take an inverse power spectrum and hence obtain a plot of power vs time which will have a peak at the delay time of the back scattered signal.

Modern atomic and spectroscopy experiments require tunable high power lasers which have linewidths of the order of a megahertz or less. This is commonly achieved with an external laser cavity created by a grating which can be adjusted for fine tuning of the laser frequency. The downside of this technique is that the laser power is compromised because a large proportion (typically around 50%) of the light is back reflected into the laser by the grating. Optical injection is often used in atomic physics or other laser experiments to amplify the power from a low power laser diode by injection into a higher power diode [108] which then takes on the linewidth and frequency properties of the master laser. But in this scenario the injection merely acts as a light amplifier. It is not the case that injecting almost any laser power from a master laser into a slave laser separated by some small frequency will cause the slave laser to become locked, in reality the locking band is formed by only a narrow band in (f_i, k) space.

Laser diodes can be current modulated at microwave frequencies to create sidebands in the optical spectrum. These sidebands can be tuned by adjustment of the modulation frequency and have been used to create a MOT in rubidium [113] and potassium [114] and also for the single beam tetrahedral rubidium MOT [115, 116]. There are two problems with this technique; Firstly the modulation frequency, and hence sideband frequency, are limited by the modulation bandwidth of the slave laser diode. This bandwidth is set by the lifetime of the upper state in the laser which limits how quickly the population inversion can be varied by current modulation. Hence the modulation bandwidth is approximately the relaxation oscillation. Secondly the amplitude of the sidebands are not independently tunable. In reference [117] the (current modulation) sidebands are amplified by optical injection into a slave laser enabling some degree of sideband power tuning. M Vangeleyn *et.al* [115, 116] optimised power in the sideband by tuning the laser cavity size and relaxation oscillation resonance, however this optimised the laser for a specific frequency only. Using a P1 oscillation it is possible to obtain a single sideband oscillation which

limits the power loss to other sidebands and harmonics. External modulators such as electro-optic modulators (EOMs) or accousto-optic modulators (AOMs) can also be used to create frequency shifted light, but typically EOMs are not very tunable and AOMs operate in the 100 MHz range.

As injection locking is commonly used in atomic physics as a light amplification method it seems appropriate that the tunable sidebands resulting from P1 oscillation could be used to simplify equipment in experiments which require more than one optical frequency, this could be done using an existing optical injection setup. Unlike the current modulation technique the P1 oscillation sidebands can be tuned beyond the current modulation bandwidth because the sideband is the shifted RO frequency. A demonstration of how the P1 oscillation can be applied to atomic physics will be carried out by using the two resulting frequencies from the slave laser to create a magneto-optical trap, but first previous similar work will be discussed.

In 1996 H.S Moon *et al.* [118] used two frequencies from an injection seeded laser to create a ^{85}Rb MOT. In this case they start with an injection locked laser and decrease the injection power until multiple frequencies are observed. By adjusting the slave laser current and hence detuning, they are able to tune the two most prominent peaks to a separation of approximately 3 GHz, from which they are able to both trap and re-pump a ^{85}Rb MOT. From the description of the spectrum observed and low injection power used it is likely they were operating in the 'pulling' region (see section 2.3.1). This pulling region was observed in the course of our work, however, we had optimised our setup to maximise injection power and so it was only observed for very low k typically where the beam was misaligned. This made adjustment of the optical frequencies very coarse so we did not investigate this region further, however there are a number of advantages of the sidebands created by pulling. The pulling region is another P1 oscillation and the hence the sideband amplitude and frequency can be tuned [118]. Due to k being insufficient to lock it is also possible for the sideband to be tuned to frequencies very close to (within a few MHz of) the injection frequency without the laser becoming locked or moving to another dynamic, this could be useful for two frequency applications which require small frequency separations such as addressing two hyperfine transitions separated by a few hundred megahertz or less. In contrast the P1 oscillation will typically become locked if the sideband is within $1 - 2$ GHz of the injection frequency. The

disadvantage of the pulling region is that typically only a few GHz tuning are possible before the laser modehops or becomes unlocked due to the weak injection power, however for the P1 oscillation a sideband can be tuned many tens of GHz away from the injection frequency.

Reference [118] trapped mainly ^{85}Rb but they also note that by increasing the injection power they can trap ^{87}Rb which requires the sideband to be 6.6 GHz away. Curiously this paper does not state what happens to the linewidth of the optical frequencies emitted from the slave laser, however the fact the trap works implies that the frequency component addressing the cycling transition must be a few MHz or less. The linewidth of an injection locked laser has been investigated [119]. Partial linewidth transfer occurs for lower k but as k is increased complete linewidth transfer was found to occur. Note that only the linewidth within the locking bandwidth was studied. Typically a free running diode laser which does not have an external cavity or grating stabilisation would have a linewidth of tens of MHz, however this can be reduced by increasing the laser current or decreasing the temperature [120]. It is possible that due to the high bias current of the slave laser that the free running linewidth of the laser in reference [118] was already very narrow. If P1 sidebands were to be used in atomic physics experiments it would be important that linewidth transfer occurred for both the optical frequencies.

2.1.6 Magneto-Optical Traps (MOTs)

A magneto-optical trap (MOT) can be thought of as an optical molasses which is spatially confined. MOTs can be loaded directly from a room temperature vapour [121, 122] and provide an excellent source of ultracold atoms which can subsequently be loaded directly into a magnetic trap.

Recall that laser cooling is achieved by an atom absorbing a photon from beam propagating opposed to the atoms motion and spontaneously emitting the photon in a random direction. Successive absorption, from a beam travelling in one direction, followed by emission in random directions (which cancel out) creates a net force on the atom and this is known as the scattering force.

Consider an atom with a ground and excited state with total angular momentum $F = 0$ and $F' = 1$ which each have magnetic sub-levels m_F representing the projection of the total angular momentum onto the quantisation axis. The ground state will have levels $|F, m_F\rangle = |0, 0\rangle$ and the excited states will be $|F', m'_F\rangle = |1, -1\rangle$,

$|1,0\rangle$ or $|1,+1\rangle$. A quadrupole field generated from anti-Helmholtz coils creates a field which is linear with displacement from the origin and zero at the trap centre which coincides with the origin. The Zeeman shift causes a shift to the atoms energy levels δE given by

$$\delta E = \mu_B g_F m_F B \tag{2.29}$$

Where μ_B is the Bohr magnetron, g_F is the Landé g-factor and B is the magnetic field magnitude.

Three orthogonal counter-propagating laser beam pairs (usually derived from the same laser) cross at the centre of the trap. The laser is red detuned from the atomic transition by a small amount δf. An atom moving along one axis will observe the beam it is moving towards to be Doppler shifted closer to resonance whilst the beam it is moving away from will be Doppler shifted away from resonance, hence a moving atom will favour the scattering force from the counter-propagating beam. By choosing each beam to drive only $\Delta m_F = +1$, or $\Delta m_F = -1$ we can spatially confine the atoms also as shown in figure 2.12. A quadrupole magnetic field Zeeman shifts m_F levels towards resonance with the laser beam propagating towards the centre of the trap. Selective Δm_F transitions are driven by using light which is circularly polarised relative to the quantisation axis which is set by the magnetic field direction. If the laser polarisation addresses the $\Delta m_F = -1$ transitions then the light is said to be σ^- polarised and addressing the $\Delta m_F = +1$ transitions would be σ^+ polarised. Note that this means the polarisation is defined relative to the magnetic field direction, which is opposed on opposite sides of the trap, and so the laser light in the atomic reference frame flips from σ^+ polarisation to σ^- polarisation as the atom crosses the quadrupole centre.

A schematic of the ^{87}Rb D2 line and the laser frequencies required for a MOT are shown in figure 2.13. In our experiment we use the ^{87}Rb $F = 2$ to $F' = 3$ D2 line ($5^2S_{1/2} \rightarrow 5^2P_{3/2}$) as our cycling transition which is addressed by a 'cooling laser'. Due to the selection rule that ΔF = (-1 or 0 or +1), atoms in the upper $F' = 3$ state can only decay back to $F = 2$, hence completing the cycle. An undesirable consequence of addressing this cycling transition is that we also address the $F = 2$ to $F' = 2$ transition because the $F' = 2$ and $F' = 3$ hyperfine levels are only separated by 266.65 MHz. There is still appreciable cross section at the $F = 2$ to $F' = 2$ transition due to: the high intensity of the cooling laser, the natural linewidth of $\frac{\Gamma}{2\pi} = 6.07$ MHz, the red detuning of the cooling laser frequency, Doppler shifts and

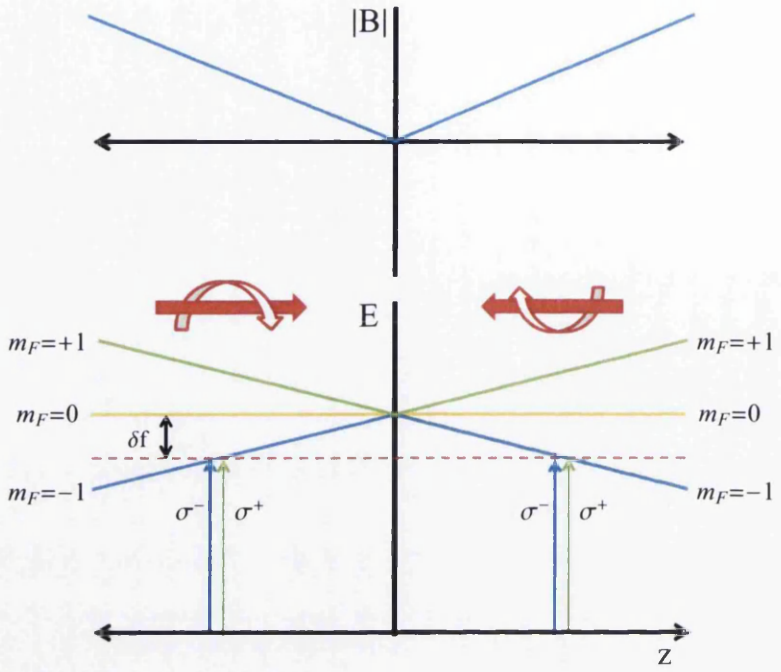

Figure 2.12: The MOT in one dimension. Away from the trap centre the $m_F = -1$ level is shifted towards resonance with the σ^- beam which will always be the beam pointing back towards the centre. The red dashed line indicates the laser red detuning δf which coincides with the Zeeman shift in the $m_F = -1$ level at certain points along the z - axis.

Zeeman shifts. From $F' = 2$ decay to $F = 1$ is permitted and any such decay would result in the atom being optically pumped to a state which is far from resonance with the cooling laser and hence being lost from the trap. This can be solved by having a 're-pump' laser which addresses the $F = 1$ to $F' = 2$ transition. From the $F' = 2$ state the atom can decay to $F = 2$ where it will continue to be addressed by the cooling laser. For this reason a ^{87}Rb MOT requires two laser frequencies separated by 6.6 GHz.

Typically to successfully create a magneto-optical trap in rubidium requires a magnetic field gradient of 0.1 Tm^{-1} and the laser is red detuned by a few 10's of MHz. For stable MOTs this requires locking the lasers to a frequency reference to prevent them drifting by more than few MHz.

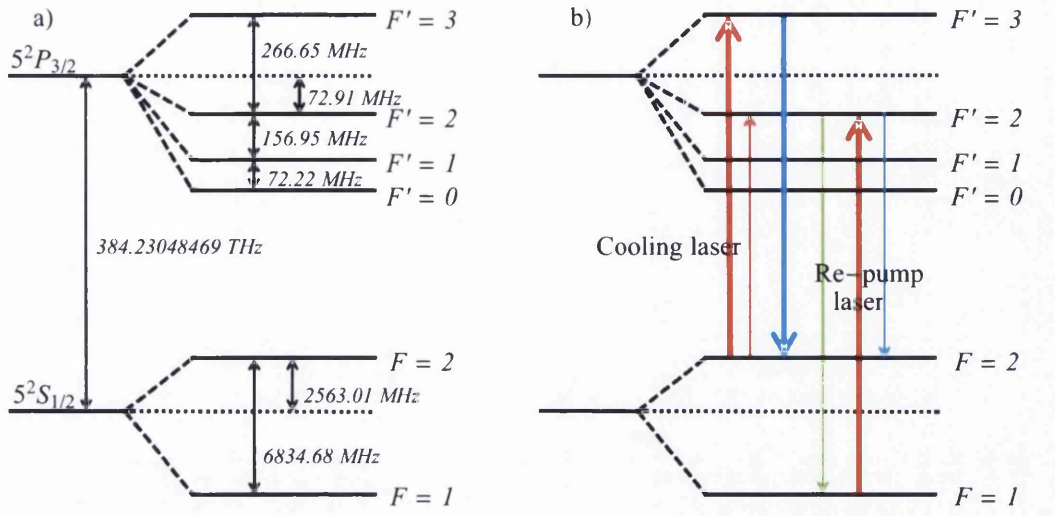

Figure 2.13: (a) Rubidium D2 line. Data taken from references [123] and [124]. (b) Transitions driven by respective lasers (thick red line), undesirable transition weakly driven by the cooling laser (thin red line), desirable transitions from the $F' = 2$ and $F' = 3$ levels (blue), undesirable decay which could cause atoms to become untrapped without a re-pump laser (green). Any atoms which fall into the lower $F = 1$ state by any other allowed routes, e.g. via $F' = 1$, are also addressed by the re-pump laser.

2.2 Experimental Setup

2.2.1 The Lasers

Three lasers are utilised: a master laser, a slave laser and a reference laser arranged as shown in figure 2.14. The master laser is a home-made extended cavity diode laser [125] in the Littrow configuration containing a Sharp GH0781JA2C edge emitting diode laser. This design utilises a diffraction grating external to the laser diode which is mounted at an angle to the laser diode such that the negative first order reflection from the grating provides the optical feedback and the zero order provides the output beam. The laser frequency can be tuned by fine adjustment of the incident angle of the laser light on the grating, which finely adjusts the wavelength of the light reflected back into the laser cavity. Following the design in reference [125] a Newport Ultima one inch mirror mount is used. The rear static part of the mount holds the laser diode and collimating lens and the grating is mounted on the adjustable front plate with the angle adjusted by a piezo electric transducer connected

to a highly stable and controllable voltage reference. Coarse adjustment can be made by hand using the mirror mount thumbscrew. The master laser was contained within a metal box where the temperature of the mirror mount assembly was internally controlled by mounting the assembly on top of a Peltier heat pump. A thermocouple on the mirror mount was monitored by a temperature controller (Wavelength Electronics MPT2500,) which adjusts the heat pump to account for changes. The laboratory was stabilised to within one degree by an air conditioning unit. These two systems combined kept the laser diode temperature stable to within 10 mK.
The slave laser had a collimating lens and the same internal temperature control system as the master laser (with a smaller heat pump) but no external cavity grating. The laser diode used for the slave laser was Sharp GH0781JA2C edge emitting diode laser. The slave laser has no grating and was primarily tuned by current adjustment.

The reference laser was a commercially built EOSI 2001 laser in the Littman Metcalf configuration [126]. The reference laser was used only to probe the output of the slave laser by heterodyning. The reference laser was modified to use up to date laser diodes with more power and was tunable over 7 GHz mode hop free with piezo adjustment. The reference laser used a Thorlabs DL7140-201S in the experiment described here, however, due to a design flaw with the current limiting diode protection electronics of the digital control unit, the diode was replaced several times during the project due to catastrophic failures.
All the lasers could be tuned to any transition of the rubidium D2 line.

2.2.2 Injection Setup

For this experiment we demonstrate the application of injection-locked semiconductor laser dynamics to atomic physics experiments. The three lasers are arranged as shown in Fig. 2.14.
The master laser was isolated from the slave laser and the slave laser isolated from the rest of the experiment to prevent back reflections causing unwanted injection effects. Light is injected from the master laser into the slave laser via the injection port of a Faraday isolator, the injection power is controlled by a half-wave plate (HWP). Polarisation of the injection beam was optimally matched to the orientation of the laser diode with an additional HWP. The reference laser beam was combined with a low power pick-off beam from the slave laser to form a heterodyne signal

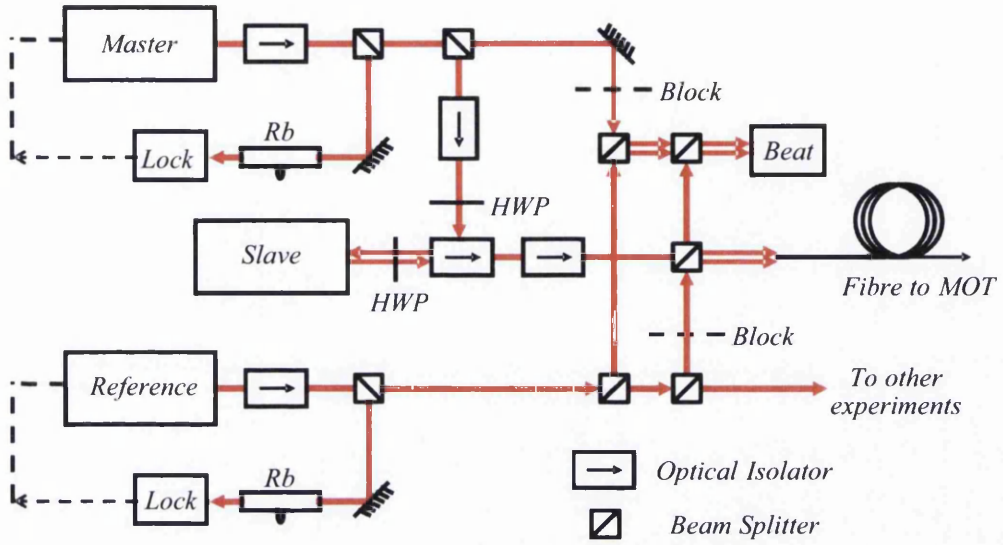

Figure 2.14: Schematic setup for the Injection Locking Experiment. The master laser couples into the slave laser via the injection port of an optical isolator. By appropriately placing beam blocks all three lasers can be combined at the heterodyne beat detector. The slave and reference laser beams are aligned into an optical fibre for the delivery of light to the MOT.

which was used for frequency diagnostics of the dynamics occurring within the slave laser. A low bandwidth (150 MHz) Thorlabs PDA10A amplified detector was used to measure the beat frequency. If the reference laser is locked to a well defined atomic transition, counting the beat frequency will give the frequency of the slave laser. It is possible to obtain linewidth information of the slave laser by measuring the beat signal using a spectrum analyser.

We can also sweep the reference laser and use the low bandwidth of our detector (150 MHz) to low pass filter the response. Peaks in the resulting heterodyne spectrum correspond to the slave laser frequency spectrum which are used for diagnostics.

2.2.3 Spectrometers and Laser Locking

The laser frequencies used in the MOT must be locked to a few MHz or better. To achieve this a polarisation spectrometer [127, 128, 129] was constructed for both the master and reference lasers. The polarisation spectrometer setup is shown in

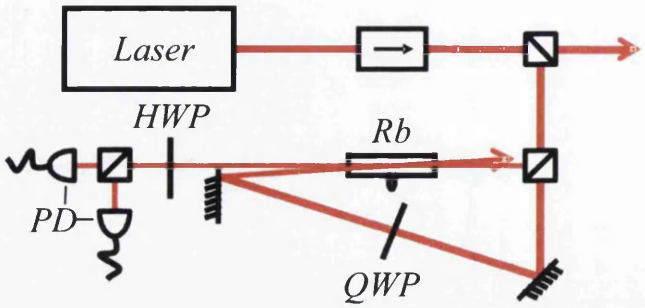

Figure 2.15: Schematic setup for the polarisation spectrometer. QWP is a quarter-wave plate.

figure 2.15.

From this spectrometer it is possible to obtain the error signal shown in figure (2.16). Conveniently the line centre of a hyperfine transition is at the centre of a steep slope which creates an error signal with a gradient of a few hundred mV per MHz. This provides an excellent signal to lock the lasers to using a simple PID circuit which feeds back to the laser piezo. Two lock boxes were made for the master and reference lasers and a circuit diagram is shown in appendix (A.3.1).

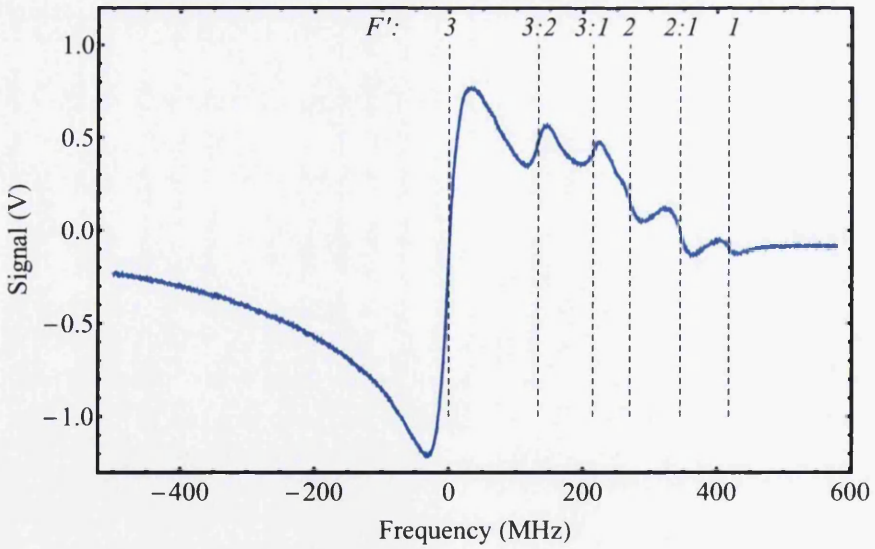

Figure 2.16: Polarisation spectroscopy output for ^{87}Rb $5^2S_{1/2}F = 2 \rightarrow 5^2P_{3/2}F'$ line. Dashed lines mark the different hyperfine levels for different F'. Crossover lines are denoted by a colon separating the two levels.

2.3 Observed Dynamics

2.3.1 Heterodyne Output

In this section examples of the different dynamical regions observed are presented. Maps such as reference [23] were used as a guide of where to look to find certain dynamical regions.

In the following images the master laser is locked to the $F = 2 \rightarrow F' = 3$ transition in ^{87}Rb except for the case of the unlocked P1 oscillation where the master laser is locked to the $F = 1 \rightarrow F' = 2$ transition in ^{87}Rb. The black trace is the reference laser polarisation spectrometer output, the blue trace is the heterodyne beat detector (offset for clarity). The reference laser can only sweep around 7 GHz at a time but the sweep can be shifted to higher or lower frequencies to check for the existence of other peaks.

Injection Locked

When the slave laser is locked by the master laser all the slave laser power is at the master laser frequency. A single peak is observed in the spectrum (figure 2.17) equal in amplitude to that of the free running slave indicating all the power is at this frequency. If the master laser is tuned in frequency (over a small range) the slave laser will follow, as long as f_i remains in the locking band.

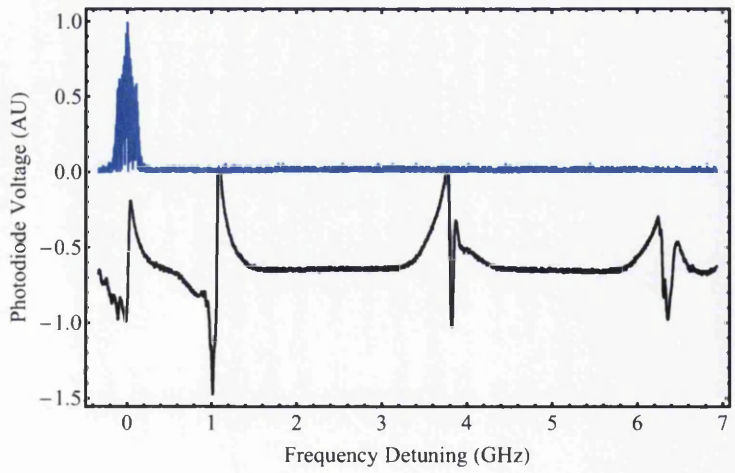

Figure 2.17: f_i =−5.2 GHz and $k = 0.23$. Locked slave laser.

Locked P1

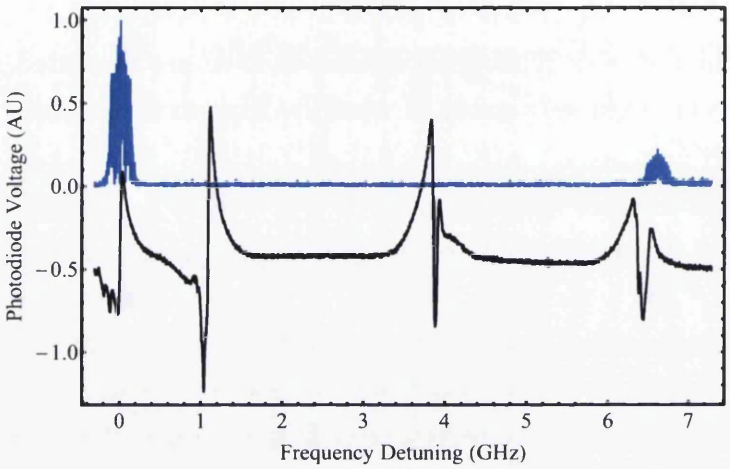

Figure 2.18: Locked P1, $f_i = -11.2$ GHz, $k = 0.14$. Master laser frequency corresponds to the large intensity feature.

A large peak is visible at the $F = 2 \rightarrow F' = 3$ lock point and a smaller peak about 6.6 GHz away. Typically the sideband intensity falls as it is detuned from the lock point but intensity can be tuned to some extent by simultaneous adjustment of k and f_i. A sideband at negative frequencies with respect to the lock point and higher order positive sidebands are observed when the sidebands are tuned closer to the lock point however at the large detunings shown in figure 2.18 they are typically barely visible above the noise level and are ignored. Hence we describe this as 'single sideband'. The sideband detunes from the lock point for increasing k or decreasing f_i.

Unlocked P1

As shown in figure 2.19 a weak peak is observed at the injection point and a larger peak representing the slave laser's frequency shifted output moves to some higher frequency. Again other peaks are below the noise level and we consider this to be 'single sideband'.

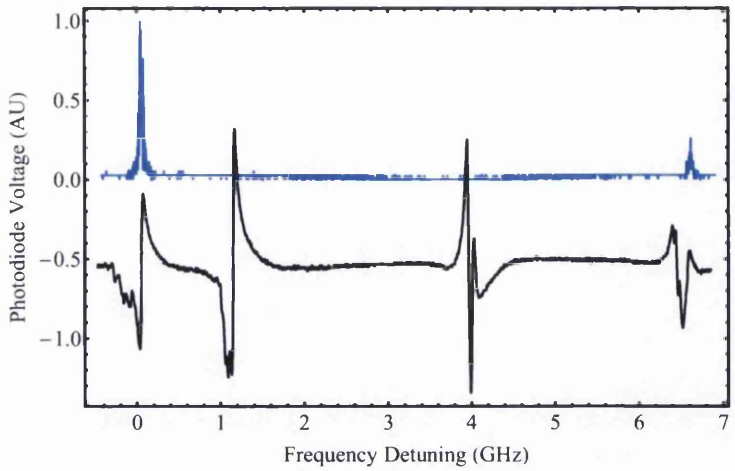

Figure 2.19: $f_i = 0.7$ GHz, $k = 0.052$. In this figure the master laser is locked to the ^{87}Rb re-pump transition corresponding to the small intensity feature. Note that this figure was taken with a different scope to the other figures presented in this section giving the apparent narrower features.

P2 Oscillation

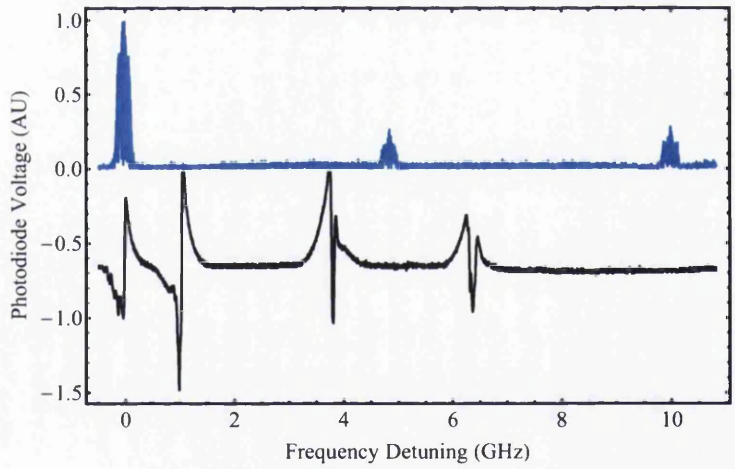

Figure 2.20: $f_i = -3.0$ GHz, $k = 0.17$. The master laser frequency corresponds to the high intensity feature, note that the image is constructed of two 7 GHz data sweeps joined together using atomic features in the reference laser spectrometer as frequency references.

Areas of P2 oscillation are usually surrounded by areas of P1 oscillation, as the oscillation changes to P2 oscillation an additional 'P2 peak' appears midway between the high intensity feature and small intensity feature. This new 'P2 peak' grows in

intensity to be less than or equal in power to the 'P1 peak'. Similar to a P1 oscillation increasing the injection power causes the low intensity peaks to tune away from the large feature which forms at the master laser injection frequency. Typically as injection power is increased the 'P2 peak' will reduce in amplitude and eventually disappear below the noise level at which point we return to the P1 oscillation.

Chaos

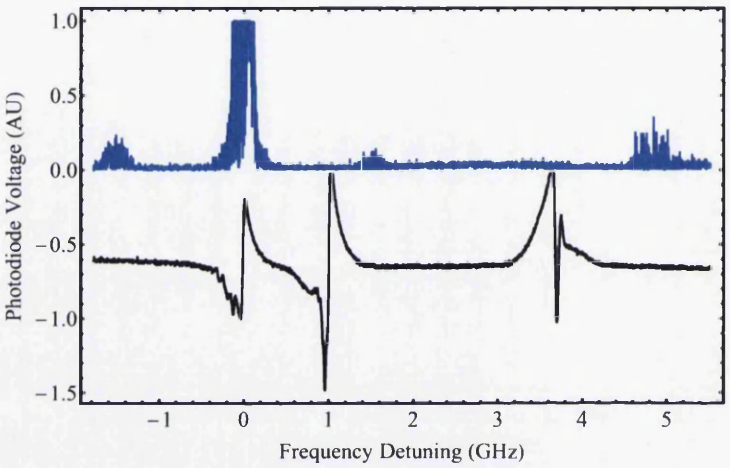

Figure 2.21: $f_i = 1.0$ GHz and $k = 0.0095$. The apparent saturation of the heterodyne signal is due to the voltage sensitivity of the oscilloscope having been reduced to clearly show the small features of the spectrum.

Chaos was somewhat hard to obtain for this laser compared to the large chaotic regions found in reference [23]. When chaos occurred the heterodyne spectrum became very noisy with irregular sidebands (figure 2.21), although it is interesting to point out that even here there is some structure to the spectrum.

Pulling Region

For very low injection (much less than the injection power required to lock the laser) a region is observed where sidebands and their harmonics are generated and are shifted in frequency (or 'pulled') towards the injection point. There are many sidebands and it possible to tune them within a few hundred MHz of the injection frequency without locking. This was used in reference [118] to create MOTs, however it is extremely sensitive to injection power and we found it impractical to tune the sidebands. Our setup was optimised to work for injection powers in the milli-watt

regime and this dynamic could only be obtained by deliberate misalignment of the injection beam, hence we were not able to attempt a MOT with this dynamic.

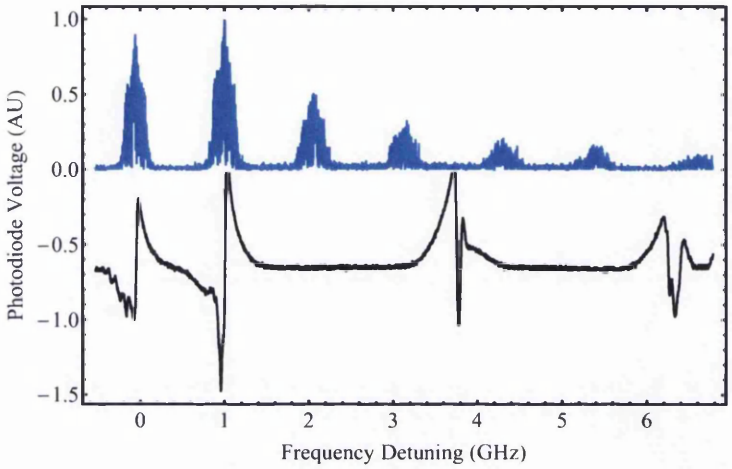

Figure 2.22: $f_i = -2.7$ GHz, $k =$ very small (less than 0.008).

Reverse Tuning Sideband P1

An additional region was observed which qualitatively appeared like a locked period one dynamic region except that the sideband moved towards the lock point for increasing k. This dynamic was observed for values of k both above and below the locking region (see the map in section 2.3.2). Above the locking region a sideband appeared which typically moved a few hundred MHz towards the injection frequency for increasing k before 'changing direction' and shifting to higher frequencies as would be expected with a locked P1 oscillation. It is unclear what causes this behaviour, however, at the turning point the sideband frequency would be less sensitive to changes in injection power because the direction change is gradual rather than sudden.

Other Potentially Useful Observations of the P1 Oscillation

Here some other observations of the P1 oscillation are noted which may be useful for other applications.

It is possible to obtain a 1:1 sideband to carrier ratio as shown in figure 2.23, however adjustment of the sideband frequency by changing either f_i or k will also adjust the amplitude of the two peaks. Tuning of the amplitude without changing the frequency must be done by adjustment of both f_i and k.

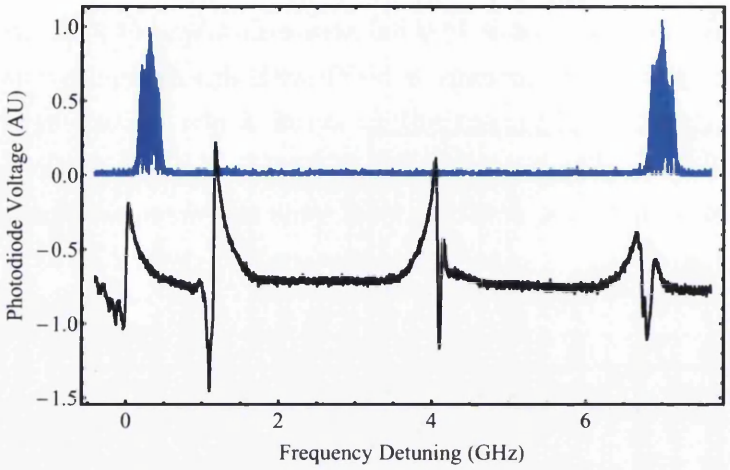

Figure 2.23: A heterodyne beat signal with a nearly 1:1 sideband to carrier ratio.

The largest sideband detuning observed in this experiment was 21.2 GHz, in our experiment this was limited by available injection power and in principle higher frequencies are possible. At this large detuning there are no spectral features to reference the sideband to for frequency diagnostics and this is far above the beat detector range. To solve this the reference laser was coupled into a wavemeter with a resolution of 100 MHz and tuned close enough to the sideband so that the beat detector could count the frequency difference between the sideband and reference laser. We found sideband frequencies of less than around 5 GHz difficult to obtain at the high slave laser bias current we used, however lower frequencies can be obtained if the slave laser current is reduced, we observed as low as 2 GHz. This is due to the sideband being a result of the undamped RO frequency which reduces for lower bias current. The frequency at which the P1 sideband first appears for increasing k is approximately the relaxation oscillation.

2.3.2 Mapping the (f_i,k) - Plane

The dynamics described above were mapped out for various f_i and k over a small region. The master laser was locked to the ^{87}Rb $F = 2 \rightarrow F' = 3$ transition and f_i set at a fixed measured value, the injection power was then increased from the minimum. When the slave laser was on the boundary between dynamical regions the slave power P_s and the injection power P_{Inj} were measured. A boundary is defined as occurring when the features of the new dynamic are visible above the noise on the beat signal, note that the boundaries were always recorded for increasing k.

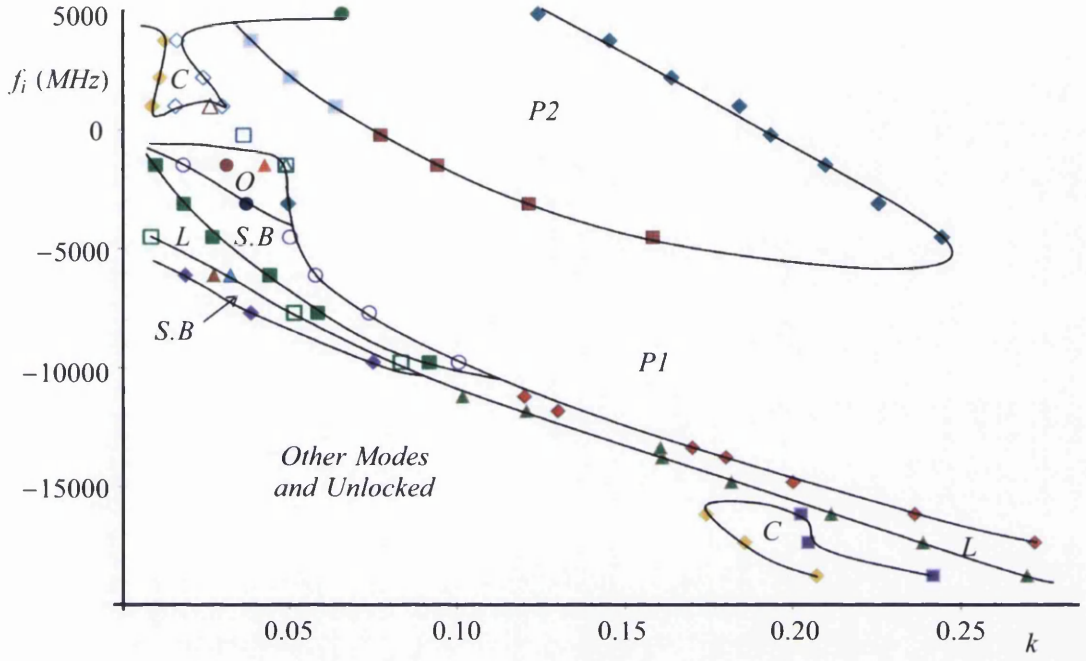

Figure 2.24: Regions are denoted as follows: L = Locked, C = Chaos, P1 = Locked or Unlocked Period one limit cycle, P2 = Period two limit cycle, S.B = Reverse tuning sideband P1, O = Other dynamical regions. All points are measured boundaries however the black lines joining the points are simply to guide the eye. The pulling region is not shown as this required misalignment of the injection beam to obtain a weak enough injection signal, it occurs between the y-axis and the points recorded for the lowest k.

Distinct dynamical regions are observed, most notably in the narrow band of locking which requires increased amounts of injection power for larger absolute detunings. The locking band precedes a large region of P1 and P2 oscillation which dominates the map. This map follows the same general trends as references [23, 21].

Towards the bottom left of the map is a region denoted 'Other Modes and Unlocked' where the small injection or large master-slave detuning simply cause the laser to; mode hop, shift slightly in frequency or to not to change at all. Since these regions are largely un-interesting and it is often difficult to tell whether the laser has mode hopped or simply frequency shifted, this region was not studied in detail. The reverse sideband feature was observed on both sides of the locking band. The

slightly larger region at higher k and lower f_i created a sideband which, at the P1 boundary, changed its motional direction in frequency with respect to increasing k. The region of other dynamics ('O') contained a mixture of other dynamics in small regions which could not be resolved on such a coarse grained map, and some which did not appear to fit into the categories described in the section above or could not be determined. Further work would be required to identify these regions accurately.

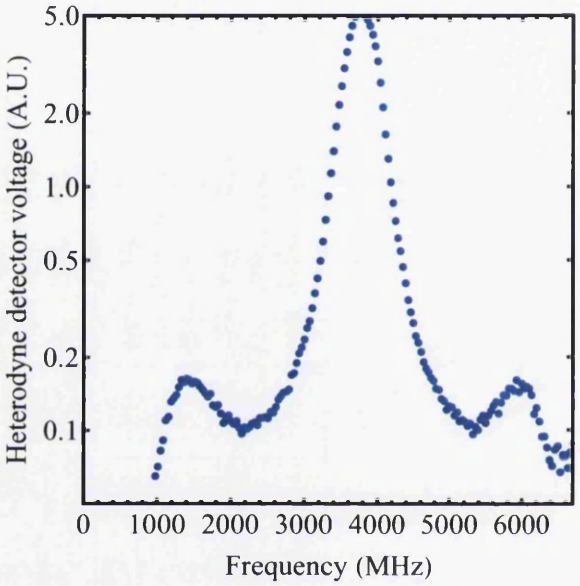

Figure 2.25: The beat detector spectrum showing the RO frequency.

2.3.3 Estimating the Relaxation Oscillation

As discussed in section 2.1.1, the free running slave laser relaxation oscillation (RO) frequency is related to the square root of the stable lasing intensity I_S however the oscillation amplitude becomes suppressed as the bias current is increased.

The beat detector can be used to find the relaxation oscillation of the free running slave laser for lower bias currents, and by extrapolation we can estimate the RO frequency at the bias current used in the experiment.

One hundred sweeps of the slave laser sweeping over the rubidium D2 line were recorded by the heterodyne detector and these were averaged to try to see the relaxation oscillation. An example is shown in figure 2.25, the large central peak indicates the main lasing mode and the weak sideband is the relaxation oscillation. Above approximately $I = 55$ mA no RO signal was observed, however weak peaks

were observed for lower currents. The RO frequency for various bias currents are plotted in figure 2.26. This graph extrapolates up to the bias current used to create a P1 oscillation suitable for creating a magneto-optical trap, in this experiment a bias current of 2.6 times the threshold current (I_{THR}) was used. $I_{THR} = 30.7$ mA. The fitted line in figure 2.26 gives a RO frequency of approximately 4.1 GHz.

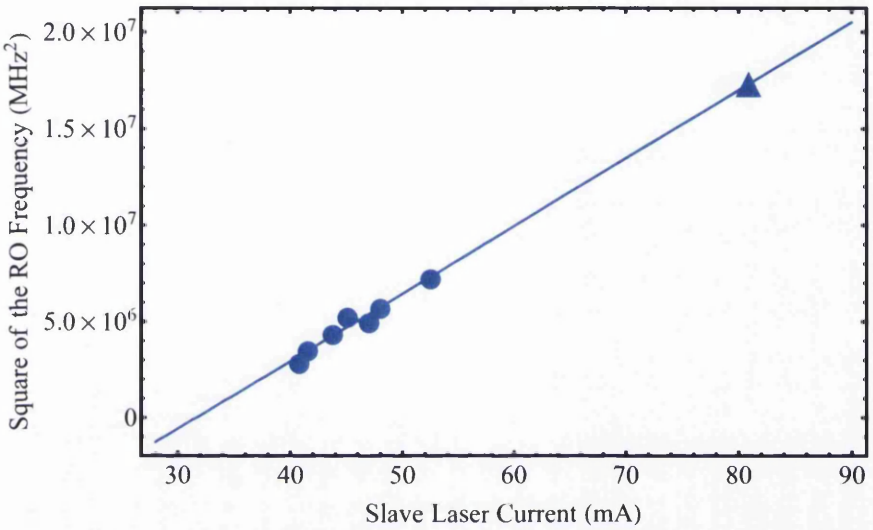

Figure 2.26: The square of the relaxation oscillation of the slave laser as a function of current. Circles indicate datapoints, the triangle indicates the operating region of the laser for the experiment described in section 2.4.

2.3.4 Estimating the Alpha Factor

The boundary between the locking band and the P1 region, known as the Hopf bifurcation line (see section 2.1.4), can be used to determine the alpha factor as described in reference [130]. Due to our slave laser being optimised for higher output power we did not have sufficient injection power to find the Hopf minimum at the slave laser's normal operating power. The laser was therefore increased in temperature and decreased in current to reduce output power of the slave laser whilst keeping the frequency close to the rubidium D2 line. Since $k = P_{Inj}/P_{SL}$, the range of k was increased by the reduction in slave power. The current was reduced to just above threshold at $I/I_{Thr} = 1.5$. Coordinates of f_i and k were recorded for the Hopf bifurcation line, these are plotted in figure 2.27. Points are joined by an interpolating line which is simply to guide the eye.

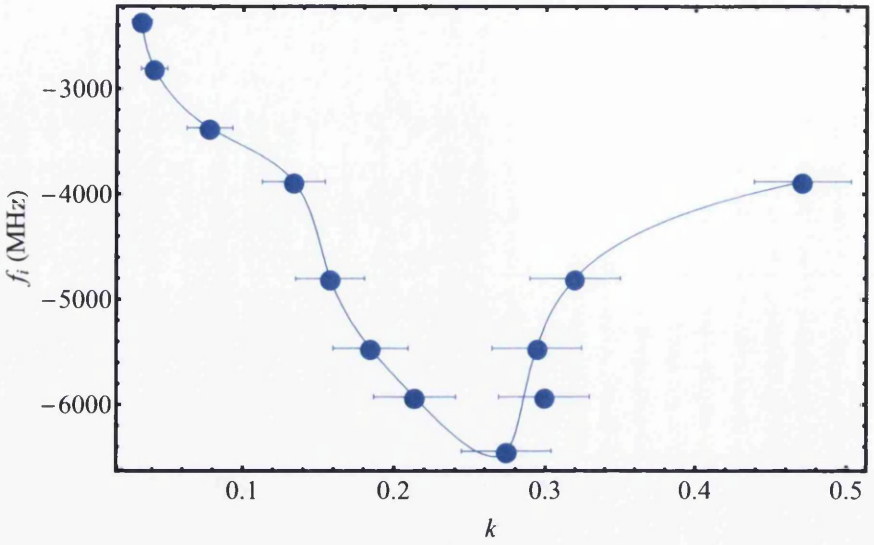

Figure 2.27: Plot of the Hopf bifurcation line. Boundaries between locked and P1 regions were recorded and joined with a line which is just to guide the eye. In the region above the points the slave laser is in a P1 region, below the line the slave is injection locked. The error bars are the result of uncertainty in determining the injection power at which the boundary occured.

The injection power was varied by adjustment of the half wave-plate, and this is now a more coarse adjustment of k than at higher laser bias current. The laser power is also lower giving a lower heterodyne beat signal which makes determination of the boundary point more difficult, for these reasons the boundary positions on the k axis are given to the nearest one degree increment of the waveplate. The large k-axis error bars arise from this resolution uncertainty.

Figure 2.27 shows a minimum in f_i, defined as f_{min}, at -6.4 GHz. From reference [130] we can relate this minimum to the approximate value of the alpha factor using the equation:

$$\frac{f_{min}}{\omega_{RO}} \simeq -\sqrt{\frac{(\alpha^2-1)^3}{32\alpha^2}} \tag{2.30}$$

The negative square root is a consequnece of the Hopf minimum occuring at negative detunings.

Using equation (2.30) and the value of the RO frequency determined from figure 2.26 we can estimate our alpha factor to be approximately $\alpha = 4$.

2.4 MOT Using the P1 State

In this section the application of the P1 oscillation to atomic physics will be demonstrated by using this to create a magneto-optical trap. This will be done for a range of detunings and shown to not affect the number of atoms loaded into the trap when compared with a MOT made in the conventional way of using two laser.

2.4.1 Setup Details

A large amount of the slave laser beam was coupled through a polarisation preserving fibre into the magneto-optical trap (MOT) setup. At the exit of the fibre the beam was collimated using a Thorlabs F810APC-780 fibre collimation package which has a specified $1/e^2$ output beam diameter of 7.5 mm. This beam was spilt into three beams of equal power which were retro-reflected to create six beams intersecting at the minimum of a quadrupole magnetic field with an axial field gradient of 1.1 mT/cm within a vacuum. The magnetic field was created by two identical coils in the anti-Helmholtz configuration. The coils had; 320 turns, an inner radius of 62.3 mm, an outer radius of 72.0 mm, a height of 17.9 mm and were separated by 38.1 mm at their closest face. Details of the vacuum system and bakeout procedures can be found in appendix A.1.1. A schematic of the laser setup for the MOT is shown in figure 2.28.

The dispenser and MOT coil currents are controlled by MOSFET and power op-amp circuits respectively which in turn are controlled by an analog output from a computer card. The circuits designed for control of these components are detailed in appendix A.3.2.

MOT fluoresence is collected by a lens which is approximately 5 cm away from the MOT and focussed onto a photodetector (Thorlabs PDA055), the fluorescence can then used as a measure of the number of atoms in the trap. The fluoresence light also has to pass out of the vacuum through a vacuum viewport which is not anti-reflection coated. This means only around 5% of light emitted from the MOT is collected by the fluorescence detector. The voltage from the photodetector is recorded by the same computer which controls the dispensers and coils.

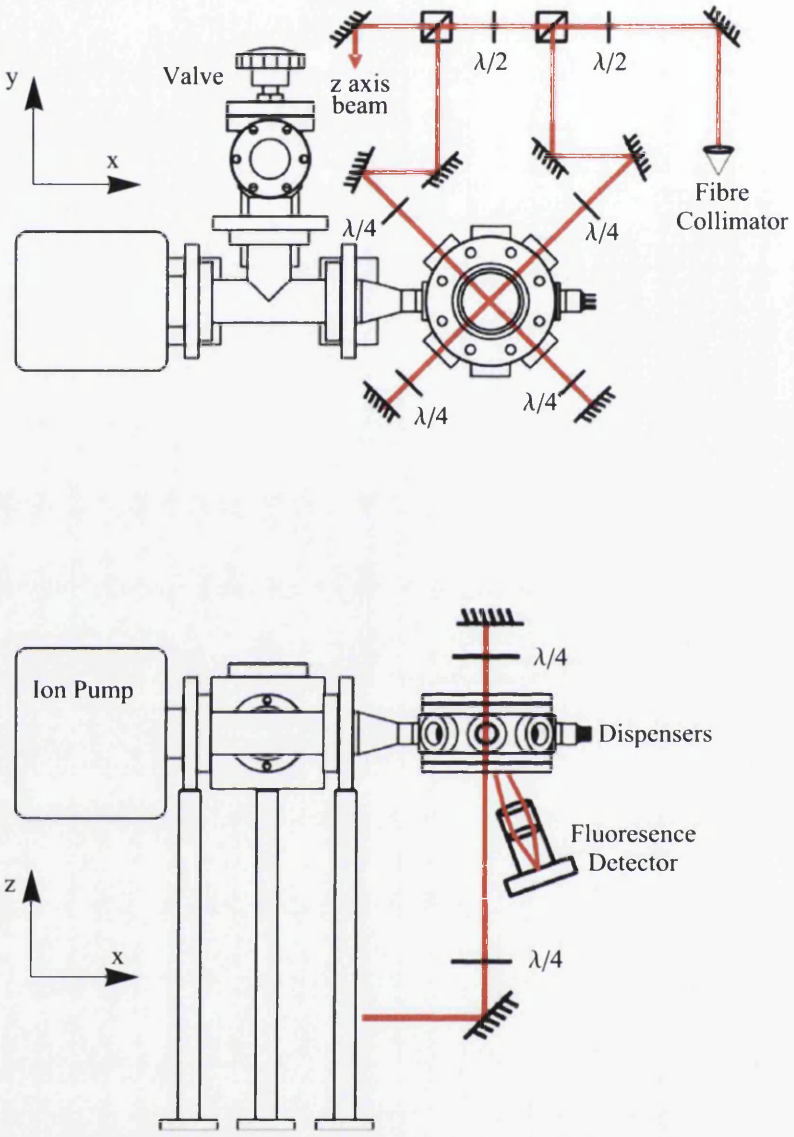

Figure 2.28: Top and side views of the vacuum system with a schematic of the MOT laser setup.

2.4.2 Unlocked P1 MOT

A P1 oscillation can be created with either a locked or unlocked slave laser as shown in section 2.3. A P1 state with an unlocked slave laser can be created by

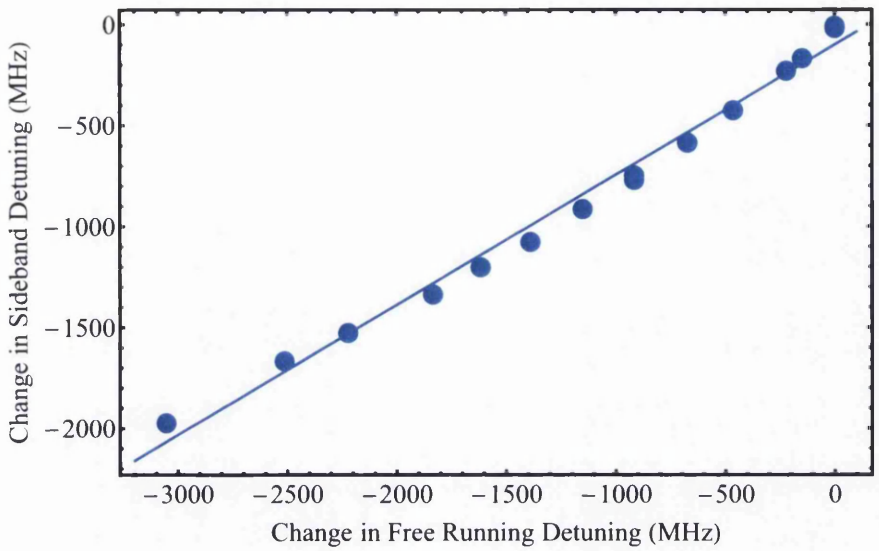

Figure 2.29: Change in frequency of the sideband relative to the change in frequency of the free running slave laser. The gradient of the fitted line is 0.64 GHz per GHz.

setting k to be 0.052 and f_i to be 0.7 GHz. The master laser is locked to the ^{87}Rb $5s^2S_{1/2}(F = 1) \rightarrow 5p^2P_{3/2}(F' = 2)$ transition known as the re-pump transition.

A weak feature is visible at the injection frequency and a stronger feature - the shifted slave laser frequency - appears at some shifted frequency f_s. This strong feature can be tuned by adjustment of either f_{SL} or k.

For the unlocked case the high intensity feature appears to be somewhat unstable and constant adjustment was needed to keep this at the desired frequency. In our experiment adjustment of k is by mechanical adjustment of a waveplate angle and hence we find it far easier to fix k and finely adjust f_{SL} by small adjustment of the laser current (< mA). This can easily be done electronically by applying a small DC voltage to the modulation input of the slave laser current driver. Using the above method the waveplate adjustment k becomes a coarse adjustment and the adjustment of f_{SL} a fine adjustment. Over a 3 GHz range we find f_s tunes approximately linearly with the slave laser free running frequency $\Delta f_s/\Delta f_i = 0.64$ GHz/GHz.

The reference laser was now locked to the ^{87}Rb $F = 2 \rightarrow F' = 3 : 2$ crossover peak, which is 133 MHz away from line centre of the $F = 2 \rightarrow F' = 3$ cycling transition. This reference frequency was chosen because it is within the 150 MHz bandwidth of the heterodyne detector. The red detuning of the P1 sideband frequency was varied to see how this affects the number of atoms in the trap. With the reference laser

locked to a well defined point in frequency space we can use the beat count between the reference laser and slave laser to tune the high intensity feature to any desired red detuning. This is done by applying a small DC signal to the modulation input of the slave laser current driver. Using this tuning method the high intensity feature is tuned to various red detunings of the ^{87}Rb $F = 2 \rightarrow F' = 3$ transition to provide the MOT cycling transition light and the low intensity feature is used to provide the re-pumper. The spectrum is now as shown in figure 2.19 and this light is now used to make MOTs for various detunings. The beat frequency is monitored during an experiment run.

With the lasers tuned and locked as described above MOTs can be created by dispensing a pulse of rubidium atoms at natural abundance from a getter source [121, 122] which was run at 8 amps for 10 seconds. The dispensers and coils are controlled by computer for better repaetability. Fluorescence from the MOT is focussed onto a photodetector which can then be used as a measure of the number of atoms in the trap. Several minutes were allowed to pass before repeating the experiment to ensure the ion pump had removed all background rubidium from the system. During this time the dispensers were kept hot by running them at 2 A which is insufficient current to cause them to dispense but enough to keep them hot. This prevents dirt buildup on the dispensers and also makes them start dispensing faster.

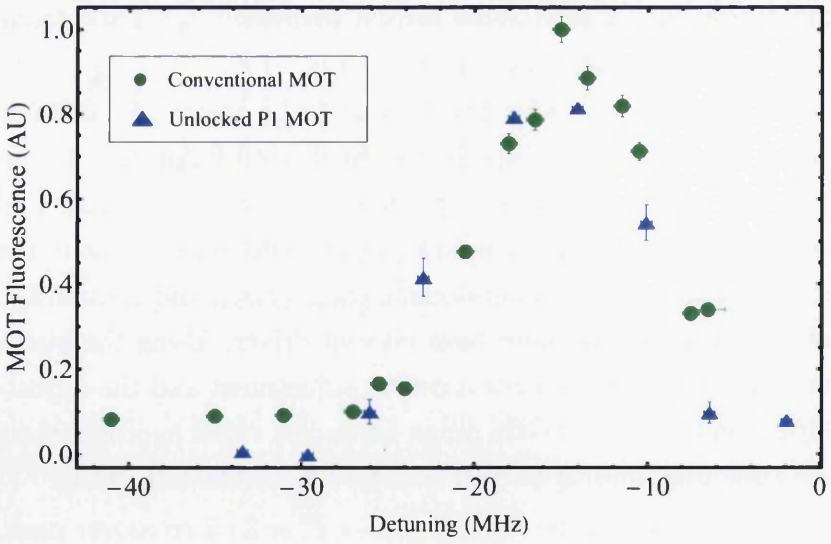

Figure 2.30: Maximum MOT fluorescence Vs detuning from the $F = 2 \rightarrow F' = 3$ line.

For comparison MOTs were also created in the conventional way of using seperate

lasers for the trap and re-pump light, in this case the cycling transition came from a stable injection locked slave laser without sidebands and the re-pump from the reference laser. In figure 2.30 the detuning is plotted against the maximum number of atoms loaded into the trap during a dispenser pulse.
The frequency instability of the high intensity feature causes the largest error bars for the MOT fluoresence to be on the sides of the distribution, where a small change in frequency can have a large effect on the number of trapped atoms. The dominant source of uncertainty for the other points arises from the normalisation of the data to account for laser power lost into the sidebands (see section 2.4.4).

2.4.3 Locked P1 MOT

MOTs were also created with a P1 oscillation from a frequency locked slave laser. f_i is set to -11 GHz and injection power to 6.9 mW which gives $k = 0.14$, the master laser is now locked to the ^{87}Rb $5s^2S_{1/2}(F = 2) \rightarrow 5p^2P_{3/2}(F' = 3)$ cycling transition. With the injection parameters described above a high intensity feature forms at the injection frequency and a low intensity feature forms at the re-pump transition. Note that these injection parameters are still positive with respect to the Hopf bifurcation line and hence injection power would have to be reduced to remove the sidebands. The laser spectrum is as shown in figure 2.18. The high intensity feature is the injection locked slave laser frequency which coincides with the master laser frequency. The low intensity sideband is caused by the master-slave beat frequency causing the relaxation oscillation to become undamped and shift to higher frequencies. The slave laser spectrum is qualitatively indistinguishable from the unlocked case shown in figure 2.18. The low intensity sideband can be tuned by adjustment of k or f_i and both can be tuned to many 10's of GHz. The power ratios between the two peaks are also tunable by simultaneous adjustment of k and f_i.
Fine tuning of the high intensity feature is done by applying a small offset to the polarisation spectrometer signal to move the lock point of the master laser which can be done via the lock circuits. This is done with the reference laser locked to the $F = 2 \rightarrow F' = 3 : 2$ crossover and hence by counting the beat frequency between the slave laser and reference laser it is possible to determine the red detuning for the MOT cooling frequency. The low intensity feature can now be tuned by locking the reference laser to the $F = 1 \rightarrow F' = 1$ transition and again counting the beat frequency between the slave and reference it was possible to check that the

low intensity sideband was at the re-pump transition. Tuning of the low intensity sideband was done by simply tuning the coarse HWP adjustment of k. Partly because, for the locked case, f_s seemed to be less sensitive to changes in f_i and also the re-pump light is insensitive to fluctuations of the order of a few MHz, this meant k could be left for periods of hours or more without adjustment and MOTs could still be created. The sensitivity of f_s to k was found to be 0.29 GHz/mW (figure 2.32).

Control of the MOT coils, dispenser and fluoresence photodetector used the same control sequence described for the unlocked P1 MOT.

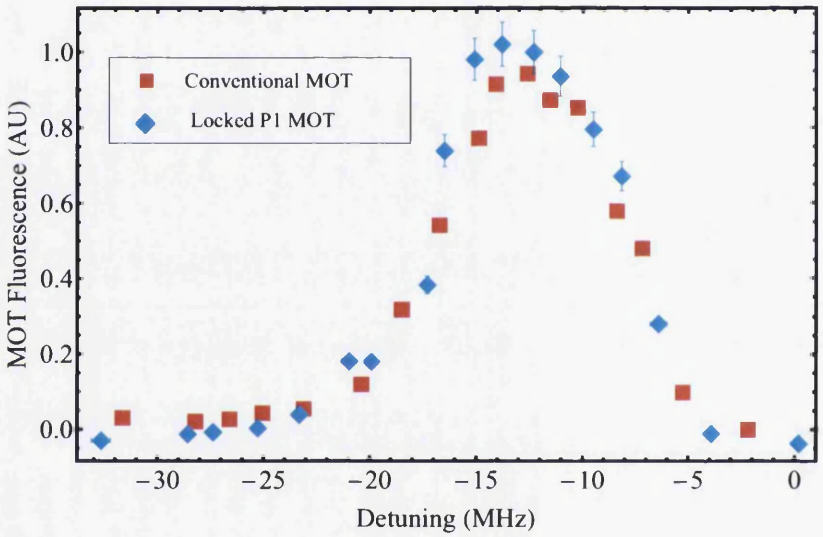

Figure 2.31: Peak MOT fluorescence Vs detuning from the $F = 2 \rightarrow F' = 3$ line.

The above procedure was repeated several times to create MOTs made with the locked P1 oscillation for various detunings as shown in figure 2.31. Similar to the unlocked case, data is also compared with MOTs made with separate cycling and re-pump light. Seperate cycling and re-pump light was made by injection locking the slave at the cycling transition without sidebands and using the reference laser to provide re-pumping light.

Like the unlocked P1 MOT the error bars shown in figure 2.31 are once again predominantly caused by uncertainty in the normalisation of the number of atoms detected which accounts for power lost to the sideband and power variations in the MOT.

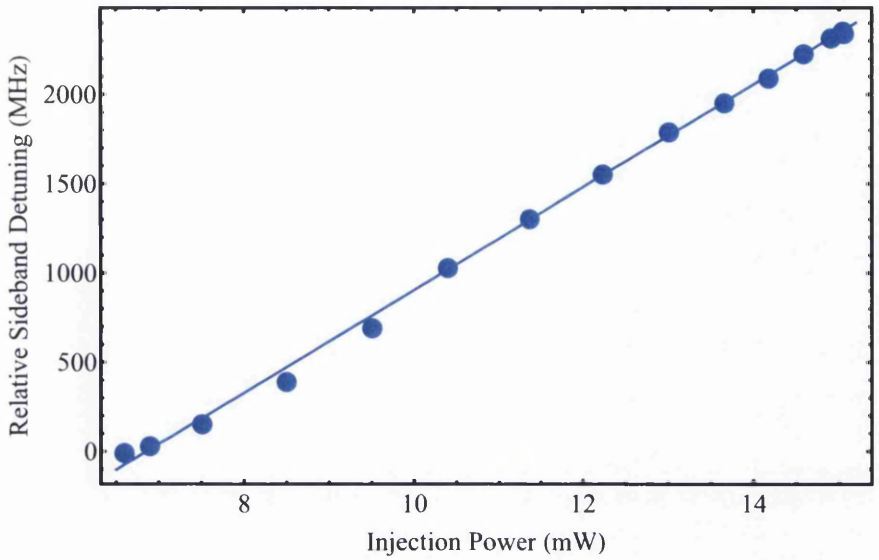

Figure 2.32: Change in frequency of the locked P1 sideband relative to the change in injection power. The gradient of the fitted line is 0.29 GHz per mW.

2.4.4 Normalisation of Atoms in the Trap

For the P1 oscillation the data points are normalised to account for the power lost into the low intensity feature and day to day variations in power coupled through the fibre. Using separate cycling and re-pump light the cycling power was varied to check that this was linearly related to the number of atoms trapped (fluorescence) and used to find the minimum power required to create a MOT. Power lost to the sideband was determined from the peak amplitude of the heterodyne beat frequency, using a locked slave laser the amount of power which went to the heterodyne detector was varied to confirm this amplitude was linearly related to power. Normalisation of the data required precise measurements of the power in the MOT and of the heterodyne beat amplitude, uncertainty of these measurements was the dominant source of the uncertainty in the y-axis of figures 2.31 and 2.30.

2.4.5 Linewidths

The linewidth of each optical frequency component used to make the MOT were measured using a beat frequency measurement between the slave laser and a reference laser locked to an arbitrary nearby atomic line feature. Using an RF spectrum

analyser we can extract single linewidth traces to which a Lorentzian distribution is then fitted. Images of the data and fitted Lorentzian are shown in figure 2.33. The linewidth values from several single traces are averaged to find a mean. The instrument linewidth, given by the beat of the master laser with the reference laser, was 1.143 ± 0.017 MHz. The uncertainties given are the error in the fitted Lorentzian linewidth however individual measurements are limited by the resolution of the spectrum analyser which was 100 kHz.

We first measure the free running slave laser full width half maximum (FWHM) linewidth of (2.916 ± 0.023) MHz. This is already narrow for a laser without grating stabilisation, this is due to the high bias current used and low temperature which reduce the linewidth [120].

When optical injection produces an unlocked P1 oscillation we find a linewidth of (1.000 ± 0.015) MHz for the low intensity feature (at the injection frequency) and (1.739 ± 0.032) MHz at the high intensity feature. For the locked P1 the linewidth was (1.317 ± 0.016) MHz for the low intensity feature and (1.226 ± 0.030) MHz for the high intensity feature (now the injection point).

In figure 2.33 the unlocked high intensity feature appears somewhat noisier than the other peaks, this is due to it being less stable in frequency and tending to drift rapidly during data collection. The spectrum analyser sweeps 1.6 MHz/ms. Figure 2.33(g) clearly shows that the linewidth of all optical features reduce when the slave laser is subject to optical injection. When the slave laser is free running we expect spontaneous emission into the free running slave laser mode to be the dominant source for lasing, but when light is injected into the slave laser cavity the source becomes increasingly dominated by the master laser spectrum [119] which also acts as a phase reference, hence in the locked P1 case both optical frequencies reduce in linewidth.

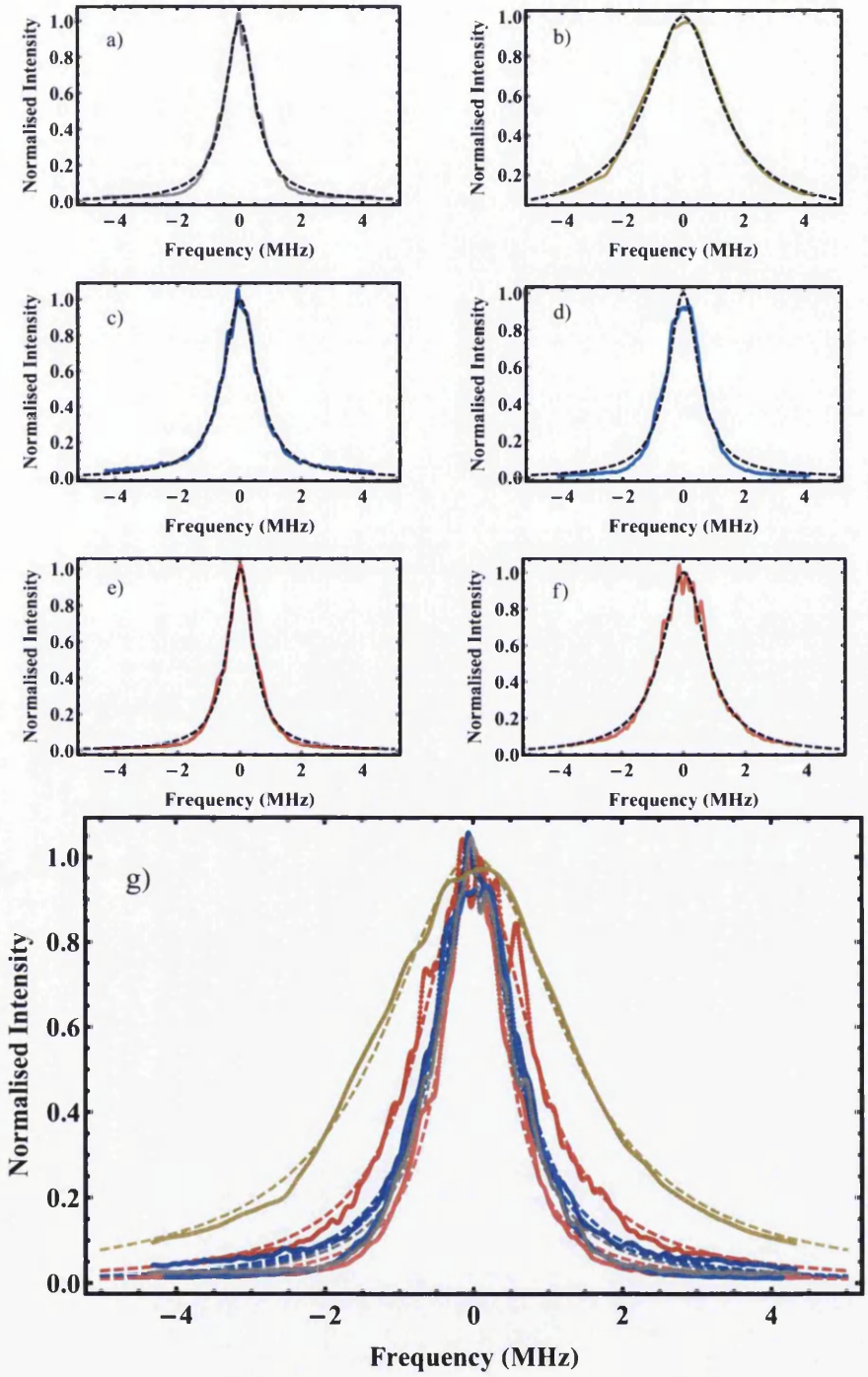

Figure 2.33: Data (solid lines) and Lorentzian line fits (dashed lines). (a) The instrument linewidth (beat of the master laser with the reference laser), (b) The free running slave laser, (c) Locked P1 low intensity feature, (d) Locked P1 high intensity feature, (e) Unlocked P1 low intensity feature, (f) Unlocked P1 high intensity feature, (g) All plots combined into one to show the linewdith reduction. All data has been normalised to an amplitude of 1.0 for ease of comparison.

In our P1 oscillation the relaxation oscillation becomes undamped and does not contribute significantly to the linewidth. The linewidth of the small feature in the unlocked case is expected to be narrow because this is the injection point for the master laser light, however the reason we also observe some linewidth narrowing for the high intensity feature is less well understood because for the unlocked P1 case the phase is not locked (not bound). One possible but speculative reason for this is that we may be near a boundary between a bound phase and unbound phase P1 oscillation [22]. The boundaries between the two are not precisely known meaning the master may be acting as a partial phase reference. This partial phase reference may also explain why this feature is not quite as narrow as the others.

We attempted to test the narrowing effect for a slave laser with a broader starting linewidth by increasing the slave laser temperature and decreasing the current. Again the linewidths reduce to approximately 1 MHz when injected, however at these conditions the slave laser is less stable and possibly near a mode-hop. With a free running slave laser linewidth of approximately 21 MHz the linewidth reduced to 0.802± 0.004 MHz for the locked high intensity feature and 1.177±0.005 MHz for the low intensity feature. The corresponding numbers for the unlocked case were 1.559± 0.004 MHz and 0.813± 0.004 MHz.

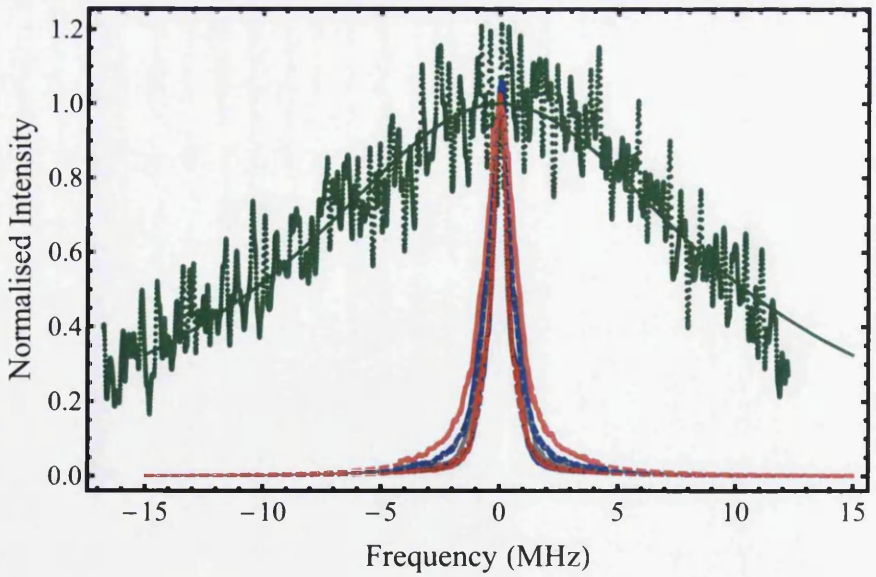

Figure 2.34: Linewidth reduction from a broad free running slave laser (green). Data is shown with Lorentzian fits, red and blue are the optical features of the locked and unlocked P1 oscillation as described for figure 2.33.

The data is shown in figure 2.34 with corresponding fits. The free running slave laser data now appears very noisy, due to instabilities in the laser which are apparent due to the slow scan speed of the spectrum analyser.
In conclusion the linewidth narrowing makes the optical frequencies under discussion here well within the natural linewidth of many atomic transitions commonly used in atomic physics experiments.

2.4.6 P1 MOT Experiment Remarks

The data for the locked P1 and unlocked P1 were taken on different days with somewhat different MOT alignments which is suspected to be the reason for slightly broader distribution in figure 2.30 than in figure 2.31. The two data sets clearly show that normalised MOT fluorescence data does not show a noticeable difference in the number of trapped atoms in the MOT when P1 oscillation light is used instead of separate lasers. MOT fluorescence during loading of the MOT also shows no noticeable difference.
It can then be concluded that apart from the loss of power into the sidebands P1 oscillation light traps atoms just as efficiently as ordinary MOT light. The measurements also demonstrate that making a MOT using the locked P1 oscillation as described above is possible without active stabilisation of the injection power or detuning, however in the unlocked case constant adjustments were required to maintain the appropriate frequencies for atom trapping. Both the locked and unlocked P1 could be made more stable by detecting the heterodyne beat frequency on a fast photodetector and stabilising the beat frequency to a good microwave oscillator [131, 132, 133] which uses feedback to adjust either k or f_i. It is suggested adjustment of f_i would be easier because this is done by small adjustments to the slave laser current which can easily be done on sub-microsecond timescales.

2.5 Potential P1 Oscillation Applications and Notes

2.5.1 Operation Without a Reference Laser

The reference laser provides a beam at a well defined frequency for which the slave laser output can be studied either by sweeping the reference over several MHz or locking it to an atomic line and counting the beat frequency. However if the beat

detector was fast enough to count over 7 GHz and a spectrum analyser with 7 GHz was available there would be no need to sweep the reference laser, potentially the master laser beam could be used as the reference beam also. Using a simple beat locking circuit which stabilises the slave to an external reference [131, 132, 133] and controls either f_i or k, the unlocked features of the P1 oscillation could be stabilised. This convenient setup would use two lasers and could provide a convenient way to rapidly and controllably tune laser frequencies because the switching bandwidth is limited only by the dynamical frequency of the laser which is of the order of the P1 oscillation. For example, the rapid tuning could be used in a cold atoms experiment to create the optical frequencies required for optical pumping, imaging or molasses steps from one optically injected laser. It would also be possible to turn off certain optical frequency components by moving into a locked slave laser regime, e.g. by rapidly reducing the injection power when using the locked P1 oscillation used in the experiment above. A schematic setup is shown in the figure 2.35.

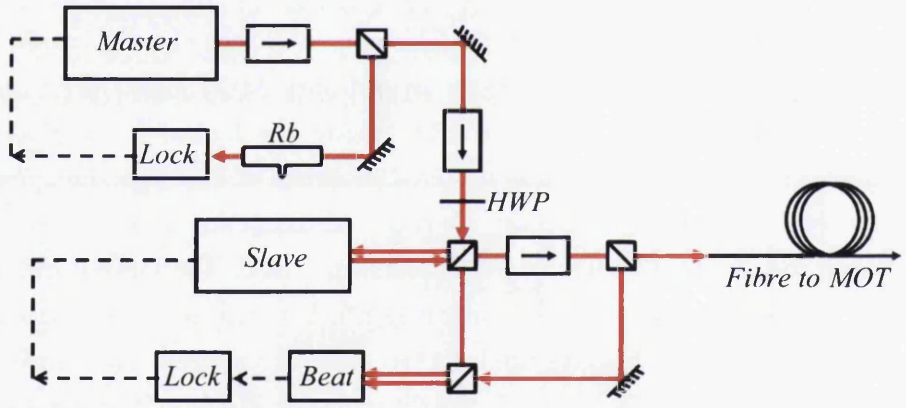

Figure 2.35: Schematic setup of a slave laser beat locked to the master laser, hence not requiring a reference laser.

This setup would have been ideal for use in the magnetic trap described in the next chapter if equipment capable of counting 7 GHz frequencies had been available at the time. This was not the case but would be a desirable development to the setup for the future. Although such detectors and oscillators for such a beat lock may be expensive the reduction in the required number of lasers and optics would make this financially favourable.

2.5.2 Other Applications of the P1 State

Since the optical frequencies of the P1 oscillation are derived from the same laser the polarisation is the same for all frequency components making delivery to an experiment very efficient. This would be particularly useful for any single beam scenarios such as the tetrahedron [115] and micro-pyramid [134] where the two optical frequencies could travel co-linear. Within our measurement precision the linewidth reduces to that of the master laser and so using a narrower linewidth master laser should create narrower frequency components, however better frequency stability may be required to observe this narrowing. As described above this could be achieved by using a beat-locked laser stabilised to another stable reference laser.

Off resonant frequency stabilisation would be possible as long as there is a reference transition some GHz away, this is comparable to locking which has be achieved using the Faraday effect [135] over a range of 6 GHz to 14 GHz. In principle the tuning speed of the frequency sidebands are only limited by the dynamical frequency of the slave laser [100] which is of the order of the shifted RO frequency (the P1 oscillation frequency, which is of the order of GHz) and hence very fast switching should be possible. This makes the setup ideal for an experiment where the laser must tune very quickly. The frequency tuning range of the sideband is limited by the free spectral range of the laser beyond which the single mode model of the laser no longer applies [100]. Experimentally P1 oscillations of 100 GHz have been observed [136], far exceeding those obtained by direct current modulation.

Electro-optic modulators (EOMs) or accousto-optical modulators (AOMs) can be used to modulate amplitude and frequency. AOMs typically only operate in the MHz range. EOMs create sidebands similar to those observed in our P1 oscillation, however the tuning of amplitude and frequency is more difficult and single sidebands are not possible. Our P1 oscillation could easily replace an EOM to create these fully tunable sidebands, and unlike an AOM or EOM our injected laser could also amplify the light intensity injected from a low power master laser. Typically for an EOM and AOM the insertion loss is of the order of 4 dB and 1.5 dB respectively. Total laser power could easily be amplified to the 1 W regime with a tapered amplifier seeded from the slave laser.

The P1 oscillation would be an ideal light source for two photon processes such as stimulated Raman transitions where two laser frequencies separated by some GHz are required, this could be used for Raman laser cooling techniques capable of

optically cooling to 100 nK [137]. High degrees of coherence between the two laser frequencies are possible, and setups with linewidths of 1 kHz for the P1 oscillation frequency itself have been demonstrated [138].

Stimulated Raman transitions in the range of the P1 oscillation have been used to optically transfer heteronuclear molecules to a vibrational level of the ground state, for instance in $^{40}K^{87}Rb$ [139]. The P1 oscillation could be used for this setup and would be particularly desirable for frequencies which are difficult to attain by other methods and could give narrow linewidths of 1 kHz as described above, however due to the pulsed nature of the separate frequencies additional AOMs and optical filtering would be required for this application.

The P1 oscillation offers an attractive method for addressing multiple molecular transitions with tunable narrow band laser light as long as resonant diode lasers can be sourced. For example, it may be possible to laser cool heteronuclear molecules such as CaF using vibrational states and two frequencies separated by 62 GHz which is well within the 100 GHz range discussed above [140].

Chapter 3

Creating a Cold Magnetically Trapped Cloud

3.1 Experiment Motivation

This chapter describes the construction of a magnetic trap which is demonstrated to work for atoms pre-cooled in a MOT even without optical pumping or a molasses step. This is the first step on a larger experiment which aims to create a cold ^{87}Rb-^{40}K mixture which could be used to model quarks inside an atomic nucleus [141]. Using cold atoms to model quarks requires tuning the interaction strength between atoms which can be achieved using magnetically induced Feshbach resonances (see section 3.2.5), and detection with single atom sensitivity.

The magnetic trap requires a strong quadrupole magnetic field and the Feshbach resonances require a strong uniform magnetic field, however, one set of coils were designed which could create both fields, this necessitates coils which can switch in millisecond timescales. The coils were further specified to also provide a weak quadrupole field to create the MOT.

An additional goal of this experiment is to interact with cold atoms using tapered nanofibres. Tapered nanofibres are optical fibres which have been heated and stretched until a tapered section occurs which has a width of the order of the wavelength of the light without significant loss in transmission. Part of the light wavefunction now propagates outside of physical extent of the fibre which continues to act as a waveguide. The size of the mode which is outside the fibre is comparable to the resonant atomic scattering cross section which gives a high probability of

interaction between the photon from the fibre and the atom and hence these fibres can be used for single atom detection [142]. The production of these fibres and their characterisation was not part of this project however it did strongly influence the vacuum chamber design.
The aim of this project was to design and construct one system which could meet all these requirements.

3.2 Background Theory

3.2.1 Method of Creating a Cold Magnetically Trapped Cloud

Atoms held within a MOT are likely to be cooled to approximately the Doppler cooling limit, cooling the atoms further can be achieved using Sisyphus cooling in a molasses. The lowest possible temperature is the Sisyphus cooling limit for a atom of mass M is given by:

$$T_{SisLim} = \frac{h^2}{k_B M \lambda^2} \tag{3.1}$$

Where λ is the wavelength of the cooling light. This limit is inversely proportional to mass and the experiment uses one of the heavier alkali metals (rubidium) for which this limit is 0.4 μK. However background magnetic fields which are hard to eliminate completely will cause the magnetic sub-levels to be perturbed and the achieved temperature is normally a few μK.
Cooling any further is not possible using optical techniques based on the photon recoil force as the energy removal tool, evaporative cooling of the atoms is required to cool the cloud further. Evaporative cooling can be done in either an optical dipole trap or magnetic trap. Here we will focus on the magnetic trap.
Loading atoms into a magnetic trap from room temperature is almost impossible because the magnetic trap depth is typically very shallow compared to the kinetic energy of atoms loaded into the MOT. Capture velocities for rubidium in a MOT and magnetic trap over a few milli metre stopping length are of the order 10^1 m/s and 10^{-2} m/s respectively. Hence a MOT is used to pre-cool the atoms first. A magnetic trap can be created using a quadrupole field which is zero in the centre and increases linearly moving outwards. Atoms in the low field seeking state feel a force $F = g_F \mu_B m_F \nabla.B$ towards the trap centre. For our rubidium MOT if we assume even distribution over all F and $m_F = -F$ to $m_F = +F$ levels there will

be less than half of the atoms in a low field seeking state. This can be improved by briefly applying a circularly polarised beam to pump the atoms to a magnetically trapped state in between the molasses going off and the magnetic trap coming on. To achieve a BEC in a magnetic trap evaporative cooling is used to allow the hotter atoms to escape and carry away thermal energy, the colder atoms remain and re-thermalise at a lower temperature. Normally when evaporating in order to achieve a BEC the number of atoms in the trap reduces by several orders of magnitude however the phase space density can be increased rapidly enough for the onset of quantum degeneracy.

3.2.2 Magnetic Traps -Principle of Operation

Zeeman Effect

The magnetic trapping force is the result of the Zeeman effect in an inhomogeneous magnetic field. Hyperfine structure is a consequence of a perturbation to fine structure levels which occur due to coupling of angular momentum to the nuclear spin $\mathbf{I}$. The hyperfine interaction is described by $A\mathbf{I}.\mathbf{J}$ and gives total angular momentum $\mathbf{F} = \mathbf{I} + \mathbf{J}$, where A is the interaction strength which gives the energy splitting between levels and $\mathbf{J} = \mathbf{L} + \mathbf{S}$ is the total angular momentum resulting from the coupling of spin $\mathbf{S}$, and angular momentum $\mathbf{L}$. The quantisation of the angular momentum allows there to be $2F + 1$ magnetic sub-levels per hyperfine level which are degenerate in the absence of a magnetic field. The following Hamiltonian can be used to describe what happens to the magnetic sub-levels when a field is applied:

$$H_{ZE} = \frac{\mu_B}{\hbar}(g_S\mathbf{S} + g_L\mathbf{L} + g_I\mathbf{I}).\mathbf{B} \tag{3.2}$$

Where g_S, g_L and g_I are Landé g-factors. Considering a uniform field along a quantisation axis z we can write the Hamiltonian as:

$$\begin{aligned} H_{ZE} &= \frac{\mu_B}{\hbar}(g_S S_z + g_L L_z + g_I I_z)B_z \\ &\simeq \frac{\mu_B}{\hbar}(g_S S_z + g_L L_z)B_z \end{aligned} \tag{3.3}$$

The simplification of H_{ZE} occurs since $g_I \ll g_S, g_L$ First we consider the effect of small magnetic fields where the Zeeman energy shift is smaller than the hyperfine splitting ($\mu_B B_z < A$). Hence F and m_F are good quantum numbers and we use the

$|IJFm_F\rangle$ form of the atomic energy state. F precesses around the quantisation axis (B field). We can approximate the Zeeman effect as a perturbation to the hyperfine energy levels and the Hamiltonian can be written:

$$H_{ZE} = g_F \mu_B F B \tag{3.4}$$

And so the resulting shift in the magnetic sub-levels are linearly related to the field strength.

$$\Delta E = g_F m_F \mu_B B \tag{3.5}$$

Here we have used the simplification $g_S = 2.0023193043737 \simeq 2$ and $g_L = 0.99999369 \simeq 1$ which simplifies the bracket in equation (3.3) to $(2S_Z + L_Z) = F g_F$ where

$$\begin{aligned} g_F &= \frac{F(F+1) + J(J+1) - I(I+1)}{2F(F+1)} g_J \\ g_J &= \frac{3}{2} + \frac{S(S+1) - L(L+1)}{2J(J+1)} \end{aligned} \tag{3.6}$$

For high fields where the Zeeman shift is of the order of the hyperfine splitting ($\mu_B B_z > A$) and so F and m_F are not good quantum numbers. We therefore use the quantum numbers J, m_I and m_J and consider the Zeeman effect as a perturbation to the fine structure splitting using the atomic energy state of the form $|IJm_I m_J\rangle$. Now **J** precesses around the magnetic field and the Hamiltonian in equation (3.3) becomes:

$$\begin{aligned} H_{ZE} &= \frac{\mu_B}{\hbar}(g_S S_z + g_L L_z + g_I I_z) B_z + H_{HFS} \\ &\simeq \frac{\mu_B}{\hbar}(g_J J_z) B_z + A\mathbf{I}.\mathbf{J} \end{aligned} \tag{3.7}$$

The energy shift is given by

$$\begin{aligned} \Delta E &= g_J \mu_B m_J B - g_I \mu_B m_I B \\ &\simeq g_J \mu_B m_J B \end{aligned} \tag{3.8}$$

For the rubidium D2 line the boundary between the low field and high field scenarios is of the order of tens of milli Tesla, the size of the magnetic trap used in this work is of the order of a few millimetres with a field gradient of $\sim$ 10 mT/cm, meaning that most atoms exist in the low field region.

The ground states energy splitting of the rubidium D2 line ($J = 1/2$) are described exactly by the Breit Rabi formula [143].

$$\begin{aligned} \Delta E &= -\frac{A(I+1/2)}{4I+2} + g_I \mu_B m B \pm \frac{A(I+1/2)}{2}(1 + \frac{4mx}{2I+1} + x^2)^{1/2} \\ x &= \frac{(g_J - g_I \mu_B B)}{A(I+1/2)} \end{aligned} \tag{3.9}$$

where $m = m_I \pm m_J$ and follows the same sign as in equation (3.9).

Magnetic Force on Neutral Atoms

From equation 3.5 an atom in a weak magnetic field which is not uniform and varies spatially with a field gradient given by $\nabla.B$ will feel a force:

$$F_{Btrap} = -g_F \mu_B m_F \nabla.B \tag{3.10}$$

Note that the direction of the force is dependent on the sign of $g_F m_F$. High field seeking (HFS) atoms $g_F m_F < 0$ feel a force in the direction of the positive field gradient, low field seeking (LFS) atoms $g_F m_F > 0$ feel a force towards the negative field gradient. HFS atoms are more difficult to trap because a local magnetic maximum is forbidden by Maxwell's law ($\nabla.B = 0$), hence we use a trap geometry which creates a local field minimum.

The Quadrupole Field

A quadrupole field uses two identical coils separated along a common z-axis . Current in the two coils is in opposing directions and the resulting field is shown in figure 3.1. Due to symmetry the field in the x (B_x) and y (B_y) are equivalent and again from Maxwell's equations the field gradient in the z-direction $\frac{\partial B_z}{\partial z}$ near to the origin is given by:

$$\frac{\partial B_z}{\partial z} = -2\frac{\partial B_x}{\partial x} = -2\frac{\partial B_y}{\partial y} \tag{3.11}$$

For this geometry the trapping potential extends all the way out to the coils as long as the high field region does not put the atom in an untrapped state. For example equation (3.9) becomes negative (and hence HFS) for the $F = 1$, $m_F = -1$ of the ^{87}Rb D2 line for fields in excess of 250 mT. However in principle we normally want to contain the atoms in a cloud with dimensions of the order of 1 mm which for

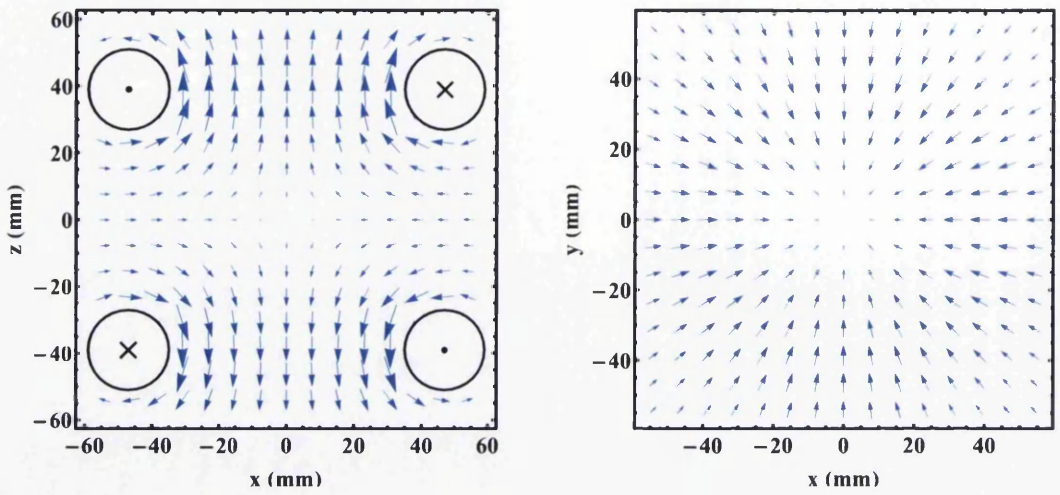

Figure 3.1: Field from a quadrupole field in the x-z and x-y plane for circular coils displaced along the z - axis

rubidium means that a field gradient of approximately 10 mT/cm is required for a trap depth of 1 mK.

Majorana Spin Flips

Majorana transitions can occur at the centre of the quadrupole field where the magnetic sub-levels become degenerate, this can lead to 'spin flips' to untrapped states and hence losses from the trap. These losses become worse for colder denser clouds which accumulate nearer the centre of the trap. Consider an atom moving at some point r away from the centre of the trap at some velocity v. Close to the centre of the trap the direction of the magnetic field will change rapidly in the atomic reference frame, if the precession of the atom's dipole moment around the magnetic field is unable to keep up with this rotation, quantified by the Larmor frequency, then the atom can spin flip to an untrapped magnetic sub-level. The Larmor frequency for an atom in a uniform field B is:

$$\omega_{Lar} = \frac{g_F m_F \mu_B B}{\hbar} \tag{3.12}$$

In the quadrupole field $B = \frac{dB}{dr} r$,where r is the radial position of the atom, the

Larmor frequency can be written:

$$\omega_{Lar} = \frac{g_F m_F \mu_B r}{\hbar} \frac{dB}{dr} \tag{3.13}$$

Coil geometries to prevent Majorana spin flips are discussed in section 3.3.4. The schemes considered work by making the field minimum non-zero at the centre and harmonic in shape.

In a harmonic trap the trap strength is expressed by considering simple harmonic motion of an atom in the parabolic potential and using the frequency of its oscillation known as the trap frequency $\omega_{trap} = (\omega_x, \omega_y, \omega_z)$. Considering one (x) axis the field along the x-axis close to the trap centre $(x = 0)$ is given by:

$$B(x) = B_0 + \frac{B_2}{2} x^2 \tag{3.14}$$

where $B(0) = B_0$ and B_2 is the curvature. The potential U of an atom in the harmonic potential can be approximated using Hooke's law for a particle on a spring with spring constant k:

$$\begin{aligned} U(x) = \frac{k}{2} x^2 &= \mu_B g_F m_F (B(x) - B_0) \\ &= \mu_B g_F m_F (B_2 x^2) \end{aligned} \tag{3.15}$$

and hence $k = \mu_B g_F m_F B_2$. From Hooke's law the oscillation frequency for a particle of mass m is given by:

$$\omega_{Hooke} = \omega_x = 2\pi\nu_x = \sqrt{\frac{k}{m}} \tag{3.16}$$

Re-arranging this equation the trap frequency is given by

$$\omega_x = \sqrt{\frac{\mu_B g_F m_F B_2}{m}} \tag{3.17}$$

If the harmonic trap is derived from a quadrupole with its centre corresponding to the origin then the curvature of the potential, and hence B_2, reduce for larger B_0 and so B_0 need only be as large as is required to prevent spin flips - typically a field of the order of 0.1 mT is sufficient.

Gravitational Effects

When gravity acts upon the atoms in the trap the magnetic trap forms at the point where $F_{Btrap} = F_{grav}$
From equation (3.10) we can estimate the field gradient along the z-axis from a quadrupole field needed to counter gravity:

$$\frac{dB}{dz} = \frac{mg}{\mu_B m_F g_F} \tag{3.18}$$

Which for a rubidium atom in the $F = 2$, $m_F = 2$ state a field gradient of $\frac{dB}{dz} \simeq 1.52$ mT/cm is required to counter gravity. In a harmonic trap where the field gradient is spatially varying the atom cloud would be displaced to the point where $\frac{dB}{dz} \simeq 1.5$ mT/cm, this is often referred to as 'gravitational sag'.

3.2.3 From MOT to Magnetic Trap

Molasses and Sisyphus cooling

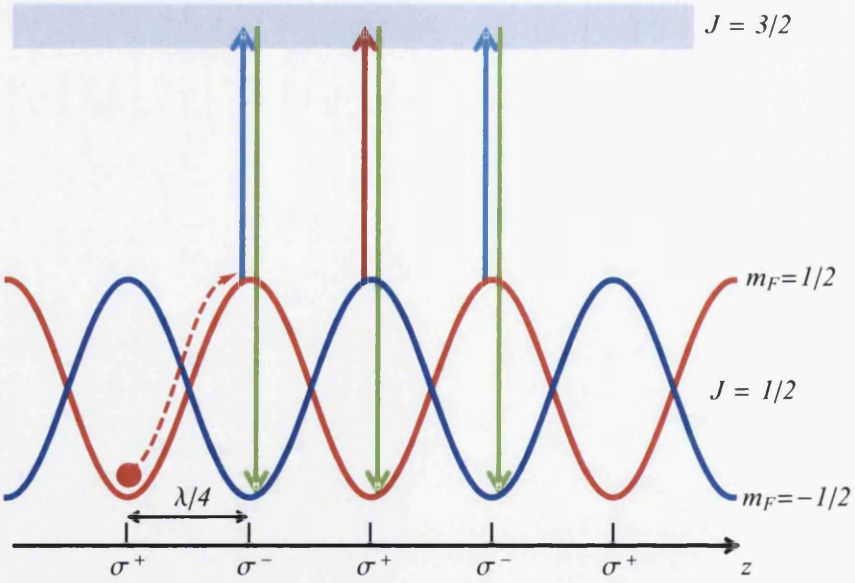

Figure 3.2: Sisyphus cooling mechanism. Blue = σ^-,$-m_F$, red = σ^+,$+m_F$. Shifts in $J = 3/2$ are not shown for clarity.

Sisyphus cooling is a sub-Doppler cooling mechanism which was found to occur within an optical molasses [46, and references 20, 21 therein]. The phenomenon was first explained by J. Dalibard and C. Cohen-Tannoudji [50]. The principle can be understood in one dimension with two counter-propagating laser beams forming a standing wave with spatially varying polarisation. The light shift causes a periodic shift of the two ground state magnetic sub-levels as shown in figure 3.2. As an atom (for example in $J = 1/2$, $m_J = 1/2$) moves along the standing wave it will lose kinetic energy as it 'rolls up a hill'. At the top of the hill the energy level at this location has shifted towards resonance with a red detuned beam which is σ^- polarised, exciting the atom to $J = 3/2, m_J = -1/2$. When this atom subsequently decays to $J = 1/2, m_F = -1/2$ it will have lost more energy than it absorbed because it now ends up in a light shift 'valley'. Atoms can also decay back to $J = 1/2$, $m_J = 1/2$ with no energy loss but this is less likely to occur.

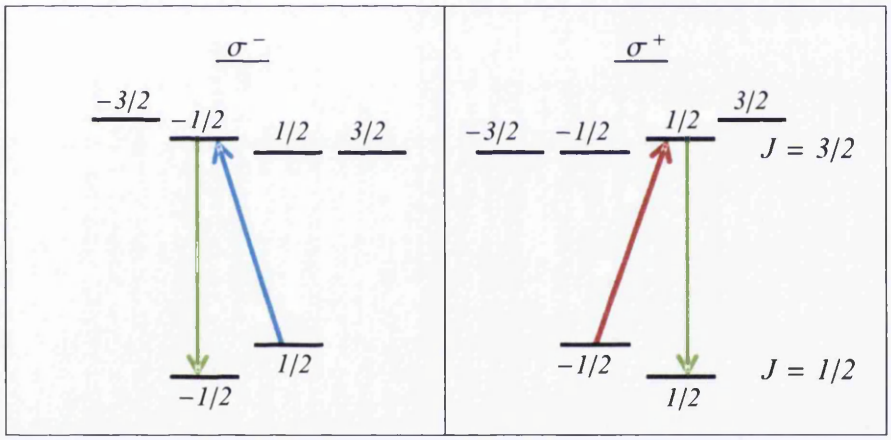

Figure 3.3: Schematic of the energy level structure for Sisyphus cooling. On the left is the shift in regions of σ^- and the right is the shift in regions of σ^+. Magnetic sub-levels are labelled with their respective m_J value.

For rubidium the diagram would be much more complex involving more m_F levels shifted by an amount proportional to m_F^2 but the principle would remain the same. Sisyphus cooling is not efficient in a MOT due to the quadrupole field which shifts the magnetic sub-levels, so in quantum degenerate gas experiments it is common to briefly provide further cooling to a MOT by creating an optical molasses for a few milliseconds in between the MOT going off and the magnetic trap switching on. The temperature T achieved by this cooling mechanism is related to light intensity I and detuning δ and is given by $T \propto \frac{I}{k_B|\delta|}$ [42]. Sisyphus cooling is effective as long

as the semi-classical model of the atom holds true. The limit of Sisyphus cooling T_r is of the order $T_r \sim \hbar^2/2k_B m\lambda^2$ [144].

Optical Pumping

Transfer of atoms from a MOT or molasses can be optimised by ensuring that as many atoms as possible are in a magnetically trapped state (LFS). It is therefore necessary to optically pump the atoms into a LFS state. In ^{87}Rb optical pumping can easily be achieved using a circular polarised beam - as shown in figure 3.4.

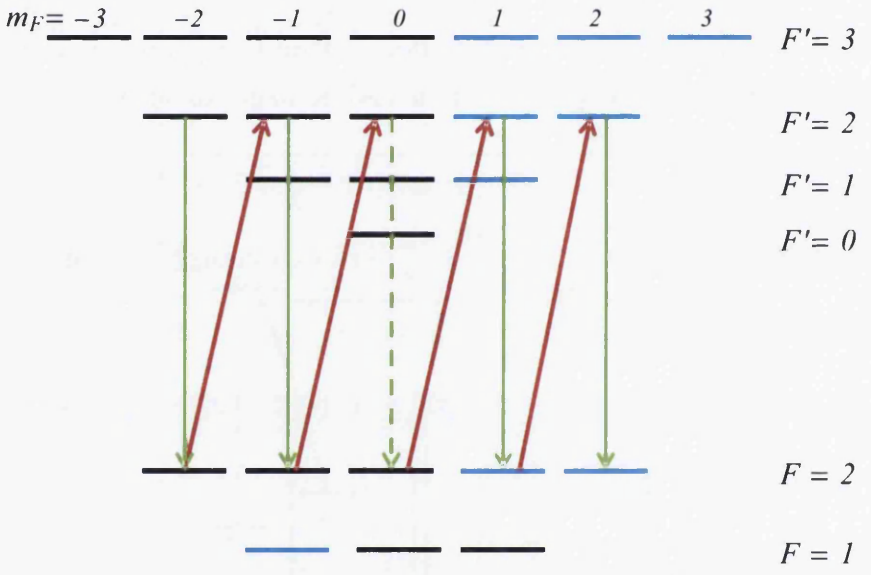

Figure 3.4: A possible optical pumping system for ^{87}Rb. LFS states (magneticlly trapped in a quadrupole minimum) are shown in blue. Not shown is the re-pump laser, $F = 1 \rightarrow F' = 2$ transitions, and σ^+ and σ^- decay transitions. The dashed arrow from $F' = 2, m_F = 0 \rightarrow F = 2, m_F = 0$ indicates the net effect of σ^+ and σ^- decays since $F' = 2, m_F = 0 \rightarrow F = 2, m_F = 0$ is not an allowed transition.

The transition used is $F = 2 \rightarrow F' = 2, \Delta m_F = +1$, which pumps the atoms towards $F' = 2, m_F = 2$ which decays to $F = 2, m_F = 2$. Once in this LFS state the atoms can no longer interact with the pump beam which avoids further heating of the atoms which will occur since the pumping process also creates heating from the photon recoil force and typically there is no heat removal process at this stage. Heating can be minimised by retro-reflecting the pumping beam, however, this is not

practical in the setup described in this thesis since it is planned to use the imaging axis for optical pumping. Atoms can decay to to $F = 1$, and so the $F = 1 \rightarrow F' = 2$ re-pump beam must be on for optical pumping.
Another possible optical pumping scheme in ^{87}Rb is pumping to $F = 1, m_F = -1$ using $F = 1 \rightarrow F' = 1, \Delta m_F = -1$ (σ^- beam) with a $F = 2 \rightarrow F' = 1$ re-pump, [145] however atoms in the $F = 1, m_F = -1$ are less strongly magnetically trapped than the other states.

3.2.4 Route to BEC and Degenerate Fermi Gas

Although further cooling and creation of a BEC or degenerate Fermi gas were not achieved within this thesis, this is the eventual goal of the experiment and the equipment has been designed with this in mind, hence the theory of a BEC and cold Fermi gas is briefly presented here.

Evaporative cooling

Further cooling of atoms in a magnetic trap occurs by evaporation of the hottest atoms, which have a temperature higher than the average temperature and hence enough energy to escape the trap. The sides of the potential are gently lowered at a rate which only allows the hottest atoms to escape and so minimises loss from the trap. In a magnetic trap the trap sides cannot be lowered by simply reducing the coil current because this would also reduce the trap frequency resulting in a reduced cloud density, instead an RF field is used to 'spin flip' atoms which drift too far from the trap centre, i.e. to a region of strong magnetic field. A radio frequency (RF) magnetic field ω_{RF} applied to the trap can drive spin flips between m_F levels if an atom has energy E given by:

$$E = \omega_{RF}\hbar|m_F| \tag{3.19}$$

where

$$\omega_{RF} = |g_F|\mu_B\frac{B}{\hbar} \tag{3.20}$$

Hence by tuning the RF frequency atoms can be liberated from the trap if they are located at a specific point in the magnetic field, this is known as the evaporation surface. Atoms can be selectively removed if they are located at highest B, i.e those with highest energy and by slowly ramping down the RF frequency there will be

continual removal of the hottest atoms as the cloud cools. The optimal rate of RF reduction must be determined experimentally, it must be fast enough to minimise loss from the trap due to collisions with background gases but slow enough that the re-thermalisation rate can keep up. Elastic collisions within a magnetic trap are crucial for the re-distribution of energy which keeps the cloud in a normal thermal distribution. Hence the collision rate is directly related to the rate at which efficient evaporative cooling can proceed. Cold collisions are discussed in more detail in section 3.2.5. It is also important to take into account gravitational sag which causes the coldest atoms to not be at the field minimum.

Runaway Evaporation

As the cloud gets colder the remaining atoms move closer to the centre of the trap, where the potential is lowest, this causes the density to increase along with the re-thermalisation rate, hence the evaporation rate increases causing the density to increase further and so on. This process is called runaway evaporation and must be maintained in order to achieve quantum degeneracy.

What is a BEC and Fermi Degeneracy?

In low energy regimes the atomic energies are quantised. Bosons are integer spin particles and hence by the Pauli principle are allowed to exist in the same quantum state as another Boson. The Bose distribution function f_{BE} describing the number of atoms n_i occupying each state i is:

$$n_i = \frac{1}{e^{(E_i-\mu)/(k_bT)} - 1} \tag{3.21}$$

Where μ is the chemical potential.
As evaporative cooling approaches the critical temperature T_c the independent wave-function of individual atoms will begin to interfere with adjacent Bosons, when one falls into the ground state stimulated emission will cause an avalanche effect into the ground state.
From equation 3.21 it is possible to derive the critical temperature for N atoms in a box potential as [42]:

$$T_c \simeq \left(\frac{N}{2.6}\right)^{2/3} \frac{2\pi\hbar^2}{mk_b} \tag{3.22}$$

In a harmonic potential the critical temperature is given by [144]:

$$T_c \simeq 0.94\hbar\bar{\omega}N^{1/3} \tag{3.23}$$

where $\bar{\omega} = (\omega_x\omega_y\omega_z)^{1/3}$

This critical point is often described using the phase space density (PSD) and De Broglie wavelength $\lambda_{dB} = \frac{h}{\sqrt{2\pi m k_b T}}$.

$$PSD = \frac{n}{V} = n\lambda_{dB}^3 \tag{3.24}$$

Where $n = N/V$ is the number density. A phase transition to a BEC will occur when $PSD \simeq 1$, at which point the De Broglie wavelength becomes greater than the mean separation between atoms in the cloud.

The behaviour of atoms in a BEC can be described by taking into acount the additional energy resulting from the interaction between the atoms. The resulting equation for the condensate wavefunction ψ is called the Gross Pitaevskii equation [146, 147].

$$\mu\psi(\mathbf{r}) = \left(-\frac{\hbar^2}{2m}\frac{\partial^2}{\partial\mathbf{r}^2} + V(\mathbf{r}) + g|\psi(\mathbf{r})|^2\right)\psi(\mathbf{r}) \tag{3.25}$$

The interaction strength between adjacent atoms is given by g:

$$g = \frac{4\pi\hbar^2 Na}{m} \tag{3.26}$$

Note that a is the scattering length which can in some atomic species be tuned using Feshbach resonance.

Fermions have half integer spin for which we must use Fermi-Dirac statistics. For a Fermi gas the number of atoms n_i distributed in an energy level i is given by:

$$n_i = \frac{1}{e^{(E_i-\mu)/(k_bT)} + 1} \tag{3.27}$$

Note that this distribution has a maximum value of 1 for any given energy level.

The chemical potential μ is also a function of temperature, the value of μ at $T \to 0$ is often called the Fermi energy E_F which is related to the Fermi temperature T_F,

$E_F = k_B T_F$. For a particle in a box potential the Fermi temperature is given by:

$$E_F = \frac{\hbar^2}{2m}\left(\frac{6\pi^2 n}{V}\right)^{2/3} \tag{3.28}$$

And for a Fermi gas in a harmonic well the Fermi energy reduces to:

$$E_F = (6n)^{1/3}\hbar\bar{\omega} \tag{3.29}$$

In comparison to a gas of bosons a gas of fermions does not condense into the ground state of the trap and runaway evaporation does not occur due to the Pauli priniple. At cold temperatures one atom exists in each state up to E_F which is called Fermi degeneracy. Achievement of Fermi degeneracy usually requires a buffer gas because collisions between identical spin polarised fermions are forbidden at low temperatures. Our system has been designed with the future aim of creating cold rubidium - potassium Bose-Fermi mixtures.

3.2.5 Collision of Cold Atoms

Scattering Length

Since a low energy cloud of atoms is being considered it can be assumed the collisions are predominantly s-wave ($l = 0$). The non-resonant scattering length for elastic collisions (in the absence of Feshbach resonance) a_{nr} can be expressed from the scattering cross section σ_{el}. The scattering cross section is given by [148]:

$$\sigma_{el}(k_{rel}) = \frac{8\pi a_{nr}^2}{1 + k_{rel}^2 a_{nr}^2} \tag{3.30}$$

For two identical counter-propagating atoms with de Broglie wavelength λ_{dB} and wavevector $k = \frac{2\pi}{\lambda}$ the relative wavevector k_{rel} is given by:

$$k_{rel} = \frac{8\pi}{\lambda_{dB}} = \sqrt{\frac{16 m k_B T}{h^2 \pi}} \tag{3.31}$$

As $T \to 0$ the de Broglie wavelength increases and hence $k_{rel} \to 0$, and so for low temperatures equation (3.30) can be simplified to

$$\sigma_{el} = 8\pi a_{nr}^2 \tag{3.32}$$

The elastic collision rate γ_{el} between a cloud of N atoms per unit volume is:

$$\gamma_{el} = N\sigma_{el}\langle v_{rel}\rangle \tag{3.33}$$

where $\langle v_{rel}\rangle$ is the mean relative velocity of the atoms in the cloud. By considering the relative energy of two identical particles in the centre of mass reference frame, equating thermal and kinetic energy gives:

$$\langle v_{rel}\rangle = \sqrt{\frac{16k_BT}{\pi m}} \tag{3.34}$$

The collision rate is related to the number density and so in evaporative cooling schemes it is common to compress the trap. This compression can be done adiabatically if the trap frequency and collision rate are able to maintain a magnetic trap with the coldest atoms at the lowest field during compression.

Feshbach Resonance

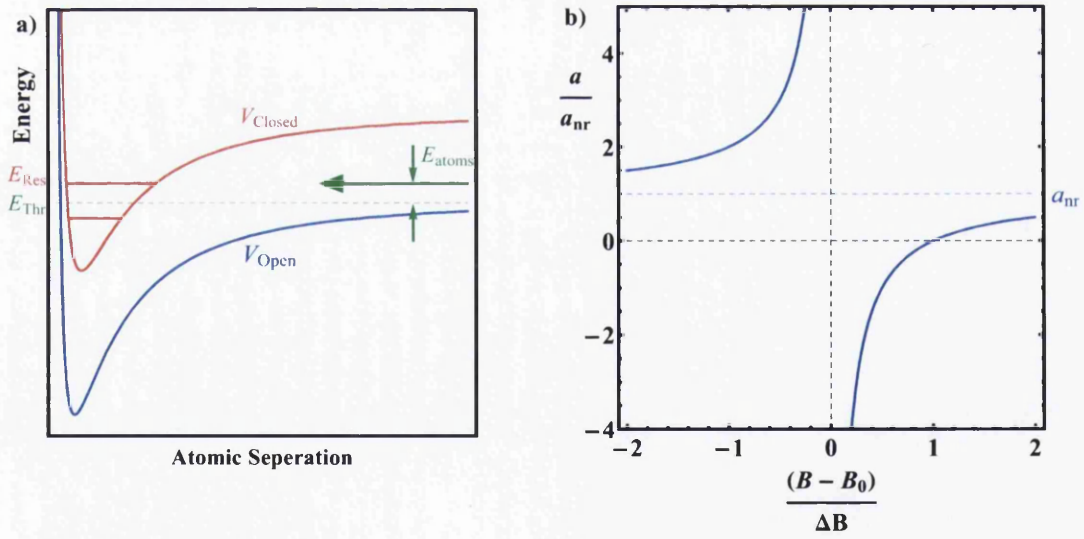

Figure 3.5: (a). Example of Feshbach resonance formation between two energy potentials for an open (blue) and closed (red) channel of two colliding atoms. (b) Plot of the scattering length near to a magnetically induced Feshbach resonance. The scattering length far from resonance is a_{nr}.

Figure 3.5 (a) shows the collision potential for two free atoms in an open channel

(blue line) and the potential for a weakly bound molecular state in a closed channel (red line). In this context a channel is described as closed if there is insufficient energy for atoms colliding in this channel to be at rest far from one another. Energy levels in the closed channel can be tuned by the application of a magnetic field, when the energy of one of theses levels (E_{Res}) is tuned close to the energy of the colliding atoms (E_{atoms}) the two atoms can form a bound state with energy E_{Res}. There is now a strong coupling between the two channels, a consequence of this is that there is a repulsive force between the two atoms if $E < E_{res}$ and an attractive force if $E > E_{res}$. And so the scattering rate is given by [144]:

$$a = a_{nr}\left(1 - \frac{\Delta B}{B - B_0}\right) \tag{3.35}$$

where a_{nr} is the non-resonant scattering length, B_0 is the field corresponding to a Feshbach resonance and ΔB is the resonance width. The scattering length is plotted in figure 3.5 (b). Hence Feshbach resonances can be used to tune the scattering length which enables the atom-atom interaction to be tuned and can be used to aid evaporative cooling, this is particularly useful for species which are difficult to evaporatively cool otherwise [149]. Feshbach resonances can also be used to form weakly bound molecules.

The coils which were designed to produce the magnetic trap for this experiment have also been designed to switch to Helmholtz coils able to probe Feshbach resonances in ^{40}K at 20.2 mT [150] for future experiments. They could also be used for the ^{87}Rb resonance at 68.5 mT [151].

3.3 Expansion of the Setup

The setup used for the P1 oscillation experiment was adapted for the creation of a magnetic trap.

3.3.1 Additions to the Laser System

Three lasers are again utilised for this experiment. These were the same lasers used for the P1 experiment but with different roles. The cooling laser, (previously the master laser,) was used as the workhorse of this experiment. It provided the MOT trapping beam, and will also eventually provide the molasses beam, the optical

pumping beam and the imaging beam. The cooling laser will need to be able to jump to various $F = 2 \rightarrow F'$ transitions, hence the polarisation spectroscopy lock was converted to a DAVLL lock (see section 3.3.2).

An AOM and two shutters were also added, the modified setup is shown in figure 3.6. The AOM will be used to control the imaging beam which will also provide optical pumping.

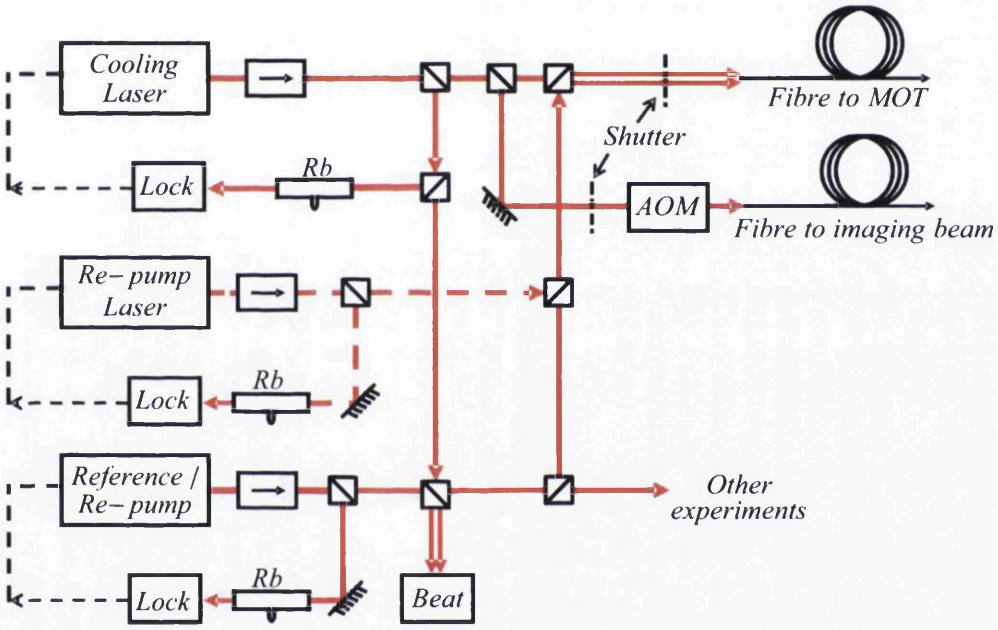

Figure 3.6: Laser setup for the magnetic trap experiment. Dashed laser beams indicate the proposed re-pump laser beam setup which was not used due to a diode failure.

The reference laser used a polarisation spectroscopy lock and continued to be used as a reference for the cooling laser, because a DAVLL spectrometer cannot resolve hyperfine structure. The laser previously used as a slave laser was setup with a polarisation spectrometer for use as a re-pump laser however due to catastrophic failure of the diode it was not used for the MOT and magnetic trap data presented here. The reference laser was temporarily used to provide re-pumping light.

3.3.2 DAVLL Lock

A dichroic atomic vapour laser lock, or DAVLL, creates an error signal which is one long slope which can span many hundreds of MHz and several hyperfine transitions [152, 153]. By applying an offset to this error signal the lock circuit can be made to rapidly jump the frequency of the laser to different points along the slope. The DAVLL setup is shown in figure 3.7.

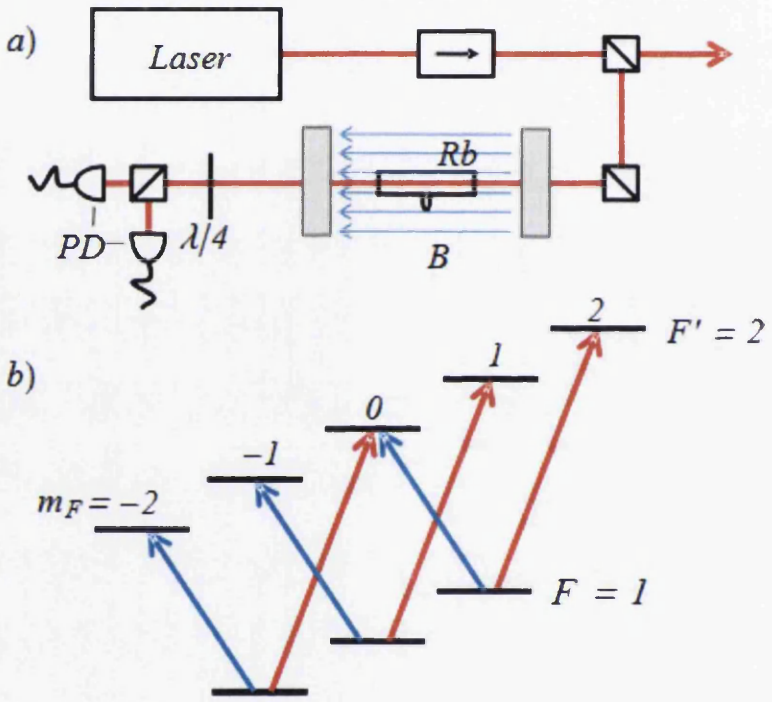

Figure 3.7: (a) DAVLL setup, two ring-shaped permanent magnets provide the magnetic field in the cell. (b) Example shifts in the magnetic sub-levels for the $F = 1$ and $F' = 2$ levels. Red arrows correspond to σ^+ transitions and blue arrows to σ^- transitions.

A single beam passes through a rubidium vapour cell and a linear magnetic field along the beam axis makes the rubidium atoms in the vapour cell become dichroic. This means the magnetic sub-levels Zeeman shift in frequency by an amount which is related to $m_F B$ and hence σ^+ and σ^- polarisations, which drive $\Delta m_F = +1$ and -1 respectively, observe the whole Doppler broadened linewidth to shift in opposite directions in frequency. Using a quarter wave plate, a beam splitter cube and two photo detectors it is possible to take the difference between the intensity in the two polarisations and produce an error signal for a lock circuit. The error signal gives

one slope which spans over the whole line. The slope is caused by two Doppler profiles where one is inverted, see figure 3.8. The optimum magnetic field strength to maximise gradient and signal amplitude has been investigated [153] and occurs at 12.5 mT. The separation of the permanent magnets was limited by the length of the rubidium cell and mount. A separation of 85.5 mm was used giving a field of 11.4 mT

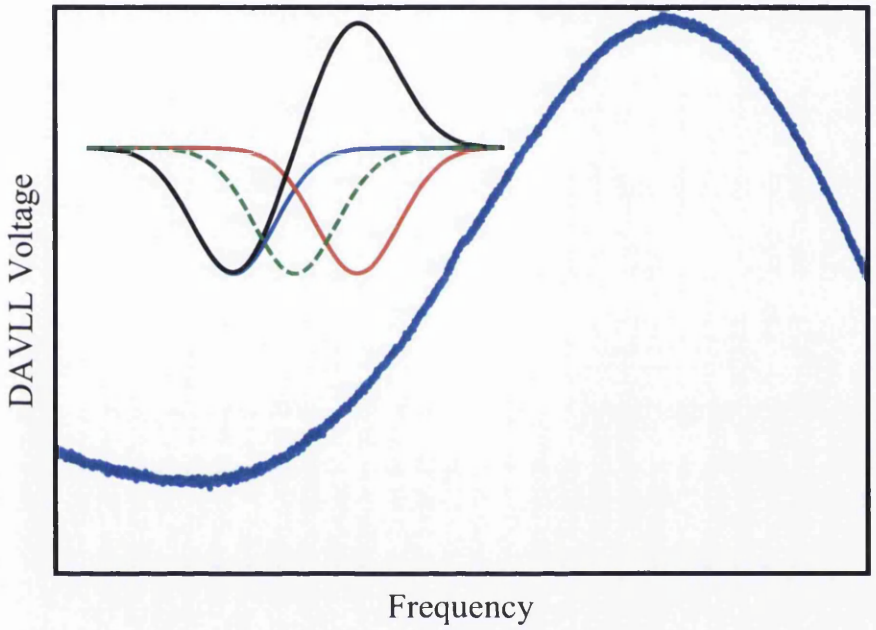

Figure 3.8: DAVLL output. The DAVLL output signal for the ^{87}Rb $F = 2 \rightarrow F'$ Doppler profile. The assymetry in the signal is due to the proximity of the ^{85}Rb $F = 3 \rightarrow F'$ transition which is just off view to higher frequency. In the inset the magnetic field in the rubidium cell is demonstrated to cause a frequency shift to negative frequency for σ^- light (blue) and to positive frequency for σ^+ light (red) relative to the non-shifted Doppler profile (green dashed). Taking the difference between the red and blue line gives the DAVLL signal (black line) which has a continuous slope over nearly all the original un-shifted Doppler profile.

The temperature stability of the DAVLL lock mechanism was studied in detail, see appendix A.4.

3.3.3 The Vacuum System

Magnetic traps for neutral atoms must be created inside a vacuum chamber, this presents several challenges for our experiment due to the need to produce large

fields and optimise optical access for several laser beams. Two obvious solutions to this are to conduct the experiment inside a glass cell or use coils or optics which go inside the vacuum chamber such as an optical pyramid [134], miniature baseball coil [154] or traps on a microchip [66]. Placing components inside the chamber can make maintenance and adjustments more awkward, reduce lines of sight and limit the geometry of other experiments which can be placed nearby to use the cold atoms. Standard stainless steel vacuum chambers are also magnetic. A small glass cell allows almost unlimited optical access and is well suited to the use of external coils, however a cell severely limits the mounting and size of further experiments. Due to some of the future plans for this experiment (see section 4.1) we would like to have an experiment and chamber which has: enough optical ports to create a MOT, no equipment required in the chamber for creation of a magnetic trap, mounting options for future experiments to use the cold atoms and large or spare ports which can be used for adapted flanges with bespoke equipment attached. Since this necessitates a metal chamber we will aim to minimise the magnetic field contribution from chamber walls and all coils and optics will be external giving easy maintenance and adjustment.

The vacuum chamber was the same Kimball Physics MCF450 spherical octagon that was used for the P1 experiment. It has two large CF63 ports and eight CF16 ports and grabber groove technology for mounting equipment inside the chamber, but is only 35.1 mm deep. This narrow chamber enables coils to be mounted in the axis of the chamber with minimal separation giving a large field.

Several improvements were made to the setup used in the P1 experiment to ensure the vacuum is suitable for magnetic trapping. For a magnetic trap to have a lifetime of several seconds or longer, pressures around 10^{-10} mbar or lower are required [155]. To confirm this an ionisation gauge was added (Varian UHV-24p ionisation gauge) which can measure pressure down to 10^{-12} mbar, along with a non evaporable getter (NEG) pump with a specified pumping speed for hydrogen of 240 l/s (Varian Gp50 with St101 cartridge), the 2 l/s NEG pump used previously was removed. The same 20 l/s ion pump used for the P1 experiment was used for the magnetic trap.

Two non-magnetic anti-reflection coated viewports (MDC ZCVP-16-QBBAR-NM) were added to the chamber for the imaging beam. The top CF63 viewport was also replaced with a non magnetic anti-reflection coated viewport (MDC ZCVP-63-BBAR-LN), the bottom CF63 viewport remained an uncoated CF63 viewport but this is due to be replaced with a bespoke flange in the future (see section 4.1.3).

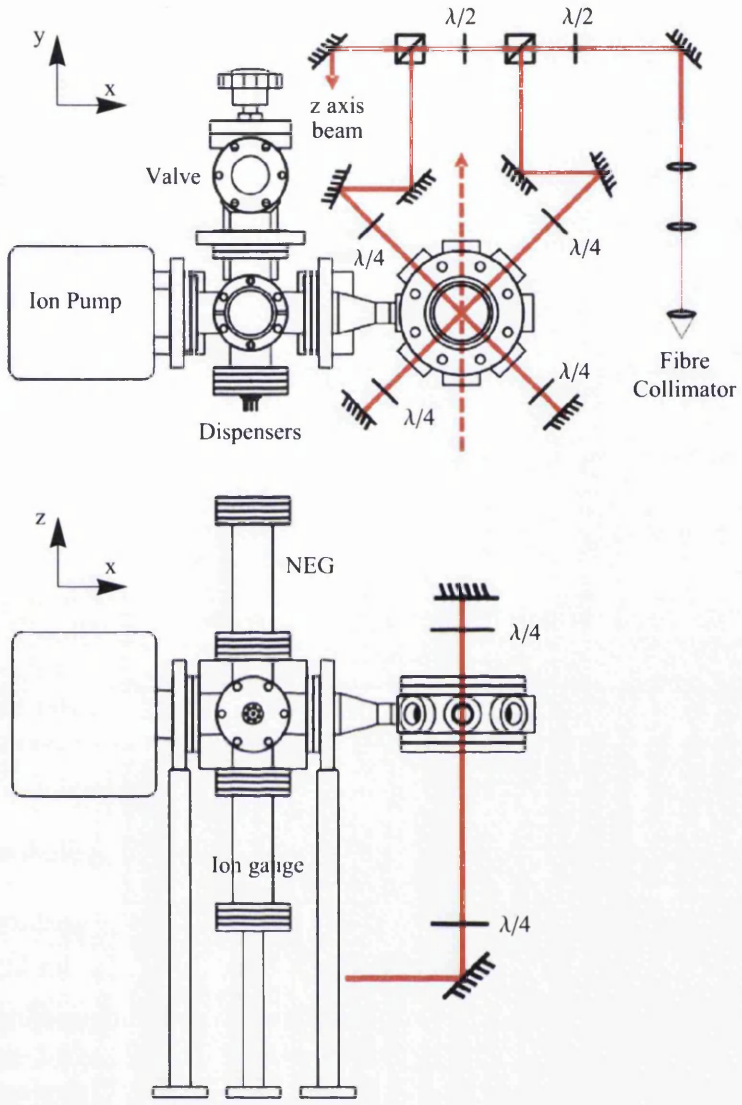

Figure 3.9: Top and side views of the vacuum chamber. The valve allows the connection of bellows to a turbo and rough pump for bakeout but this is normally blanked off, the NEG and ion gauge are each housed within a CF40 nipple. After the fibre collimation package the beam is expanded to 4.5 mm by a telescope and split into six beams of approximately equal power. The dashed line indicates the path of the (future) imaging beam, the imaging beam viewports are anti-reflection coated.

Top and side views of the vacuum system and schematic of the MOT laser setup are shown in figure 3.9. The dispensers were moved out of the chamber and mounted on

the new six-way cross with the NEG, ion pump and gauge. For the cross and conical reducer non-magnetic components were used which were made from 316L and 316LN stainless steel. The spherical octagon is also 316LN. This type of stainless steel is less magnetic than the 304 stainless.
The preparation and bakeout procedures used for the system are described in appendix A.1.1. The base pressure for the system after bakeout was about 10^{-10} mbar.

3.3.4 The Coils

The Quadrupole Coils

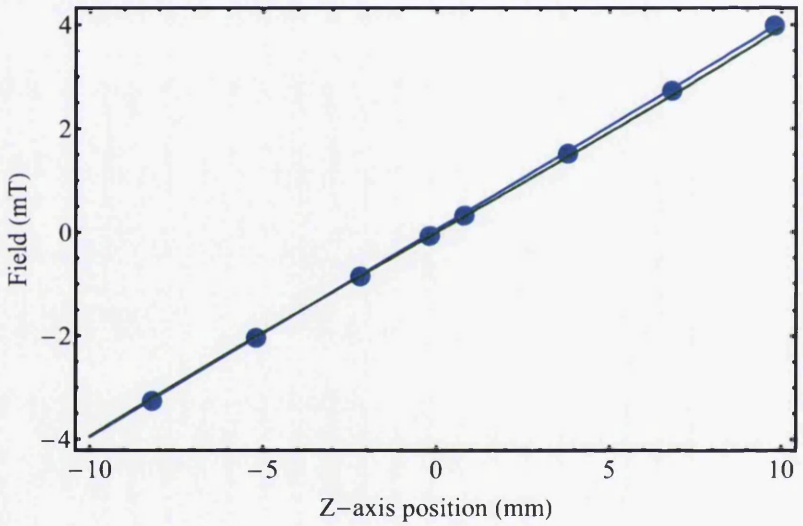

Figure 3.10: Anti-Helmholtz field in Z-direction on the Z-axis. Data (blue points) are fitted with a linear line (blue line) which is compared to the output of the numerical model (green line). The field gradient from the data is 4.00 mT/mm and for the model is 3.90 mT/mm. The discrepency between the two is primarily due to the placement of the Hall probe which was judged by eye to be in the centre of the colis and aligned correctly. The data is also recorded in the lab which has background fields present, for example from the optical table.

The design criteria and construction methods for the quadrupole coils are described in appendix A.2. The coils are high power devices, in their existing configuration they are capable of creating an anti-Helmholtz quadrupolar field with an axial field gradient of 22 mT/cm or a Helmholtz field of 62 mT at the centre of the coils. The same coils were used to create the quadrupolar field for the MOT and magnetic trap. The anti-Helmholtz field and Helmholtz field measured at 80 A is shown in figures

3.10 and 3.11. In figure 3.10 a linear field with a constant field gradient creates a quadrupolar field suitable for a magnetic trap, figure 3.11 demonstrates the creation of a field which is almost homogeneous near to the centre. Coil switching speed with and without the vacuum chamber is studied in appendix A.1.3.

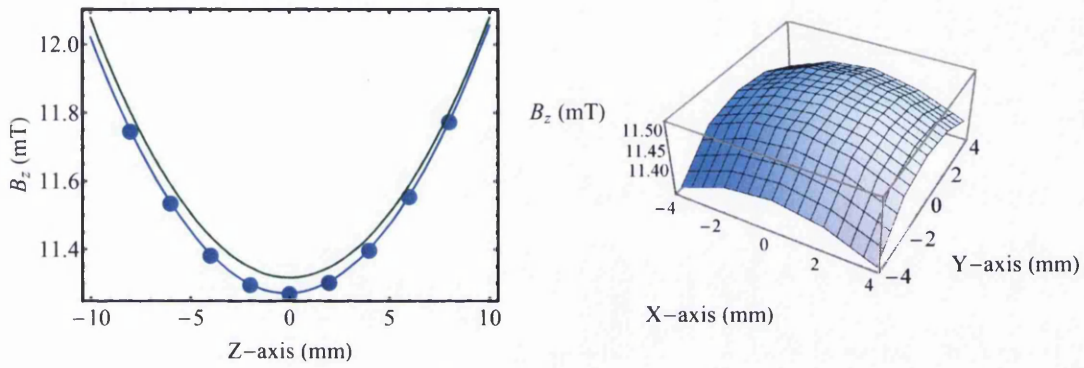

Figure 3.11: Helmholtz field in Z-direction on the Z-axis and field on the X-Y plane at $Z = 0$. Data (blue points) are fitted with a second order polynomial (blue line) which is compared to the output of the numerical model (green line). The model does not perfectly fit the data due to difficulties in estimating the imperfections in the coil winding which arise due to layer changes (see appendix A.2).

Avoiding Majorana Spin Flips

Avoiding these spin flip can be achieved by making the centre of the trap a non-zero local minimum in the magnetic field. Several schemes that produce this effect exist [58, 55, 59, 54] but we will focus on the two which were considered for this experiment. Both schemes are attractive because they are compatible with the quadrupole coils described above. These additional coils were not constructed during this work however it was important to check that these coil geometries were feasible before construction of the vacuum chamber and quadrupole coils. The models presented here are compatible with the experiment constructed to date.

One possible coil geometry is to have one coil (which we refer to as the offset coil) which has its axis of symmetry orthogonal to the central axis of the anit-Helmholtz coils, and is displaced from the centre as shown in figure 3.12. The magnetic field from the offset coil opposes the anti-Helmholtz coils field at the point where the coils are close . As the current in the offset coil is increased the field minimum shifts towards the offset coil, eventually becoming non zero and approximately harmonic at the centre (see figure 3.13). This scheme is easy to realise since it only requires

one additional coil but the disadvantages are the shift of the field minimum away from the centre of the quadrupole and the reduction in field gradient on the side of the trap nearest the offset coil. The offset coil also needs a fairly large current density (around one third of the quadrupole current density for the geometry shown in figure 3.12).

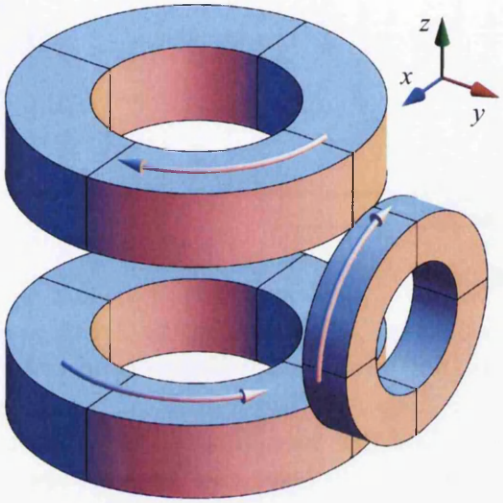

Figure 3.12: Coil setup to create an almost harmonic trap with a single offset coil and two anti-Helmholtz coils. Arrows indicate direction of current.

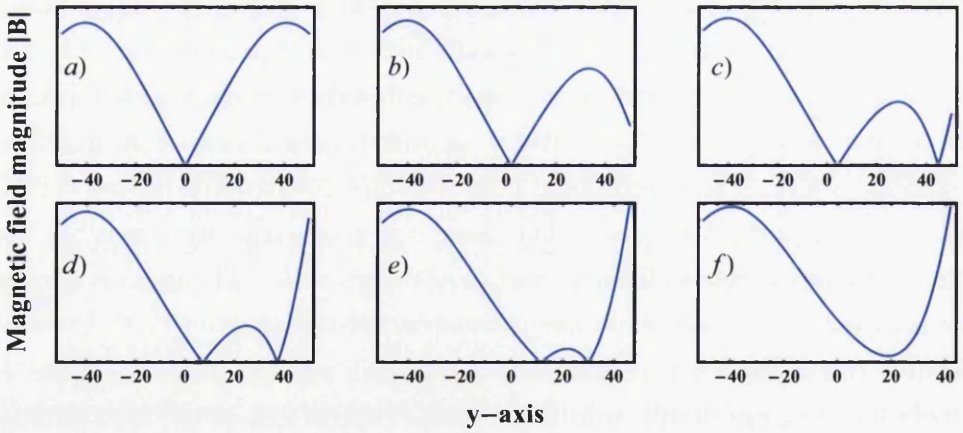

Figure 3.13: (a). No current in the offset coil, (b)-(f) Current in the offset coil is increased until the trap becomes non-zero at the minimum and almost harmonic.

Displacing the centre of the trap and significant change in the trapping field gradient can be avoided by using a Time Orbiting Potential (TOP) trap [58]. Two coil pairs

(four coils) are placed orthogonal to one another and the quadrupole coils as shown in figure 3.14. They are modulated with an alternating current of frequency ω_I with opposite coils out of phase by π and adjacent coils out of phase by $\pm\pi/2$. This rotates the field minimum around the centre of the quadrupole in the xy-plane. The time averaged field is shown in figure 3.15 and as long as the rotation of the zero field is too fast for the atoms to follow they will remain at the time-averaged minimum at the centre of the quadrupole. It is important that $\omega_I < \omega_{Lar}$ to avoid inducing spin flips.

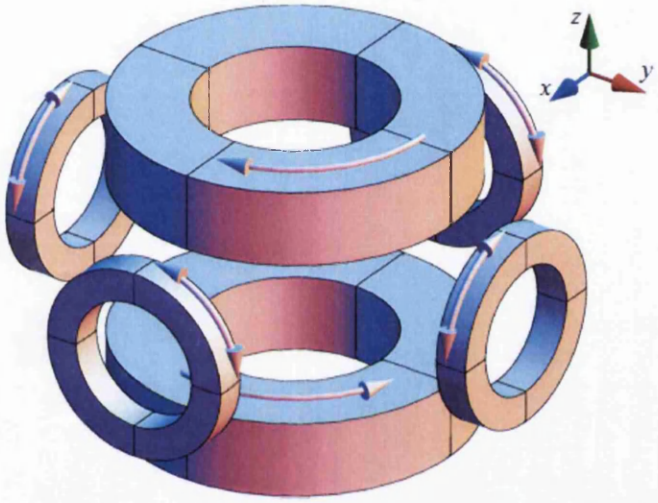

Figure 3.14: Sample coil setup for the TOP trap. The arrows indicate current direction (see figure 3.15(b))

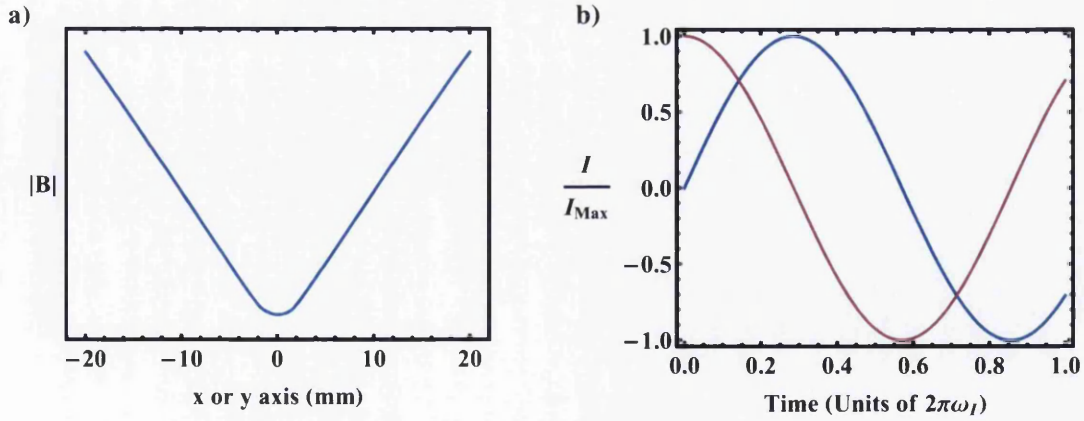

Figure 3.15: (a). The time averaged field along one dimension. (b). The current in the x-axis coils (blue) and y - axis coils (red).

3.3.5 Imaging System

The imaging system is shown in figure 3.17 [1]. The setup is currently configured for fluorescence imaging system but it is being developed for absorption imaging in the near future. The absorption imaging beam is derived from the cooling laser by jumping the DAVLL lock point and can be frequency and amplitude controlled by an AOM, this beam will also used for optical pumping. The beam passes through the centre of the chamber and is imaged on a AVT Marlin G145B CCD camera using an achromatic relay lens (Comar 02-TT-40) with an effective focal length of 80.8 mm. The camera is triggered from a TTL signal generated by a computer control card.

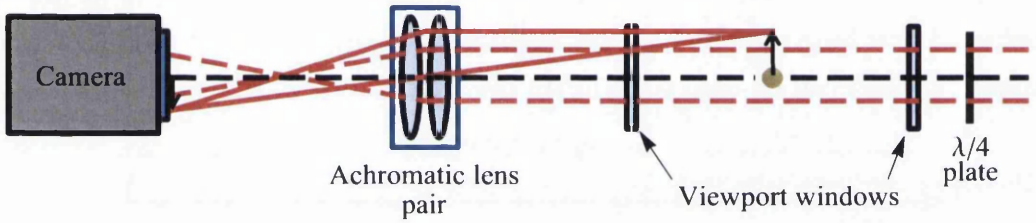

Figure 3.17: Ray diagram for the imaging system setup for fluorescence (red solid) and absorption (red dashed). For clarity the arrow indicates the imaging plane, no magnification is used.

3.3.6 Controlling the Experiment

Control Equipment

The experiment is computer controlled via a National Instruments digital card (NIPXI-6534) and analogue control card (NIPXI-6713 with BNC-2110) housed within PXIe crate (NIPXIe-1062Q and NIPXIe-8375). The analogue card will be used to control the; DAVLL frequency, dispensers, and coils. The digital card will control the AOM, shutters and camera. MOSFET based circuits were built to control the current within the dispensers and coils which are described in appendix A.3.

Control Sequence

For the following sequence used to control the equipment and confirm the presence of magnetically trapped atoms, time t is relative to the start of an experiment run.

[1] The imaging system was constructed by Rhys Jenkins

At $t = 0$ the quadrupole coils come on at 26 A and the dispenser at 3.4 A to form a MOT, the dispensers slowly dispense rubidium during 50 s. After the dispensers go off the coils remained on for a further 15 s which allowed the ion pump time to remove background rubidium in the chamber whilst holding the MOT. At $t = 64900$ ms the camera takes a fluorescence image of the MOT. At $t = 65000$ ms the shutter turns off the laser light and the coils jump to 207 A, this creates a magnetic trap which is held for a variable time t_{Btrap}, which includes feed forward times (see section 3.3.6). At $t = 65000 + t_{Btrap}$ ms the coils would return to 26 A and the shutter would re-open allowing a MOT to reload, the camera was triggered to take images of the reloaded MOT at $t = 65000 + t_{Btrap}$ ms and at 5 s intervals thereafter. For comparison the experiment was repeated but with the coils going off (current = 0 A) for the duration of the magnetic trap forming. This control measurement confirmed how long the MOT atoms would take to disperse out of the MOT beam intersection and can be used to estimate the temperature of the MOT.

Feed Forwards

In reality it is not possible to turn on beams and coils instantaneously, a finite amount of time is required however we will attempt to minimise this, ideally for this experiment we would like millisecond precision. The shutter can actuate in a few hundred micro seconds. The coils have a comparatively large inductance and rely on MOSFET control which is in turn determined by a PID circuit. The PID circuit was tuned to be much faster than the milli second timescales required, however PID controlled MOSFETs tend to approach the requested current at an exponentially decreasing rate. The rate was improved using the 'feed forwards' technique, the same technique can be used to jump laser locks rapidly [125], (we have sucessfully used this technique to jump our DAVLL frequency by 244 MHz in less than 1 ms in preparation for absorption imaging). A pre-calibrated Hall effect current sensor (HECS) detects the current supplied to the coils by the MOSFET and outputs a signal current which is proportional to the coil current, the signal current is converted to signal voltage by a sense resistor. The computer sends a control voltage to the PID circuit which the circuit attempts to match to the HECS signal voltage by adjusting the voltage on the gate pin of the MOSFET and hence allowing current to flow.

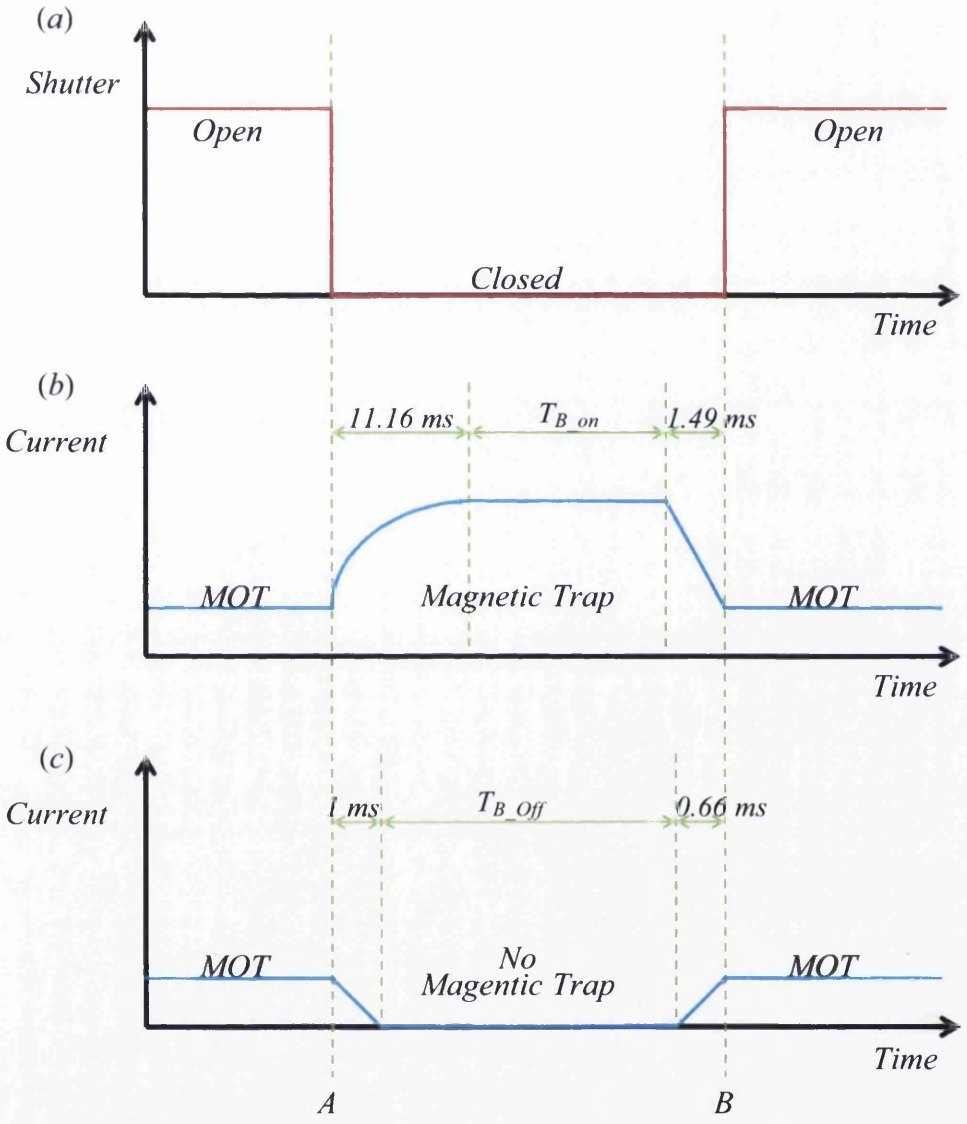

Figure 3.18: Schematic diagram of the experiment timing. (a) Shutter timing, (b) Coil current for the creation of a magnetic trap. (c) Coil current timing for the control measurement with no trapping magnetic field.

We can force the circuit to switch on as fast as possible by outputting the maximum voltage permitted by the computer card during switching, in our case this was 10 V. When the desired current is reached we found it necessary to use a second inverse feed forward step of -10 V to prevent the current continuing to increase, before

finally the control voltage returns to the value corresponding to the desired current. The timings of the feed forward steps were found experimentally. Decreasing the current required a -10 V feed forward step followed by a $+10$ V step, if the current was being switched off altogether the control signal was simply reduced to -10 V. The switching time can be further reduced by having a large additional voltage over the MOSFETs (overhead voltage) which is surplus to that required to run the circuit, however this extra voltage creates significant additional heating to the MOSFETs.

The coil current timing sequence is shown in figure 3.18. Timing points A and B are fixed. 1 ms was allocated in the control program for the coils to turn off in the case of no magnetic trap, however in reality they turn off in much less time (0.31 ms). The duration of the magnetic trap is defined as $t_{Btrap} = B - A$. Note that $T_{B_off} = T_{B_on} + 10.99$ ms. Limitation of the shutter and coil switching meant that data was taken for a minimum value of T_{B_on} of 10 ms ($t_{Btrap} =$ 20.99 ms).

3.4 Results

In this section preliminary results from the magnetic trap are presented which demonstrate its existence but also highlight some of the improvements which are yet to be implemented. We first run a control experiment with no magnetic trap using the coil current sequence shown in figure 3.18(c).

3.4.1 MOT Temperature

When the MOT goes off the MOT atoms (which have some non-zero velocity) will slowly move out of the MOT capture area. The atoms have to move approximately 3 mm to leave this region which is set by the beam size given in section 3.3.3. By varying the time for which the MOT is off T_{B_off} and comparing the image of the initial MOT with the reloaded MOT, we can count the number of atoms which remained in the beam crossing point for a given time. We expect the temperature and hence velocity of the atoms to be a thermal (Gaussian) distribution.

Data is shown in figure 3.19 with a Gaussian fit. The width of the distribution is 26 ms, which for our trap gives a mean atom temperature of 140 μK. The crossing point of the Gaussian fit and y-axis occurs at 0.63. It is not fully understood why 37% of the atoms seem to be lost from the trap immediately, it could be due to

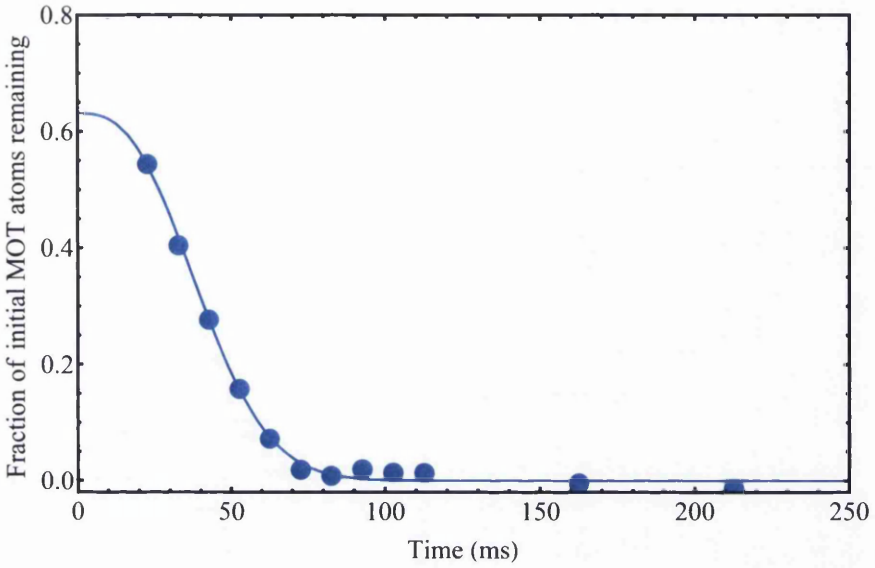

Figure 3.19: Velocity (temperature) distribution of MOT atoms.

several possibilities including; a moving molasses created by imbalance in the MOT beams; natural loss of atoms from the MOT from background collisions or mismatch between the location of the MOT and the quadrupole minimum. Although the MOT generally forms at the minimum of the quadrupole it can be shifted slightly by beam imbalance or beams which are not perfectly orthogonal. Since our MOT is formed by retro-reflected beams we can be certain that the beams are not all exactly the same power since there will be retro-beam power losses from; the vacuum chamber window, the quarter waveplate and the mirror. The vacuum chamber windows for the MOT are not anti-reflection coated. The shutter can actuate to turn off the MOT beams in approximately the same time as it takes the MOT magnetic field to ramp down.

3.4.2 Evidence of a Magnetic Trap

MOT fluorescence was recorded in the camera images of the MOT before the magnetic trap was formed, and after reloading once the magnetic trap has turned off. A film strip of fluorescence from these images is shown in figure 3.20. The magnetic trap was held for varying times and the fraction of atoms in the reloaded MOT relative to the initial MOT was calculated. The fraction as a function of hold time is shown in figure 3.21. An exponential fit is used to estimate the trap lifetime. The

fit results in a lifetime of $\tau = 6.7 \pm 0.6$ s.

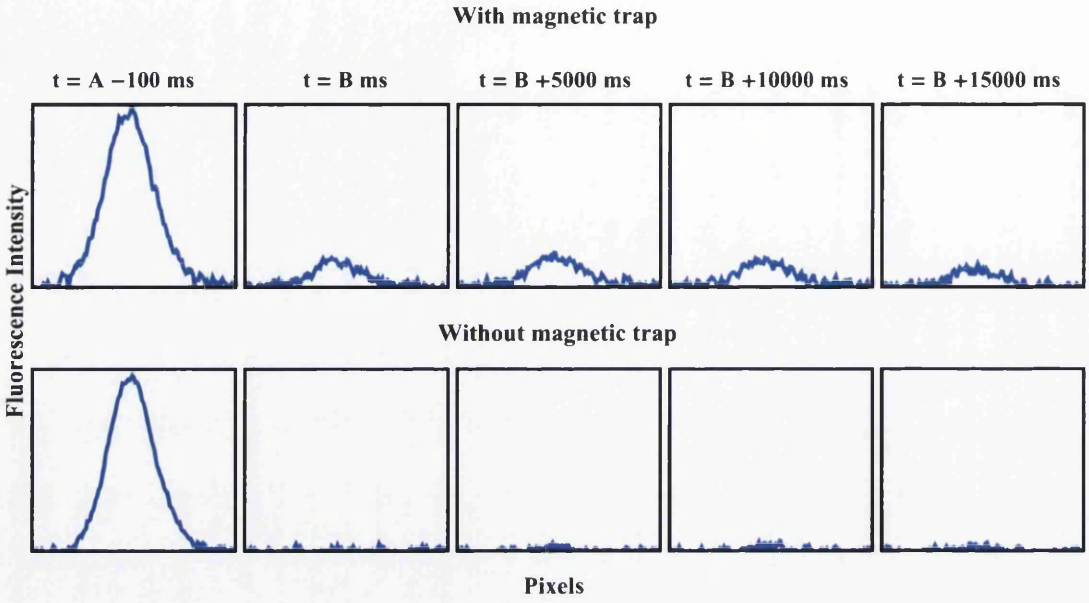

Figure 3.20: A film strip image from the experiment showing MOT fluorescence at various times, timings are given relative to points A and B from figure 3.18. In this example $t_{Btrap} = 513$ ms, the first image is the MOT before the magnetic trap is created (or the coils go off). Subsequent images are the reloaded MOT after the atoms were held in a magnetic trap (or the coils went off). In the case of no magnetic trap some reloaded MOT signal is just visible above the noise, this is due to a small residual background of rubidium which is not pumped away.

Using figure 3.19 as a guide we have removed data which was taken for $t_{Btrap} <$ 100 ms due to the the existence of significant amounts of untrapped atoms which require time to move from the MOT recapture area. The crossing point of the exponential fit and y-axis occurs at 0.21. Assuming atoms in the MOT are approximately evenly distributed in the ground state ($F = 2$) over all the magnetic sub-levels there will be around 40% of atoms in a low field seeking state, another 40% in a high field seeking state (HFS) and the remaining atoms in $m_F = 0$. The HFS atoms will accelerate out of the trap when the MOT laser beams go off. Other losses could be due to absence of a pre-cooling step and there is also a similar unexplained fraction of loss observed here to that observed in figure 3.19.

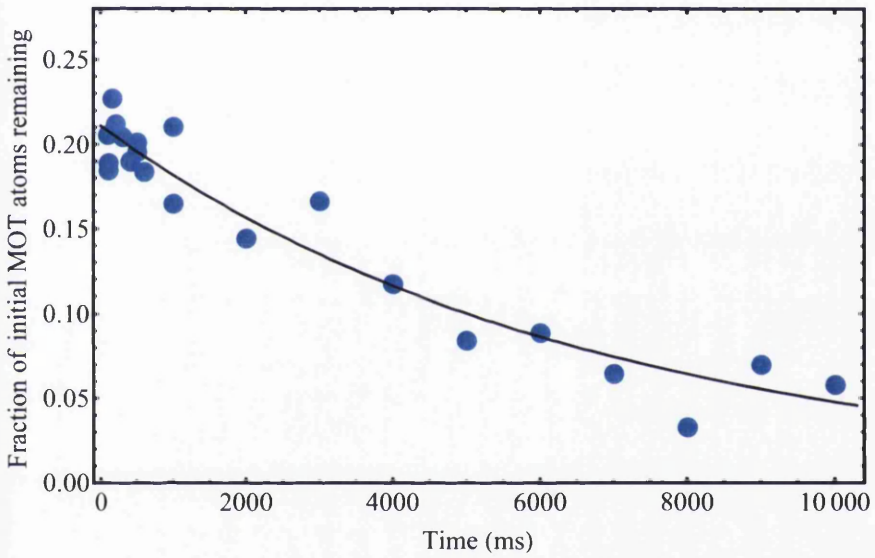

Figure 3.21: Atoms recaptured in a MOT after being held in a magnetic trap for varying times.

Chapter 4

Concluding Remarks and Outlook

4.1 Future Plans

4.1.1 Immediate Improvements to the Setup

The immediate plans for the setup are to optimise and characterise the magnetic trap, in the next few months the absorption imaging system is envisaged to be fully up and running which would allow the trap to be imaged without reloading into a MOT, this will help identify loss mechanisms. Transfer of atoms from the MOT to the magnetic trap will be improved with the addition of a molasses and optical pumping step. A tapered amplifier system has been built which will amplify the laser power to provide several 100 mW of trapping laser power.

4.1.2 Use of Tapered Nanofibres with Cold Atoms

In the future it is envisaged that the bottom CF63 viewport on the chamber will be replaced with a modified CF63 to CF16 adapter piece and CF16 viewport for the vertical MOT beam, the modified adapter piece will enable tapered nano-fibres to be mounted inside the vacuum chamber and the interaction between the evanescent field and cold atoms can be studied [156]. The cold atom cloud can be dropped onto the fibres which act as a single atom detector.

4.1.3 Degenerate Fermi Gas

One of the long term goals for this experiment is the creation of a degenerate Fermi gas of ^{40}K. This experiment will need sympathetic cooling from ^{87}Rb, certain parts,

such as the potassium lasers and some control electronics, have already been constructed.

Rubidium Potassium Mixture

As shown in section 3.2.4 s-wave collisions between identical fermions are suppressed as the cloud becomes very cold, hence re-thermalisation of the cloud for evaporative cooling is not trivial. The addition of a Bosonic atom allows collisions and re-thermalisation to continue. The scattering cross section for ^{87}Rb and ^{40}K s-wave and p-wave collisions have been calculated [157, figure 3.11].

Applications of a Degenerate Fermi Gas or Mixture

With a dual species trap it would be possible to find Feshbach resonances and exploit them, for instance to create diatomic molecules. As previously discussed in the introduction these molecules have exciting applications in the field of quantum computing. The end target for our experiment is to create a simplified model of quarks inside the nucleus using cold atoms (with atoms in different internal states each representing a quark) and tuning their interaction strength using Feshbach resonances [141]. This would be achieved by transferring the cold atoms to an optical dipole trap and applying a homogeneous magnetic field to tune the interactions. For this reason the coils and control electronics for the magnetic trap have been designed to be able to switch from running in anti-Helmholtz to Helmholtz configuration, although some parts of this circuit have not yet been manufactured.

Vacuum Expansion

Currently the MOT and magnetic trap are formed in the same chamber. Dispensing of rubidium and potassium into the chamber significantly raises the vacuum pressure of which only a small fraction ends up in the MOT. In our experiment the MOT must be held for around 15 s after the dispense and loading has ended to enable the background atoms to be pumped away. This can easily be overcome with the addition of a second, almost identical, system separated from the existing one by a narrow tube. A 'high pressure' MOT (HP MOT) is formed by dispensing into the additional chamber and then a beam of cold atoms transferred to the 'low pressure' MOT (LP MOT) by a push laser beam. This allows fast reloading of the LP MOT without increasing the pressure in this chamber because cold, pre-cooled atoms can

be stored in the HP MOT. A proposed schematic of this vacuum setup is shown in figure 4.1.

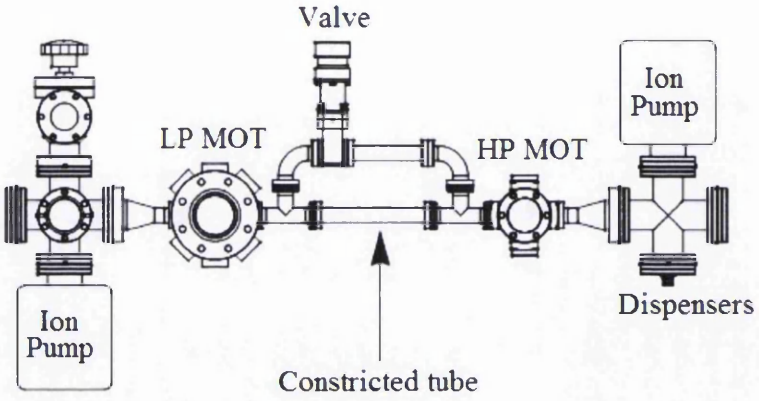

Figure 4.1: Proposal for the addition of a high pressure (HP) chamber separated from the low pressure (LP) chamber by a constricted tube. The constriction can be bypassed for the purposes of baking out.

The new HP MOT would be connected via the blank port on the chamber and the dispensers would move to the new chamber. It had been hoped the ion pump could move to the port being used at the moment by the dispensers, but it was found that this would require shielding of the ion pump magnetic field which has a significant effect on the trap when placed here. The port currently occupied by the ion pump could be replaced by a viewport allowing access for a beam or diagnosis view.

4.2 Summary of Achievment and Concluding Remarks

A novel method of creating microwave sidebands in laser diodes using optical injection has been successfully applied to atomic physics and other applications such as stimulated Raman transitions have been discussed. A MOT and magnetic trap have been constructed and after optimisation of the magnetic trap the experiment will be well on the way to producing a cold multi-species trap. This will hopefully allow new insights into the interactions between atoms on a quantum mechanical scale and may help experimentally simulate QCD by close control of the interaction using Feshbach resonance.

When I started work in the lab there was nothing but empty tables and so both experiments have been constructed from scratch. The construction work carried out to date should provide a sound footing for the experiment to progress.

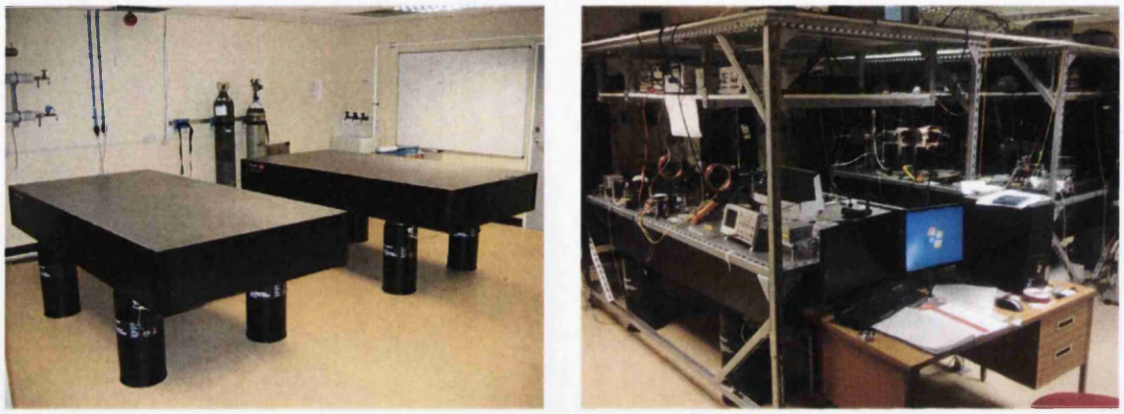

Figure 4.2: Picture of the lab before and after the work described within this thesis.

Appendix

A.1 Vacuum Procedures

A.1.1 Vacuum System for the Injection Locking Experiment

Setup

A Kimball Physics MCF450 spherical octagon chamber with two CF63 ports and eight CF16 ports was used for the main chamber. One CF16 port connected to a CF40 to CF16 conical reducer which connected to a tee-piece on which there was a 20 l/s Varian Starcell ion pump which also acted as a pressure gauge and an angle valve allowing connection of a Leybold TW70H turbo pump and Leybold Divac 2.5VT diaphragm pump. On the chamber the two CF63 ports and four of the CF16 ports were used for viewports for the MOT beams, one CF16 was used for the feedthrough for the dispensers. The two remaining CF16 ports were sealed off with a blank.

Bakeout

For a magneto-optical trap a vacuum of 10^{-7} mbar or less is sufficient, this can easily be obtained with a roughing pump and a turbo pump but in order to maximise the lifetime of atoms in the trap we baked the system for one week at approximately 120 °C. After bakeout the chamber was sealed off from the rough pump and turbo pump with a valve, these pumps were then disconnected from the system. The ion pump does not pump hydrogen very well so a small SAES ST172 (HI/16) non evaporable getter (NEG) pump was mounted in the chamber on the same feedthrough as the dispensers. The NEG pump requires activation by heating it up by running large current pulses of between 3 A and 5 A through its internal heater, the dis-

pensers were degassed at 3 A for 5 h and subsequently run at 2 A for the remainder of the bakeout to prevent bakeout released gasses from forming on the dispensers. This combination gave pressures lower than the ion pump can accurately measure (10^{-9} mbar).

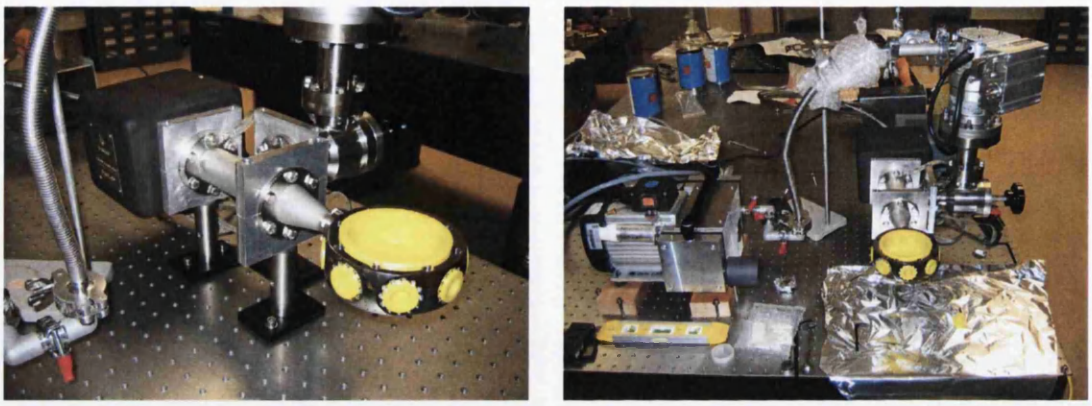

Figure A.1: Injection locking vacuum system under construction and preparing to bakeout once the chamber viewports are added.

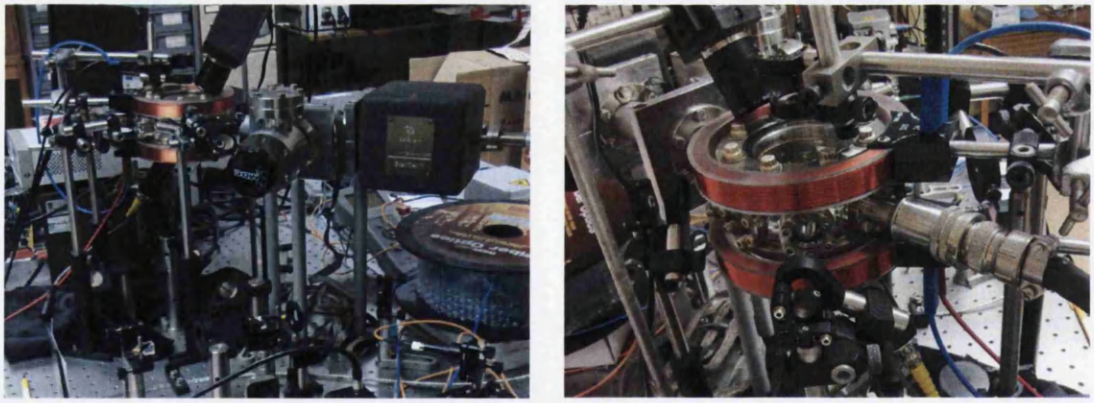

Figure A.2: The finished vacuum system with optics and coils placed around the chamber. The chamber is raised up on posts.

A.1.2 Vacuum System for the Magnetic Trap

Setup and Non-Magnetic Components

The vacuum for the magnetic trap was upgraded as described in section 3.3.3. As mentioned in section 3.3.3 the system was constructed with the aim of minimising the

amount of magnetic SS304 stainless steel. For the magnetic trap the SS316/316LN components were the; cross; conical reducer; imaging beam viewports; top CF63 viewport and the chamber itself. And the SS304 stainless components were the; bolts; CF16 blank; MOT viewports except for the top CF63 viewport and other components connected to the cross which were deemed to be far enough from the chamber to have negligible effect on the field. Note that for bolts SS304 bolts are referred to as 'A2' and SS316 are referred to as 'A4'. Non-magnetic (A4) 8-32 and 5-16 bolts were sourced for use on the chamber viewports however we found serious quality defects with these types of bolts; the A4, 5-16 bolts were more magnetic than their A2 counterparts we had previously used and the A4, 8-32 bolts sheared at torques far below the torques required to seal a CF16 port. It is still planned to replace these bolts with A4-type in the future however further quality checks will need to be carried out first. The bottom CF63 viewport will eventually be replaced with a SS316LN CF63 to CF16 zero length adaptor which has been modified for tapered nanofibres however a second unmodified adaptor piece has been purchased and can be added to the system at a convenient point in the near future. The non-magnetic CF16 viewports were bought as a trial and were extensively tested in comparison to a standard viewport under an applied magnetic field because magnetism details are not available from the manufacturer. It should be noted that the main magnetism problem from standard viewports is due to the kovar seal between the metal and the glass which is very magnetic.

Bakeout

The bakeout procedure was adjusted to account for these new components and additional degassing steps required to reach the desired pressure, this time we used a Pfeiffer HiCube 80 Eco pumping station containing a HiPace 80 turbo pump and an MVP 015 dry diaphragm backing pump, we also used a residual gas analyzer (RGA). Due to the temperature limit of the non-magnetic viewports of 120 °C the system was baked at 110 °C for one week. For nearly all this time the dispensers were held at 200 °C by running a current of 2 A. The NEG causes a severe heating effect to the surrounding nipple, therefore the NEG heater itself was used heat this part of the system and no heater tape was applied here, this also meant the NEG was kept at 250 °C for the week long bakeout which degassed it significantly.

On the last day of the bakeout the dispenser and NEG were activated. Unlike the

previous bakeout we now had the RGA to diagnose gasses released and we found it necessary to outgas the dispensers for longer; current was increased from 2 A to 5 A over 1 h causing the pressure to rise one order of magnitude and was left to degas until the pressure reduced almost to its initial value. Care was taken to keep pressure rises within one order of magnitude to prevent damage to the dispenser. The dispensers were then left on at 2 A for the remainder of the bakeout.
Activation of the NEG requires heating it to a temperature of 650 °C for a period of 150 minutes. During activation the NEG releases large amounts of hydrogen and the pressure rises by two to three orders of magnitude. As the NEG is cooled the gauge was degassed using the built in 'degas function' which runs the gauge filament at high current causing it to become very hot. Due to the presence of a gauge the ion pump did not need to be on during bakeout so this was only switched on just before cooling the system. The valve which disconnects the turbo and rough pump from the main chamber was closed off as the system cooled.

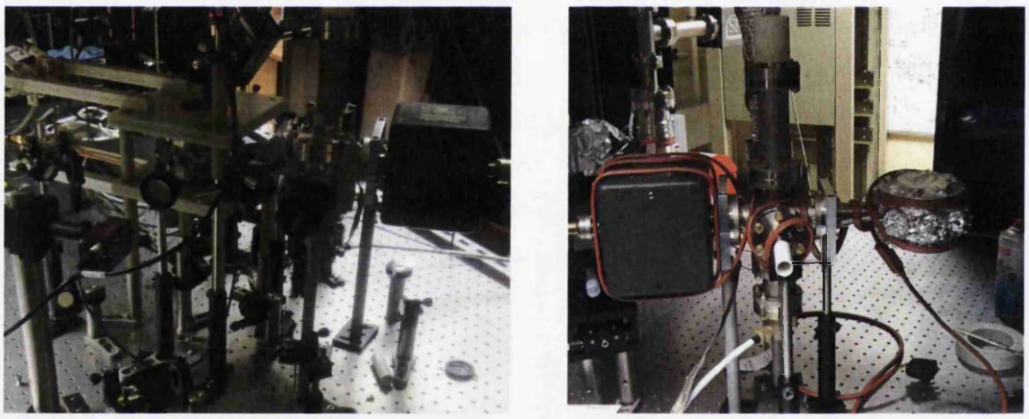

Figure A.3: Chamber with coils and optics wrapped in heater tape in preparation for bakeout.

A.1.3 Chamber Magnetic Fields

No Field Applied

The background magnetic field in the centre of the trap was measured with and without the chamber present. First we measure the background field at the trap centre. The values of $+(B_x, B_y, B_z)$ and $-(B_x, B_y, B_z)$ were measured with and without the vacuum system at the centre of the chamber to estimate the offset of

the instrument on that day. Note that data with and without the vacuum system were taken on separate days some weeks apart. The geometry of the x, y, z axes are as shown in figure 3.9 with the origin of each axis at the centre of the chamber.

With Chamber				
Positive component	Field (mT)	Negative component	Field (mT)	Offset (mT)
B_x	-0.0274	$-B_x$	-0.0156	-0.0215
B_y	-0.0667	$-B_y$	+0.0209	-0.0229
B_z	-0.0374	$-B_z$	-0.0064	-0.0219

Table A.1: Table of field components at the origin.

This gave the background field with the chamber to be $(B_x, B_y, B_z) = (-0.0059, -0.0438, -0.0155)$ mT.

Without Chamber				
Positive component	Field (mT)	Negative component	Field (mT)	Offset (mT)
B_x	-0.0273	$-B_x$	-0.0291	-0.0282
B_y	-0.0366	$-B_y$	-0.0201	-0.0284
B_z	-0.0378	$-B_z$	-0.0200	-0.0289

Table A.2: Table of field components at the origin.

This gave the background field without the vacuum system to be $(B_x, B_y, B_z) = (+0.0009, -0.0083, -0.0089)$ mT. Comparing this to the data above taken with the vacuum system it is immediately evident that the system is having some effect on the field especially in the y-direction. Curiously there seems to be no earth field when the vacuum system is not present. This could be due to the face of the (magnetic) steel optical table acting as a shield. Magnetic north is in the negative x direction, however the two tables within the room bend the field so that the earth field travels in the negative y direction, in the absence of the vacuum system the table acts as a shield and almost no field is measured at the position of the experiment chamber (approximately 30 cm above the table surface). Possibly when the vacuum system is bolted to the table surface it acts like a paramagnet (becoming magnetic in the presence on an applied field) and an earth field is measured inside the chamber in the negative y direction, or the additional field could be directly due to a component

of the vacuum system - the ion pump field for instance. The alignment of the ion pump is such that the return field for the ion pump coils would be along the y-axis. The field was measured for the (B_x, B_z) components along each axis in the region around the axis origin (centre of the trap and location of the cold atoms). The B_y field component was not measured due to the probe being inserted into the chamber along this axis. Results are shown in figure A.4. The probe was inserted into the chamber through a CF16 port hence travel in the x and z directions were limited however the y direction was not. In the figure equal scaling is given to the axis distance hence the larger y - axis graph.

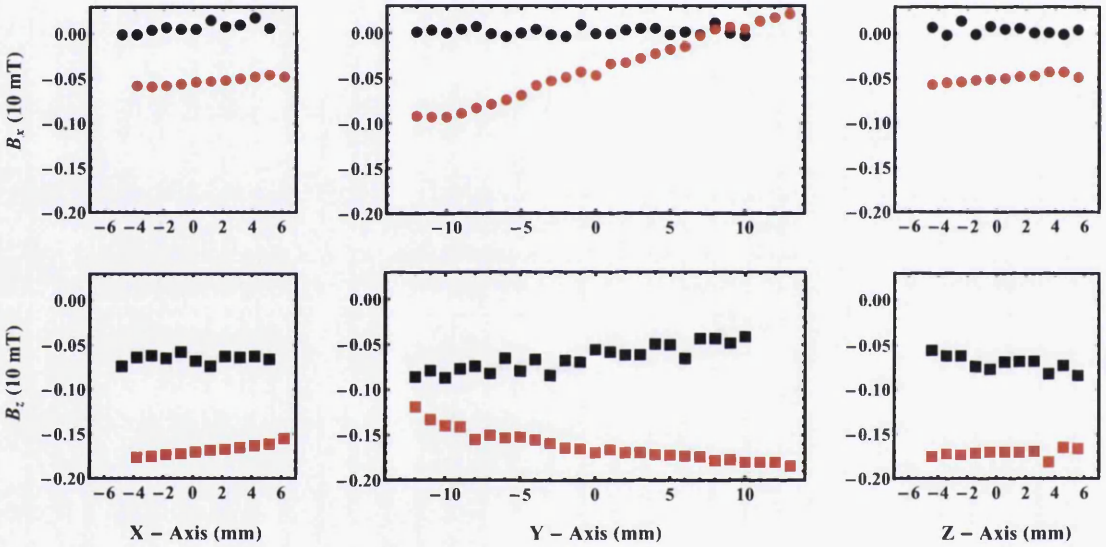

Figure A.4: Black are data without the chamber present, red points are data with the chamber present. Fields measurements are the positive field component with the offset removed.

In the absence of the vacuum system (black) there are only small field gradients which are likely to be due to the spatial variance in bending of the earths magnetic field. When the vacuum system is present more significant B_x and B_z field gradients were observed particularly along the y-axis. The B_x field could be due to the return field of the ion pump and may be solved with further shielding, the B_z field is less easy to account for and is likely to be due to the chamber components, most probably the bottom CF63 viewport which is magnetic and will contain kovar (we intend to replace this). Field gradients of this order are not a problem for the magnetic trap but could cause problem exciting or controlling Feshbach resonances

in a falling cloud of atoms.

Helmholtz Field Applied

The disturbance, due to the vacuum system, to a homogeneous field applied along the z-axis was investigated, in figure A.5 the field component in the z-direction was again mapped on the x, y and z axes with and without the chamber present. In the presence of the chamber (red points) the field becomes far less uniform around the centre compared to data taken without the chamber (black points), most notably when moving along the z- axis. It is likely this is an effect of the bottom viewport (at negative z) being a normal magnetic viewport.

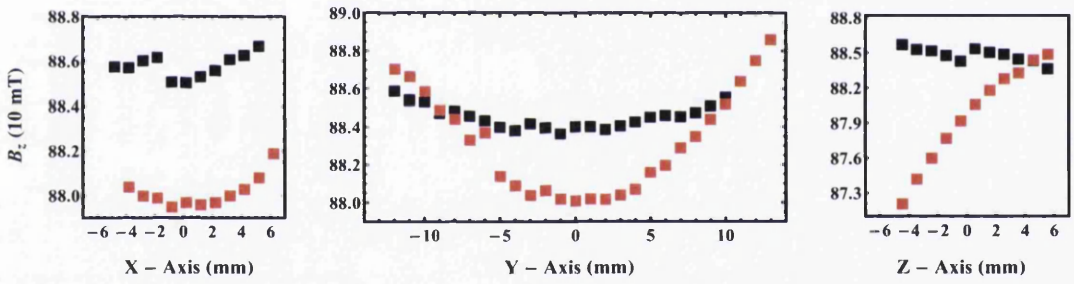

Figure A.5: Axial field component of a Helmholtz field with and without the chamber.

Chamber Effect on Coil Switching Time

The rise and fall time of the magnetic trap coil current from 0 A to 207 A is studied with and without the chamber and optics present using the output from the hall effect current sensor.

The turn off time is shown in figure A.6. At time t = 0 ms , which is indicated by a vertical line in the figure, the control voltage drops to −10 V. The current sensor output with (red) and without (black) the chamber present are overlaid and there are no significant differences.

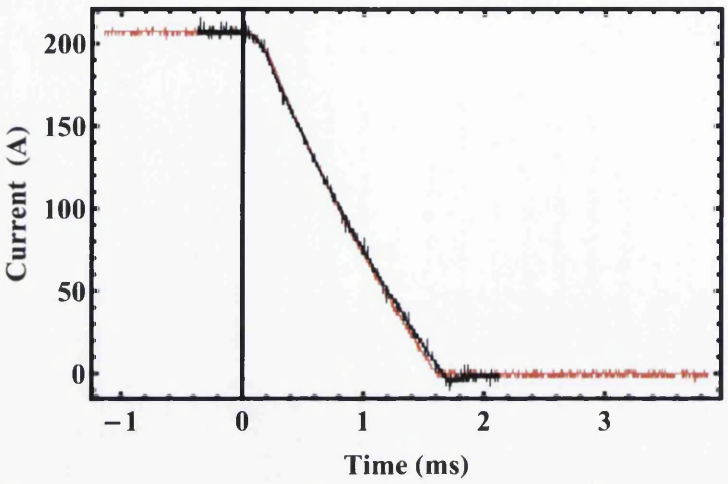

Figure A.6: Coil turn off with (red) and without (black) the chamber.

Switching the field on was done using a 10 V feedforward voltage for 10 ms followed by a brief −10 V for 0.16 ms secondary feedforward step shown in figure A.7(a), this was found to work well without the chamber (A.7(b) black). However when the chamber was added the same control sequence did not work as well as before (A.7(b) red), the traces were identical until the negative feedforward step where it appeared the positive feedforward step had gone off too early.

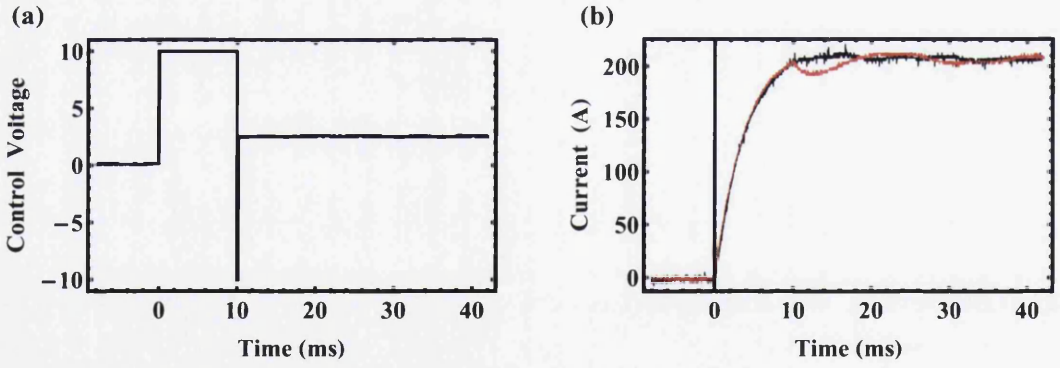

Figure A.7: (a) Control voltage sequence, (b) current response with and without the chamber (red and black).

This control sequence was adapted slightly to have a 10 V feedforward voltage for 11 ms and a −10 V 0.14 ms secondary feedforward step shown in figure A.8(a). This produced the red trace shown in A.8(b) which is overlaid on the black trace from figure A.7(b) for comparison. The two traces are reasonably well matched.

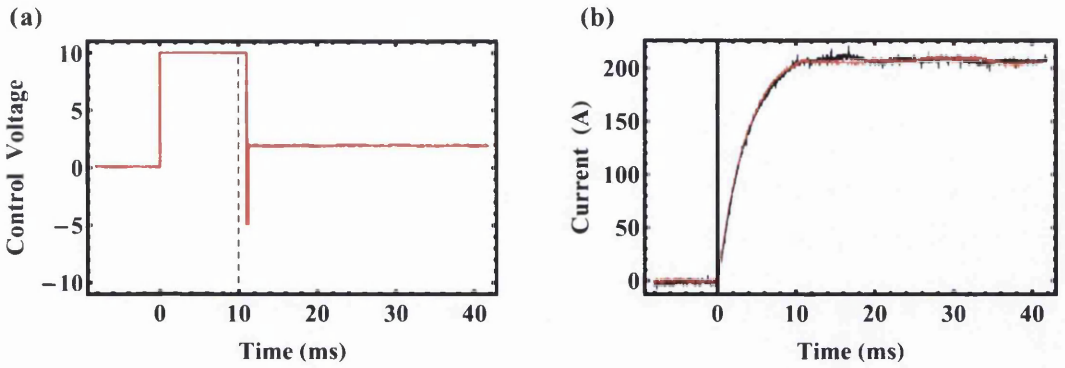

Figure A.8: (a) Control voltage sequence for with the chamber present, the dashed line indicates the end of the 10 V feed forward voltage used in figure A.7(a). (b) current response with the chamber (red) overlaid on current response without the chamber using the control sequence in figure A.7(a).

The eddy currents caused by the chamber being present creates a resistance to the increase in current which does not significantly affect the current rise time but does affect whether the current continues to increase or level off when the negative feed forward step is used. However it has been demonstrated here that the control voltages can be adapted to negate these effects.

A.2 Making Coils - Modelling and Construction

A.2.1 Coil Modelling

Criteria

The coils created for the magnetic trap had two basic criteria. They must be able to produce a quadrupole field with large field gradient for magnetic trapping and also be able to create a strong homogeneous field to excite Feshbach resonances for rubidium, and potassium. The depth of the magnetic trap is related to the field gradient produced by the anti-Helmholtz field, for an atom moving in a magnetic field B with the state $|IJFM_F>$ with temperature T we can simply equate thermal kinetic energy k_BT to the magnetic dipole energy $g_F\mu_BM_FB$ to find the trap depth. Since B is dependant on the current density within the coils we must maximise the amount of current flow. The obvious way to do this is to use many tightly packed coil turns but for our trap to work we must also be able to switch the coils on and off in a few milli seconds or less. The turn-off time for a coil is related to its inductance

L which is related to the rate of change of the current I:

$$v = -L\frac{dI}{dt} = IR \tag{A.1}$$

In this case we are considering the turn off time so the change in I with respect to t is negative. Rearranging this and integrating we obtain

$$\int \frac{R}{L}dt = -\int \frac{1}{I}dI \tag{A.2}$$

$$\frac{Rt}{L} = -Log(I) + K \tag{A.3}$$

Using the boundary condition that at t = 0 the current is I_0 we can re write this as

$$I = I_0 e^{-\frac{Rt}{L}} \tag{A.4}$$

Hence the larger the inductance the longer the turn on / off time. The inductance for a multi layered coil of n turns with a mean radius a, height b and thickness c in units of millimetres can be approximated to about one percent [158] by using the following equation:

$$L = \frac{1}{25.4}\frac{0.8 \times a^2 n^2}{(6a + 9b + 10c)} \tag{A.5}$$

Modelling the Field

From equation (A.5) L is proportional to n^2 and so reducing the number of turns will dramatically improve the turn on / off time. In practise this means that very few turns of thick wire running very high current are required. A coil with an inner radius of 28 mm, 4 turns high and 6 turns thick of 4 mm × 4 mm wire was found to be a good compromise. Although higher current and fewer turns reduce the inductance, the maximum current is set by the amount of current which can reasonably be controlled. Our coils were based around the design of previous work from other groups [145, 157] but were modified to fit our geometry and cooling capabilities, we also developed the winding technique which is documented later on. Using the coil dimensions in equations (A.4) and (A.5) gives an inductance L of 45.2 μH and time constant $1/(R/L)$ of 4.46 ms, which is in approximate agreement with the current response without the chamber present in figure A.7(b). Most of the coil dimensions were set by geometry of the chamber and attempts to minimise heat generation and

maximise the field. The inner radius of the coil is approximately equal to the visible radius of the top viewport of the chamber and the separation between the two coils is kept to a minimum (to be as close as possible to the Helmholtz configuration), the separation was 94 mm at their closest face. For ease of winding a rectangular cross section was used for the coil.

The field generated by a coil was modelled using finite element model created in Mathematica with an add-on called Radia [159] and also using an analytical model which integrates the Biot Savart law over the wire path to find the magnetic field at a point in space. The Biot Savart law for an infinite length of wire l is given by:

$$B = \frac{I\mu_0}{4\pi} \int \frac{d\mathbf{l} \times \mathbf{r}}{|r|^3} \tag{A.6}$$

Where r is a vector describing a point away from the wire at which the field is computed.

The two models are shown graphically in figures A.9 and A.10. The models were used initially to estimate fields that would be obtained from different coil dimensions but also to find how best to exit the wires form the coil without disturbing the central field.

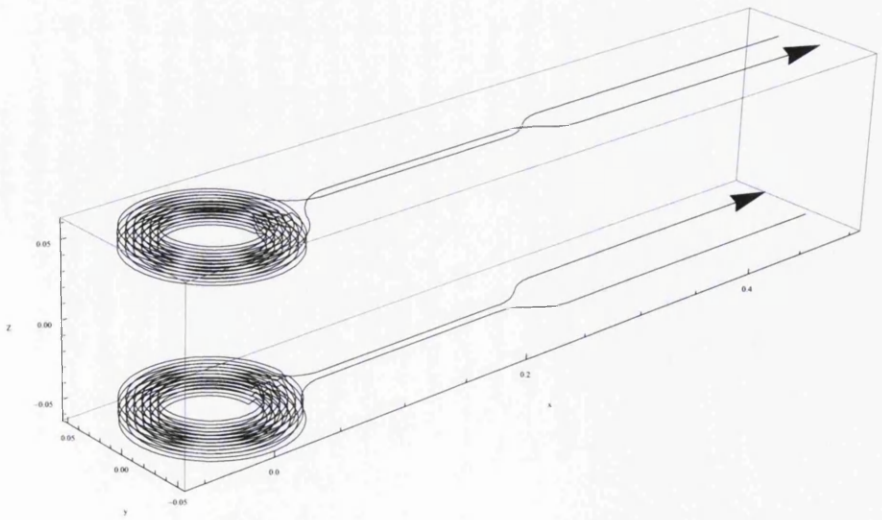

Figure A.9: Analytical model of the coils, current is modelled as a finite vector.

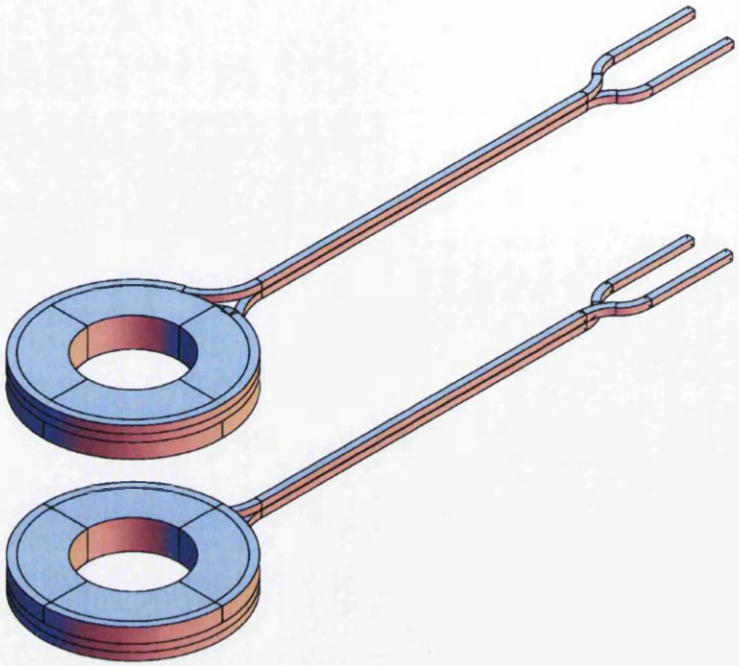

Figure A.10: Finite element model of the coils using a mathematica addon called Radia.

Modelling the Cooling and Water Flow

Modelling the field and coil inductance also demonstrated that water cooling was going to be required to run the amounts of current desired. From modelling it was deemed that hollow square wire (4 mm × 4 mm) with a 2.5 mm circular hole in the centre would be appropriate, the following calculations can be used to estimate the amount of water cooling required and the flow of water that can be expected through the pipe.

Output power P_{out} for a current I running through a resistance R is given by

$$P_{out} = I^2 R \tag{A.7}$$

The resistivity of pure copper is 1.68×10^{-8} Ωm. Using this value we find our coils, which use 6.7 m of wire (including exit wires), will output approximately 2 kW each at 440 A (the maximum output current of the Agilent 6690A, power supply). For a mass flow rate q and temperature difference between the input and output water

of ΔT we can say the system is in equilibrium when the cooling water is carrying away the amount of heat energy generated by the coils.

$$P = cq\Delta T \tag{A.8}$$

where $c = 4.18$ J/K is the specific heat capacity of water at room temperature. The flow rate for a straight pipe of length L and radius r can be calculated using the Hagen Poiseuille formula [160]:

$$\Delta p = \frac{8\mu Lq}{\pi r^4} \tag{A.9}$$

where μ is the dynamic viscosity of water and Δp is the pressure difference over the pipe. The dynamic viscosity is a function of temperature and decreases rapidly as the water heats.

To estimate flow in curved pipe it is possible to solve the Darcy Weisbach equation [161] given by:

$$q = \left(\frac{d}{2}\right)^2 \pi \sqrt{\frac{2\Delta pd}{fL\rho}} \tag{A.10}$$

Where ρ is the water density, however in principle estimating the friction factor (f) caused by roughness of the pipe wall and curved pipe can be difficult. In a straight pipe with lamina flow $f = 64/Re$ where Re is Reynolds number.

Flow rate as a function of pressure difference for the coils used is shown in figure A.21.

A.2.2 Coil Construction

Construction Problems

Using such thick wire to construct coils creates a number of challenges, the wire is more accurately described as thin copper bar than wire because, unlike other wire, once it has been bent into position it work hardens and is difficult to re-bend to another position, this makes it important to bend the wire correctly on the first attempt.

The turns must also be isolated from one another, this is done using a kapton coating which is flexible and resistant to high temperatures. The kapton coating is applied to the wire as an 8 mm wide strip which is wound around the wire.

Each coil must have two wires connected to it to bring in electrical power, for ease of connection, and to minimise the effects from any stray magnetic field on the trap, the wires must both connect to turns on the outside edge of the coil. With traditional coil winding the coil is wound from the inside out with successive layers building upon one another, but this leaves one end connection on the inner turn. To solve this the technique of backwinding was used which is described in section A.2.2.

The Coil Former

A detachable aluminium coil former was designed. The former was made of two (top and bottom) plates which could be independently removed and a central former core to which the plates were bolted and the wire was wound around. The bottom plate was a larger radius and had two holes which could be used to bolt down an outer turn of wire. The former design is shown in figure A.11.

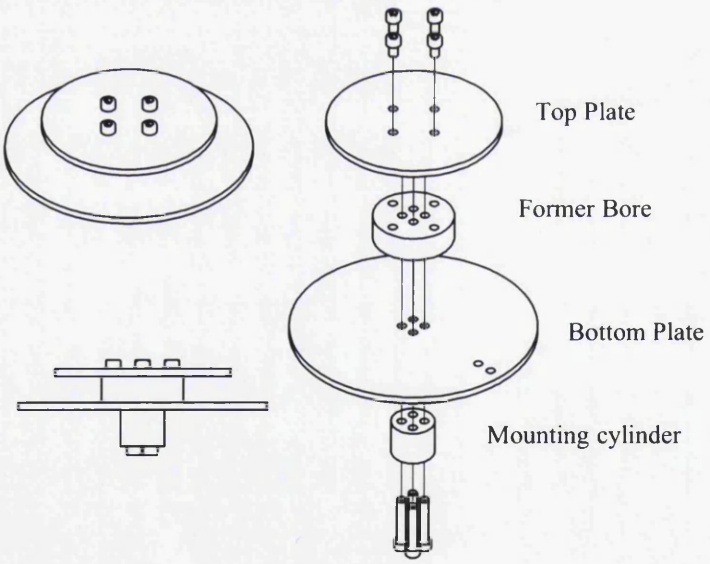

Figure A.11: Isometric, exploded and side views of the former used to wind the coils. All holes in the former bore part are tapped to allow the top plate to be removed, the mounting cylinder allows easy mounting in a mechanical chuck. Two holes on the outside edge of the bottom plate allow one end of the coil to be clamped in place once wound

Winding Method

The method was as follows

1. The wire is 4 mm × 4 mm square profile wire with a 2.5 mm circular hole in the centre. It is kapton coated by an external company and delivered on a reel approximately 50 cm in diameter. The wire is annealed and will work-harden if bent unnecessarily potentially making the winding process more difficult. The wire comes with a natural curvature due to being wound on the reel which we preserve until that particular section of wire is wound onto the former. All windings are made by tightening the radius of the natural curvature. Tipping the reel slightly enables enough wire to be slid off the side of the reel without being removed as straight wire. The coil with exit wires requires 6.7 metres and we allow an extra metre for each end so 8.7 metres is cut from the reel.

2. The coil former and clamps which are to be used are greased with Vaseline and then covered with Mylar before applying another layer of Vaseline, this helps prevent the coil becoming glued to the former.

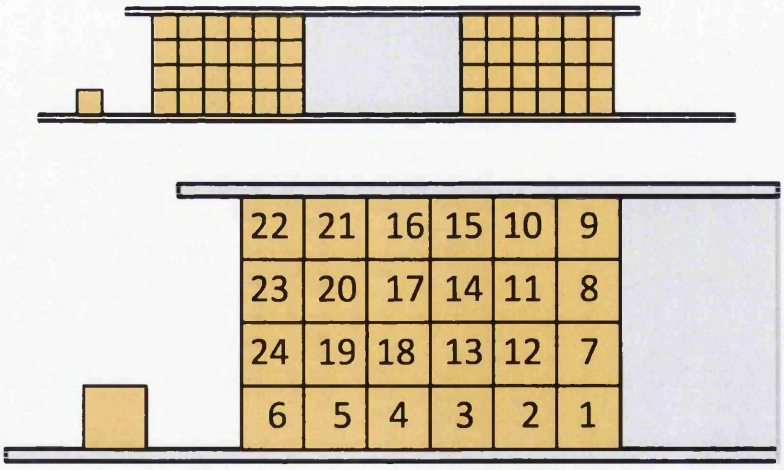

Figure A.12: A cross sectional diagram of the former and coil turns indicating the order in which each turn was made.

3. The coil former is held in a turn-table with the axis pointing vertically, initially the top plate of the former is removed because it is not required at this stage.

We first make the 'back windings' labelled as turns 1 - 6 in fig A.12 which require us to start 2.6 metres from the end of the wire, the remaining wire must be held up above the former so that the back winding can pass underneath it, this was done using retort stands. For this part the turn table is held fixed and the back-winding wire rotated around the former. A second person or a clamp holds the inner turn in place as the wire is wound, this is because when tension is applied to the back winding wire the inner turn will try to jump upwards into the place of turn 7.

4. As the turns are made the wire will naturally try to twist, we suspect this may be due to the tension within the wound kapton coating. Unlike on a lathe, the winder has the freedom to move the wire in their hand to counteract this because the former is fixed. For example, if the wire begins to twist counter-clockwise with respect to the wire direction then the winder can very easily fix this by rotating all the remaining wire in their hand clockwise as they continue the turn, or holding the remaining wire at whatever angle counteracts the twist. All six turns are made and at this stage no adhesive is applied and it is not important for the wire to be held under constant tension as long as the inner turn is prevented from jumping upwards as described above.

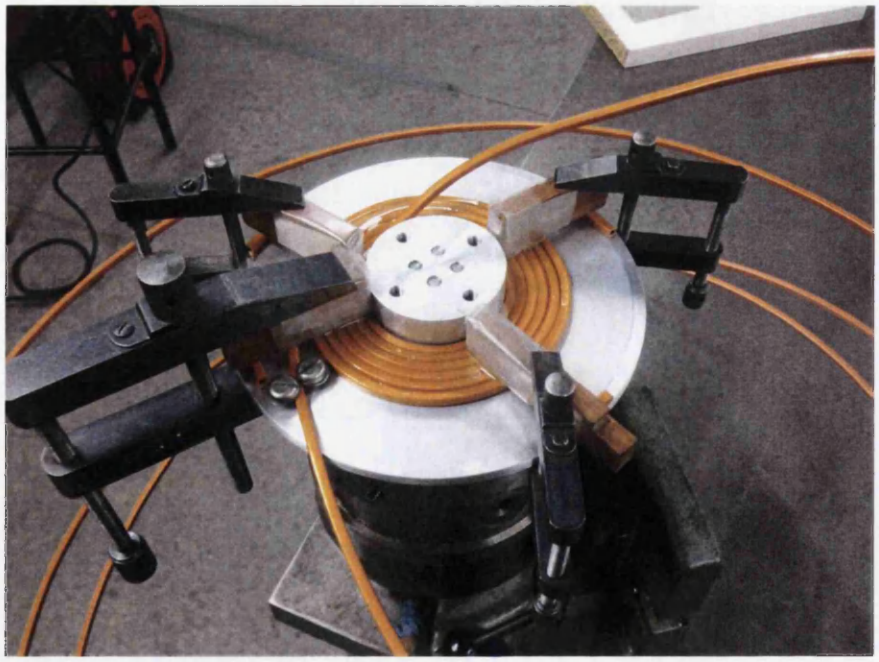

Figure A.13: The coil on the former after the base layer has been wound.

5. When all six turn have been made the coil can be pulled tight A second person can push down on the turns to prevent them jumping out onto the layer above and can also help tighten the inner turns by encouraging the outer turns to rotate. Clamps shielded with wooden blocks are then placed on the coil and the wire end clamped by two bolts. The wooden blocks ensure the metallic part of the clamp does not come into direct contact with the wire which could scratch the kapton coating. Epoxy resin is now applied to the coil without removing it from the former, we used Araldite precision two part epoxy. Gently heating the epoxy with a heat gun increases its viscosity and helps it to flow into all the gaps, the clamps can be removed one at a time and then replaced to apply glue underneath. This was left to cure overnight. See photo (figure A.13).

6. After curing overnight the clamps -but not the bolts holding the wire end- can all be removed. Underneath the clamps glue will have flowed around the side of the block and this must be carefully removed with a small file along with any other excess glue. The top plate of the former is then replaced.

7. The remaining turns (7-24) are now made in order as shown in fig A.12. The turntable is rotated to form the turns and glue is applied to the wire just before it is wound. The back winding end of the wire is held by the bolts. Tension should be applied to the other end and maintained during the winding process, this means the turns will naturally form in the correct place but they can be guided into place by the person keeping the tension and also correct for twists in the wire by rotating the wire in their hand. A second person must apply the glue, turn the turntable and occasionally use wooden tools to push the wire into the correct place, e.g if one turn tries to fall due to gravity such as in the case of turn 10. The last turn of each layer 9,12,15 etc should be prevented from 'changing layer' too early. This is mainly solved by keeping the tension but the second person can also push the turn into the correct place and apply force towards the former axis to prevent a layer change occurring too early. At a layer change there is a significant gap which should be filled with adhesive to prevent an air pocket occurring.

8. When all turns have been completed the end of the wire is clamped to maintain the tension whilst the adhesive cures. The adhesive is left to cure overnight

but after a few hours the top plate was loosened from the former and gently tapped from the side with a mallet causing it to move sideways slightly, it was then replaced and re-bolted in position. This weakens any adhesive bond forming between the former top plate and the coil.

9. The coil was removed from the former the next day and excess epoxy carefully filed away.

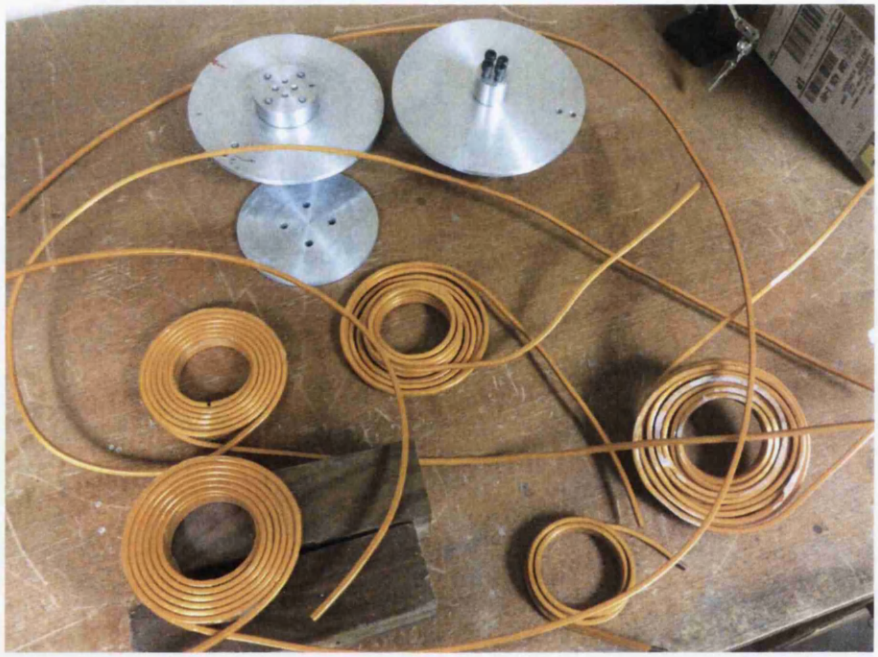

Figure A.14: The removed former (top) with the final coils (bottom left), alongside other practice attempts used to determine the winding technique.

Electrical Connection to Square Wire

Transporting current of up to 440 A requires substantial cable or copper bar and since we hope for the coils to move whilst running several hundred amps in future experiments the connection must be flexible. Welding cable is capable of carrying this kind of current. We use Eland cables H01N2-D type welding cable with a cross sectional area of 70 mm^2 (part number A2G070E) which is capable of carrying 440 A for 60% of a 5 minute duty cycle. The duty cycle increases for lower current.
We terminate the wire with crimp terminals (Thomas & Betts, T70-10, or Farnell 1208209), special clamps were designed to interface between the terminals and square wire.

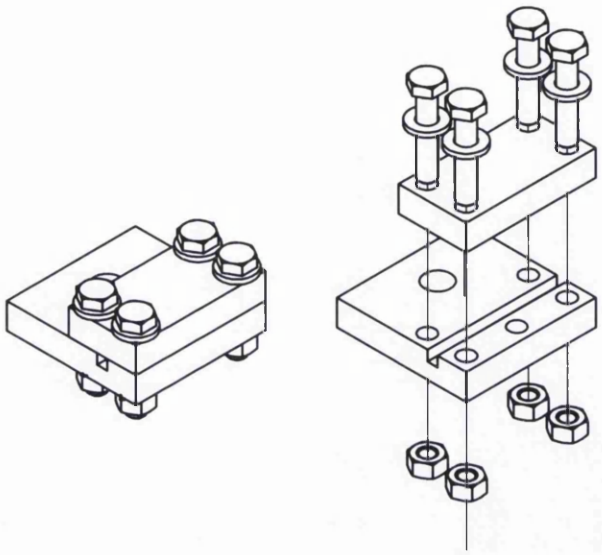

Figure A.15: Copper clamps to interface between the crimp terminals and square wire.

The clamps are made from copper busbar supplied by Metelec (British standard C101, EU CW004A), a bar of profile 50 mm × 10 mm is used to make the parts shown in figure A.15. A 3.9 mm × 3.9 mm groove is cut into a larger square (50 mm length) piece, the groove was initially cut smaller and iteratively increased in 0.1 mm steps until a scrap piece of the square wire could be snugly inserted. The wire itself is 4 mm × 4 mm square profile and so the wire will be slightly deformed under pressure when the top part of the clamp is applied, this compression of the wire optimises surface to surface contact to give good electrical connection on all four faces of the wire without constricting the inner bore.

The clamps themselves can be re-used, however it is likely that clamping and un-clamping may over time result in poorer electrical connection due to the slight deformation of the wire, care was taken to apply the clamps correctly to the coils on the first attempt and they should only be disconnected if absolutely necessary.

No excessive heating has been observed in the clamps when under operation at high current indicating the electrical connection is good.

A 10 mm hole in the clamp allows connection to the crimp terminals mentioned above, the clamps are reasonably heavy and so another 6 mm tapped hole allows for connection to a mounting piece described below.

Tufnol 10G/40 Coil Mounts

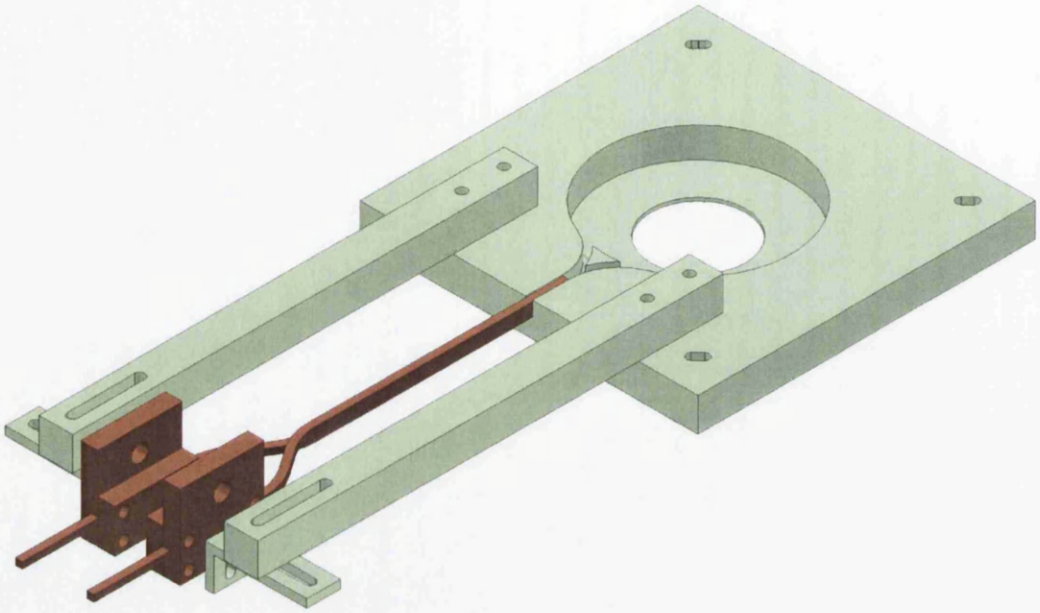

Figure A.16: A single 10G/40 mount shown with the coil exit wires and copper connectors but without the coil.

Any metallic parts close to the coils are likely to increase the switching speed of coils due to additional eddy currents in these parts, hence why the metallic former was designed to be removable, however the coils and electrical connections must be mounted and stable around the chamber. The material used for the mounting system was an epoxy bound fibre glass laminate (tufnol 10G/40), it is an extremely strong and rigid material which can be used for temperatures up to 130 °C.
Two almost identical mounts shown in figure A.16 were constructed. The circular hole houses the coil, however, we found each coil had slight differences (on account of winding by hand), in particular related to the outer turns and how the wires bend to exit the coil, and so the hole and exit wire grooves had to be cut on a trial and error basis. The coils were glued into the mount using epoxy.
A bar and L-shaped piece of tufnol were used to support the copper electrical clamps, and support posts, shown in figure A.17, were also manufactured from 10G/40. Where possible brass bolts were used to assemble the mount.
The whole 10G/40 assembly has been desgined so that it could be mouned on an

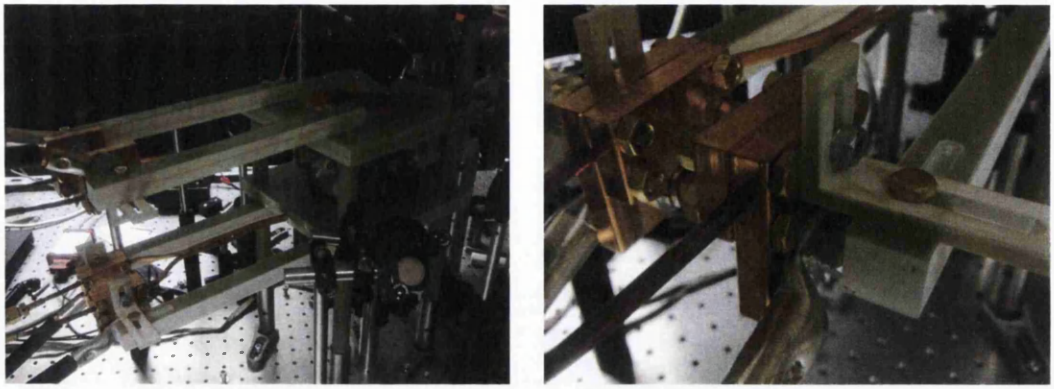

Figure A.17: 10G/40 coil holder and copper clamps.

electronic translational stage so that the magnetic trap could be moved to another part of the chamber.

A.2.3 Water Cooling System

Chiller and Plumbing

A NESLAB system 1 recirculating chiller provided the cooled water for the coils. The chiller acts as a heat exchange removing the heat from the load to a separate in-house cooling water supply. The chiller also provides water pressure to pump the water through the coils, however, the pump runs at a constant speed and so the system pressure is determined by the flow of water through the equipment. A pressure of $4 - 5$ bar was found to be a good operating condition giving flow in each coil of approximately 17 ml/s. The pressure was controlled by partially opening the valves of the bypass whilst observing the pressure gauge on the chiller. Two manifolds were used to split the water supply into four. We used a manifold with built in ball valves which is suitable for use with domestic hot water systems. To avoid risk of burns the system has been designed so that there is sufficient flow that water in the hot manifold is much less than 60 °C. All components were specified to higher temperatures and their pressure specifications exceed the maximum of the chiller ($\sim$ 7 bar).

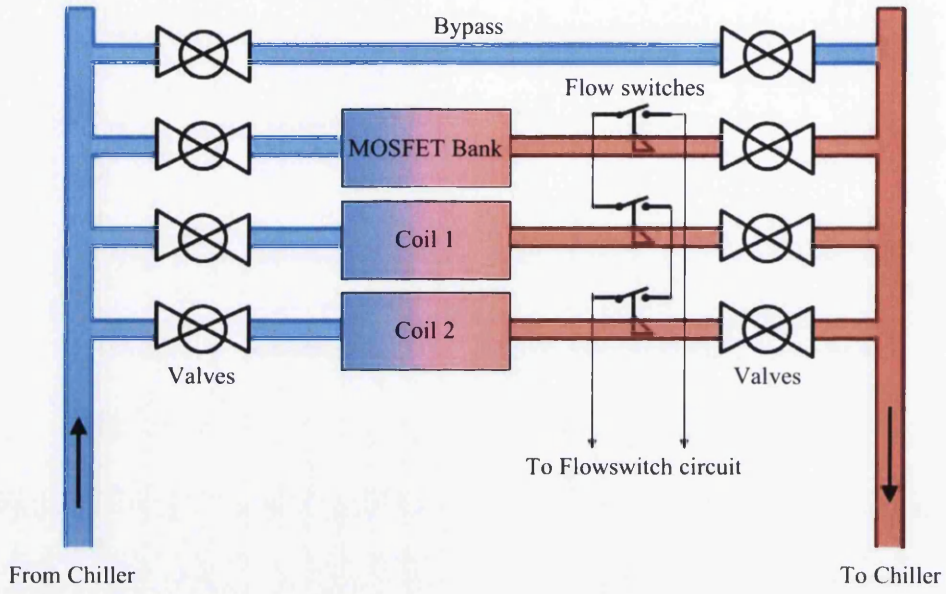

Figure A.18: Schematic of the cooling water flow

Flow Switch Safety Circuit

The coils present a significant safety concern if left running at high current in the absence of cooling water flow. This could result in melting of the coils or their mounts, or the creation of superheated steam inside the coil. To prevent such failure modes a flow switch monitors the flow of cooling water through each coil and the MOSFET bank. An inhibit function is activated in the coil power supply if a fault occurs. The circuit diagram of the saftey switch used to do this is shown in figure A.19.

The position of the flow switch is also important - it must be placed after the coil or device which it is protecting in the flow circuit, otherwise a leak after the flow switch but before the coil will reduce, or stop, the flow in the coil but create a flow-is-true state in the flow switch.

We used Gems Sensors 156265BSPP-RS (RS 395-6928) rotary flow switches, a trimmer on the rear of the device is used to set a minimum flow rate below which the two output pins of the device will be open and an LED on the switch lights up

indicating no flow. When flow is true the two pins short together. We also tried reed type flow switches such as RS 510-0571, however these switches were found to easily be damaged if air got into the system and passed through the switch because this caused the switch to actuate and re-actuate very quickly, the failure mode in this case is that the switch gets stuck in flow-is-true mode!

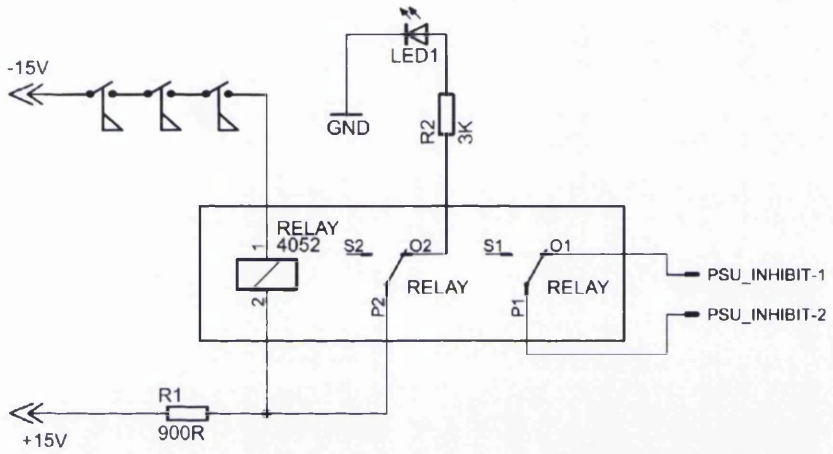

Figure A.19: Relay circuit to short the PSU inhibit pins if one of the three flow switches is open (flow-is-false). The relay is spring loaded and any power failure to this circuit or a flow switch will cause the relay to revert to the inhibited state of the power supply.

Plumbing Square Wire

In the future we would like the coils to be able to move on a mechanical stage, this necessitates the coils being plumbed to the manifold using flexible hose.
Connecting square profile wire to a round hose is not easy. This was done as follows:

1. The excess wire from the coils is cut to a length which allows room for electrical connection and is sufficiently far from the coils to have no significant effect on the field, approximately 350 mm was left including exit curves of the wire. This allowed a straight section of approximately 150 mm where the wires were adjacent (and hence their magnetic field roughly cancelled) before the wires were bent to separate them and attach electrical connections.

2. The ends of the wire are stripped of the kapton coating and filed until round and small enough to fit into the stub end of a B-400-R-4 Swagelok adaptor piece. A snug fit is best.

3. Silver soldering is used to join the the wire and swaglok adaptor, care must be taken to ensure no solder enters the bore of the wire and nuts and olives should be removed from the Swagelok part.

4. The soldered Swagelok adaptor can be shot blasted to remove dirt from the soldering process which may prevent it from forming a good seal.

The Swagelok adaptor can then be connected to rigid 6 mm pipe or in our case a flexible 6 mm hose via a stub to hose tail adaptor piece such as a Swagelok B-4-HC-A-401. Care must be taken to avoid bending the wire near to the water connector because this section of wire will have been annealed and will be very soft.

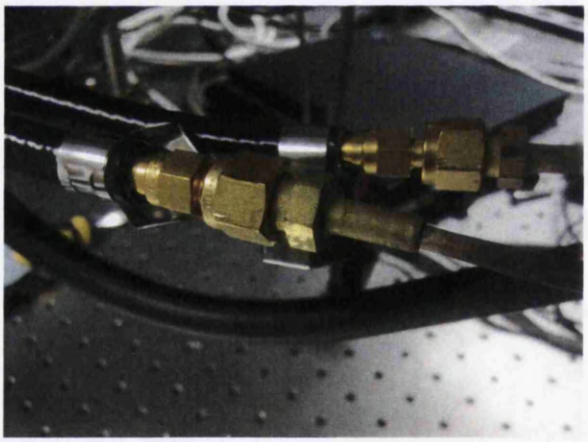

Figure A.20: Swagelok connector silver soldered to square wire.

Flow Vs Pressure

The water pressure vs flow rate for one of the coils is shown in figure A.21. Only one point is taken at high pressure to avoid potential damage to the chiller, other points were taken using pressure in a standard water tap. The flow up to 2 bar is linear with pressure which implies laminar water flow. Using the flow rate expected from a straight pipe given in equation (A.10) and fitting to the data, we find the friction factor (f) from equation (A.10) is increased by a factor of 1.94 from that of a straight pipe due to the coiling of the wire.

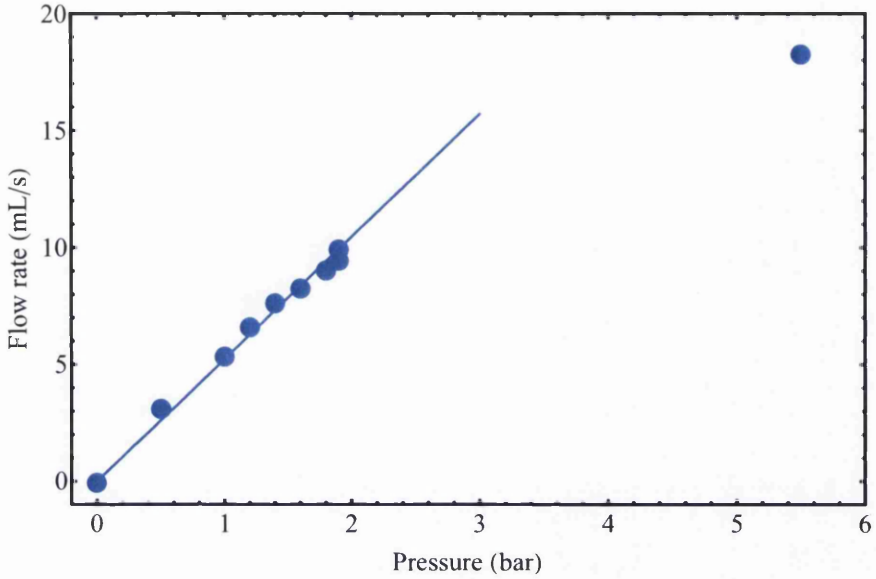

Figure A.21: Flow rate as a function of pressure through one coil.

A.3 Control Circuits

A.3.1 Lock Box Circuit

The initial design of the laser lock circuit is documented elsewhere [162], however more of these circuits were made during this project.

The circuit was originally designed with only the proportional an integral parts of the PID circuit but the derivative part was added at a later date. Using the technique of feeding forwards and combining with a DAVLL spectrometer this circuit is able to jump our lasers by several hundred MHz in less than a milli second. An external offset can be input via the EXT_IN connection enabling computer control of the lock frequency. The circuit was designed to output to a laser piezo (which controls the external cavity length), however we found this circuit also worked very well when locking our slave (re-pump) laser by current modulation.

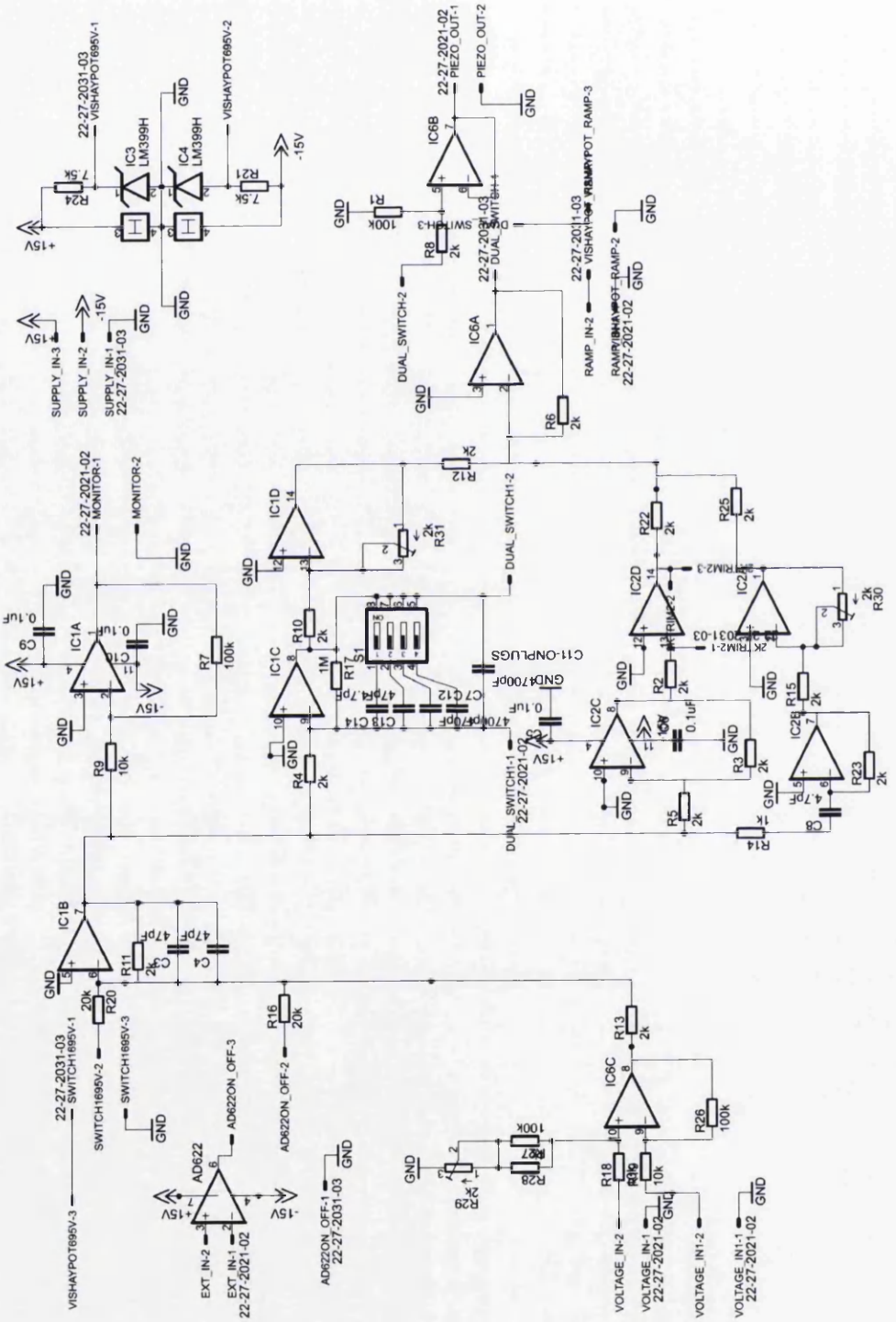

Figure A.22: Laser lock circuit.

A.3.2 Control Circuit for MOT Coils and Dispensers

Dispensers and Safety Circuit

The dispensers were controlled by a MOSFET circuit. The circuit attempts to match the voltage over a sense resistor to that provided by a computer controlled analog output by regulating the voltage flowing through a MOSFET. The dispenser (which electronically acts like a resistor,) is in series with the MOSFET and sense resistor. Two power supplies are required, a 40 mA supply (PW_IN) powers the op-amps and control circuit and a 10 A 30 V PSU running in constant voltage mode powered the dispenser (PSU_IN/OUT). A large excess voltage is required because the MOSFET needs a certain amount of voltage overhead to avoid becoming unstable, however too much overhead will cause excess heating of the MOSFET. In practise a power supply voltage of around 10 V for the dispenser, MOSFET and sense resistor was found to work well.

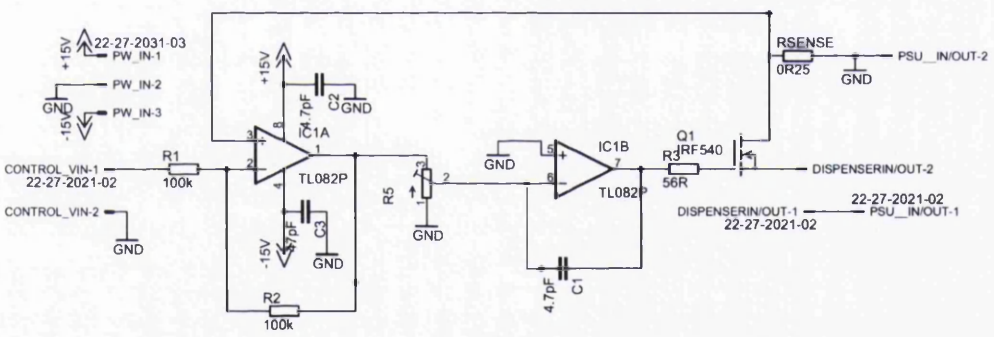

Figure A.23: Dispenser control circuit.

The circuit and PSU voltage overhead were designed to run up to 10 A, this is more than the maximum of 8 A recommended for the dispensers. The reason for the excess of power was so that a safety circuit could monitor the sense voltage for MOSFET failure. The common failure mode for this sort of MOSFET is that the source and drain will short together allowing unrestricted current to flow. If unchecked this could run the dispenser high enough to coat vacuum windows and walls with rubidium. To prevent this a safety circuit was added which monitors the sense voltage and triggers a relay to disconnect PSU_IN/OUT-1 pin on the control circuit from the power supply.

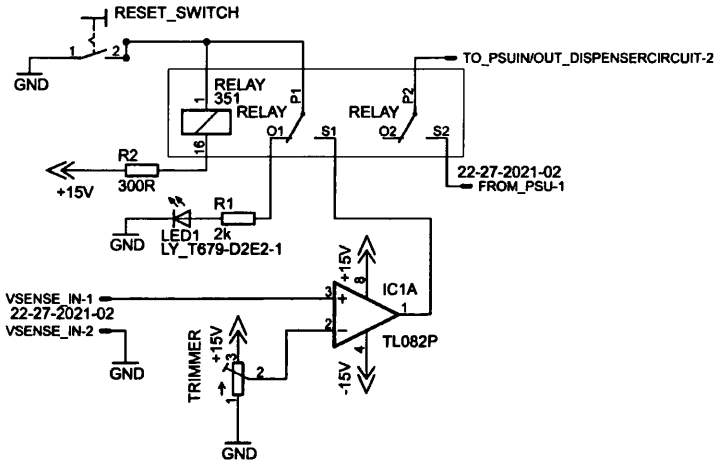

Figure A.24: Dispenser safety circuit.

When the reset momentary switch is actuated a large current flows through the relay coil causing it to actuate. This connects the PSU to the dispensers and the TL082 op-amp to the relay coil. This op-amp monitors the dispenser circuit sense voltage and compares it to a preset maximum which is set by the trimmer. As long as the preset maximum voltage is higher than the sense voltage the op-amp will continually try to drive its output to low voltage and current will flow through R2 and the relay coil. If the sense voltage increases above the preset maximum or the power to the safety circuit fails the op-amp output will not be driven low and no current will flow in the relay coil causing it to actuate and disconnect the dispenser from the PSU. If the circuit is still powered the LED will now light indicating a failure, R1 is chosen to be 2 kΩ which is low enough to allow enough current for the LED but large enough to not re-actuate the relay. The push switch is used to re-actuate the relay once the fault condition is removed.

MOT Coil Control (Injection locking experiment)

A bipolar power op-amp based circuit was used to control the MOT coils. This circuit was used instead of another MOSFET based system because it gives us the (future) ability to switch the current direction. The circuit design was adapted from reference [163]. Since the magnetic trap coils are now the MOT coils (see below) this circuit could, for example, be used to control the TOP trap coils.

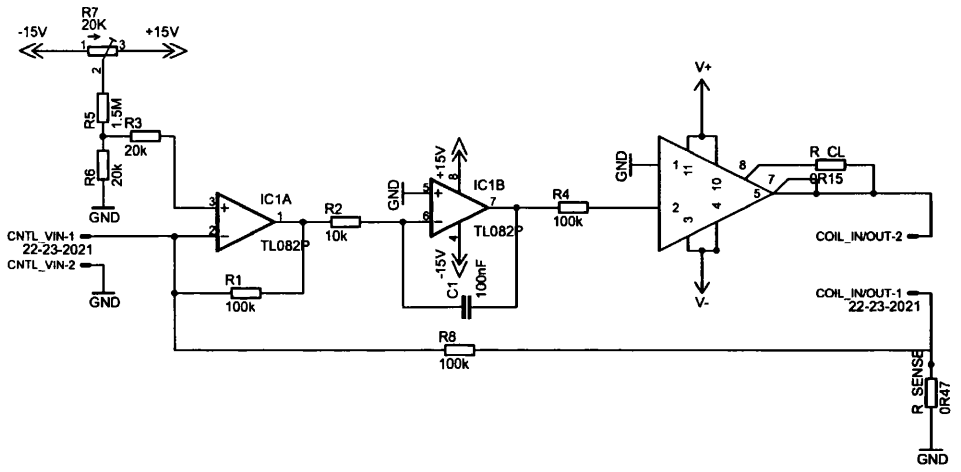

Figure A.25: MOT coils control circuit.

Power op amps such as the OPA541 used here have the disadvantage of an offset in their output, this can be tuned away with the 20 kΩ trimmer.

A.3.3 Coil Control Circuit for the Magnetic Trap

This circuit is another MOSFET-based circuit which is able to control the rapid switching of 440 A. It is similar to the dispenser control circuit described above except that the feedback signal is provided by a hall effect current sensor instead of a sense resistor. At such high currents and with high stability required the heating of the sense resistor would be intolerable. The hall effect current sensor is a Honeywell CSNS300 closed loop current sensor with a DC range of up to 600 A. It outputs a sense current which is linearly related to input current, this current is converted to a voltage by two 12 Ω resistors. Two are used to reduce heating effects from large currents.

The $\pm 15V$ supplying the op-amp and current sensor comes from a separate low current power supply to the V+ and V- which are supplied by an Agilent 6690A, 440 A, 15 V supply. Care must be taken to prevent large currents flowing to ground through the low current supply which ideally should have a common ground. To solve this ground for the low current circuit (GND) is directly connected to the earth rail and the drain pin of the MOSFET is also connected to the earth rail using the welding cable. The control voltage which comes from an analog computer control

card has a separate ground which is isolated from the rest of the circuit by IC1A which acts as an instrumentation amplifier.
A bank of 6 MOSFETs are used to control the large currents required although only one MOSFET is shown in figure A.26 for clarity. This aids the cooling of the MOSFETs since current is shared between them.

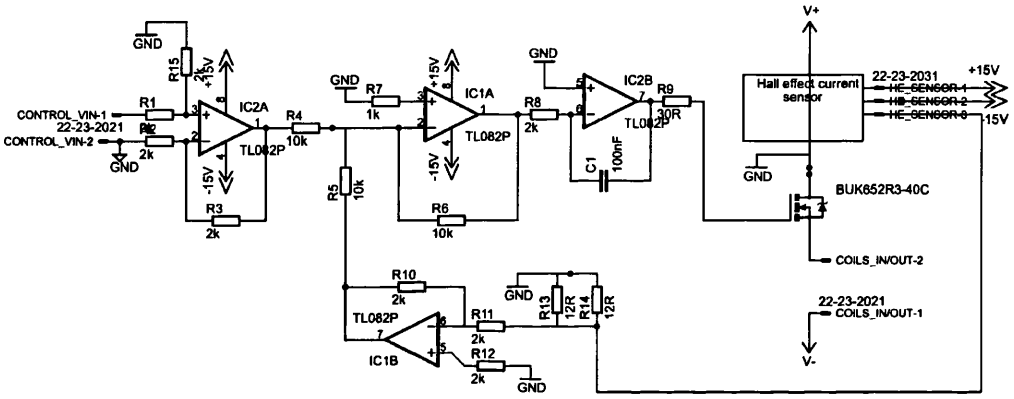

Figure A.26: Magnetic trap coil control circuit.

Eventual MOSFET Circuit

In the future it is hoped the coils will also be used to probe Feshbach resonances in addition to being the MOT and magnetic trap coils, this will require them to rapidly switch to running as Helmholtz coils which requires the current direction in one coil to be reversed. We intend to do this using a circuit from reference [157, (figure 2.8)] which is shown in figure A.27. Again each MOSFET shown in the circuit represents a bank of six MOSFETs which share the current load.
FET_1 is the MOSFET bank already constructed, it will regulate the current flow, FET_6 will act as a master switch. FET_2,3,4 and 5 act as switches to direct the current direction through coil 2 by; FET_2 and FET_5 being open and FET_3 and FET_4 being closed, or vice versa. The switching MOSFETs can be opened or closed by applying a positive or negative voltage to their gate pin.

Mounting and Cooling the MOSFETs

The MOSFETs for FET_1 were mounted on a copper bus bar shown in figure A.28 using their heatsink tab which also acts as an electrical connection to the copper

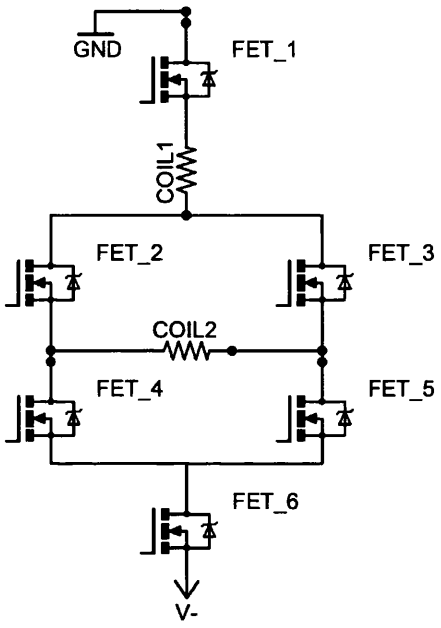

Figure A.27: Future coil MOSFET circuit. Note that GND is connected to the PSU positive output and V- connects to the negative output.

(drain pin). Two identical bars act as the source and drain, the source pins of the MOSFETs are soldered to a very short ($\sim 1 - 2$ cm,) stripped section of 13 A mains cable connected to a crimp terminal (Thomas & Betts - T2.5-4, Farnell 1208189), which is bolted to the source busbar.

The busbars are made from the same copper bar described in section A.2.2 for the connections to the square wire, the 50 mm $\times$ 10 mm profile bar is cut lengthways to make two 24 mm $\times$ 10 mm bars. A 4 mm square groove is cut along the length of the underside of the drain bar and a stripped piece of the square coil wire is used for cooling, this is attached to plumbing connections as described in section A.2.3. Thermally conductive paste is used to improve the thermal contact between the wire and bar.

The copper bars are mounted onto a 3 mm aluminium sheet as shown in figure A.30, the drain of FET_1 is earthed so this can be bolted directly onto the sheet, however the source bar is isolated using T-Global-H486R Gap filler sheet (Farnell 1372942). Although not yet constructed the mounting busbars have also been designed for the final circuit (figure A.27) and this design is shown in figure A.29. All copper parts

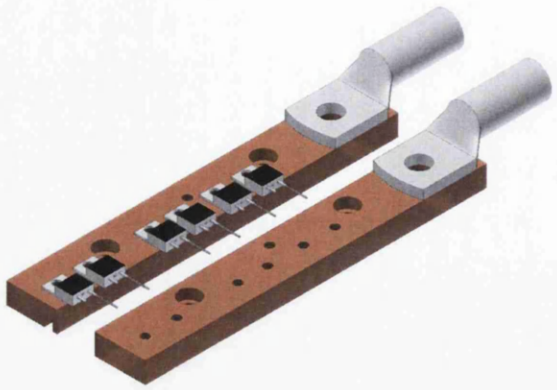

Figure A.28: MOSFET_1 source and drain busbars, note the 4 mm groove in the base of the drain busbar for cooling.

can be manufactured from the 50 mm × 10 mm profile copper bar described above, and each bar has the same 4 mm groove for cooling square wire.

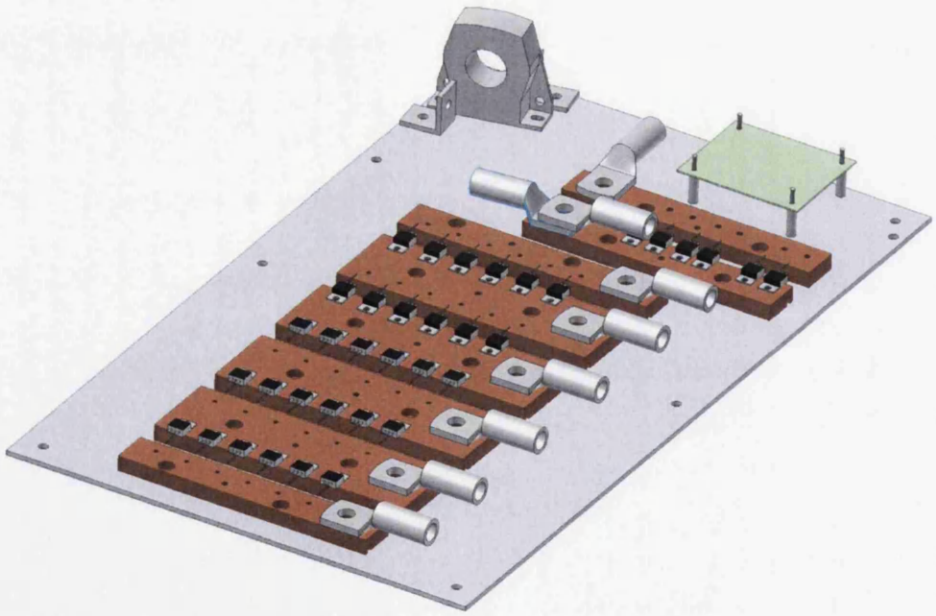

Figure A.29: Busbar design for the complete circuit shown in figure A.27.

Figure A.30: Busbar design mounted inside an enclosure.

A.4 DAVLL Stabilisation

A.4.1 Introduction

The Dichroic Atomic Vapour Laser Lock (DAVLL) was described in detail in section 3.3.2. We describe here the steps taken to try to temperature stabilise this locking mechanism

A.4.2 The Stability Problem

The DAVLL is not a Doppler free spectrometer and hence it has a sensitivity to temperature, so if used to lock a laser the laser frequency would drift with room temperature fluctuations. Immediately after construction drifts of 10 MHz per hour or more were observed. However other researchers have found temperature independent points (TIPs) at various points on the DAVLL line where temperature has no effect on the DAVLL signal [164]. Crucially they found that the TIP can be moved in frequency by rotating the QWP in the DAVLL setup. By doing so the detectors

are imbalanced, i.e. more light goes to one detector than the other and so there results a sensitivity to laser power. To use the DAVLL as a lock signal for a MOT trap laser it is crucial that a TIP occurs at the lock frequency, in the case of a ^{87}Rb MOT this is around 20 MHz to the red of the $F = 2$ to $F' = 3$ transition of the D2 line.

Fixing the problem

The QWP was varied over different angles, and at each point the DAVLL trace was recorded when the cell temperature was approximately 20 C and 24 C. The cell was heated using a desk lamp and temperature monitored with a thermocouple placed on the side of the cell and covered in heat paste. The cell was heated very slowly (over an hour or more) to minimise stress to the glass. During this time the length of the piezo (laser frequency) sweep was not adjusted.

The spectra obtained at two temperatures were overlaid as shown in figure A.31. The line crossing points occur at the TIP. Small saturation peaks can be seen in these traces from backscatter of the cell windows, these were deliberately left to provide some frequency reference so that the desired lock point could be seen easily and also so that the x-axis (frequency axis) of the two traces could be shifted slightly to account for frequency changes in between the two traces. Three saturation peaks can be seen, the desired lock point is just to the left of the middle saturation peak. The waveplate was varied iteratively until the TIP was close to the lock point. There is only one TIP on the DAVLL slope and so the DAVLL cell will need to be temperature stabilised so that the DAVLL can be used to tune to other frequencies required to optimise the magnetic trap. A long term beat of the reference Vs DAVLL-locked trap laser was then recorded using the heterodyne beat detector and frequency counter. Over approximately 10000 seconds (just under 3 hours,) the two lasers remained within 1 MHz of each other as shown in figure A.32.

Unfortunately more recent data taken of the long term beat between the reference and trap lasers has shown an apparent reduction in stability. Whilst still an order of magnitude better than the 10 MHz per hour drifts which occurred before stabilisation work, drifts of some MHz during a day are not uncommon.

Recently a significant temperature dependence was discovered in our multi order waveplates which was improved by replacing with a single order waveplate, we observed no temperature dependence in our dielectric polarising beam splitter cubes,

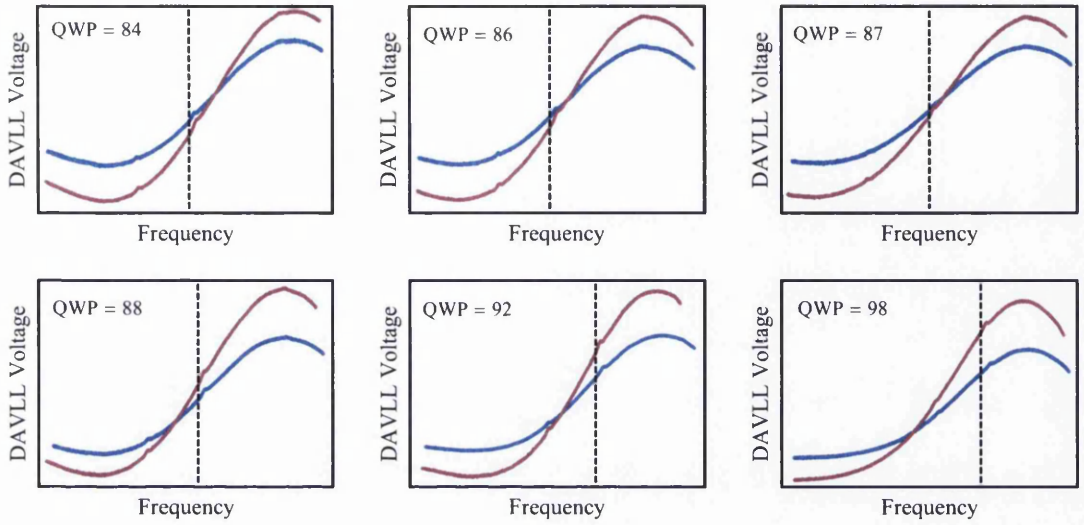

Figure A.31: DAVLL traces with a hot (red) and cold (blue) cell. To the nearest degree of the QWP, an angle of 87 degrees on the QWP mount was found to be the closest the TIP comes to the lock point. The dashed line indicates the lock point for the MOT.

this is in contrast to reference [152] who found some temperature dependence in dielectric beam splitters but obtained very stable locks even with a plastic QWP. Work on improving the DAVLL stability is continuing.

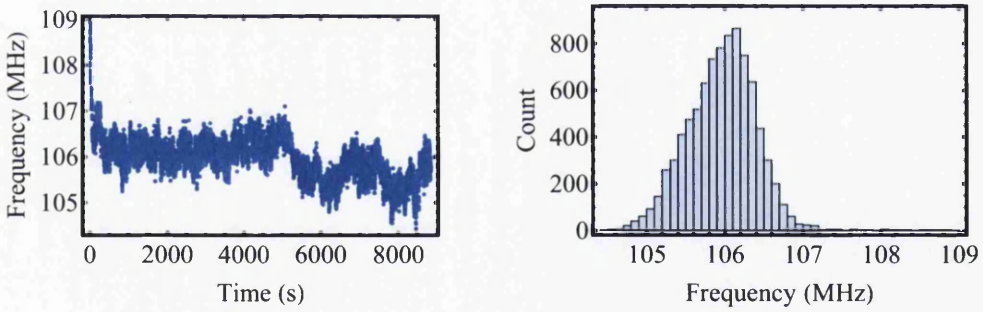

Figure A.32: Trap laser and reference laser beat frequency with a histogram of the frequency data.

Bibliography

[1] M. Bennett, M. F. Schatz, H. Rockwood, and K. Wiesenfeld. Huygens's clocks. *Proceedings of the Royal Society of London. Series A: Mathematical, Physical and Engineering Sciences*, 458:563, 2002.

[2] G.L. Beers. A frequency-dividing locked-in oscillator frequency-modulation receiver. *Proceedings of the IRE*, 32:730, 1944.

[3] D.G. Tucker. Forced oscillations in oscillator circuits, and the synchronization of oscillators. *Electrical Engineers - Part III: Radio and Communication Engineering, Journal of the Institution of*, 92:226, 1945.

[4] R. Adler. A study of locking phenomena in oscillators. *Proceedings of the IEEE*, 61:1236, 1973.

[5] A. Einstein. Strahlungs - emission and - absorption nach der quantentheorie. *Verhandlungen der Deutschen Physikalischen Gesellschaft*, XVIII:318, 1916.

[6] J. P. Gordon, H. J. Zeiger, and C. H. Townes. The maser—new type of microwave amplifier, frequency standard, and spectrometer. *Phys. Rev.*, 99:1264, 1955.

[7] A. L. Schawlow and C. H. Townes. Infrared and optical Masers. *Phys. Rev.*, 112:1940, 1958.

[8] T. H. Maiman. Stimulated optical radiation in ruby. *Nature*, 187:493, 1960.

[9] C. H. Townes. *How the laser happened.* Oxford University Press, 2002.

[10] P. P. Sorokin and M. J. Stevenson. Stimulated infrared emission from trivalent uranium. *Phys. Rev. Lett.*, 5:557, 1960.

[11] R. N. Hall, G. E. Fenner, J. D. Kingsley, T. J. Soltys, and R. O. Carlson. Coherent light emission from gaas junctions. *Phys. Rev. Lett.*, 9:366, 1962.

[12] I. Hayashi, M. B. Panish, P. W. Foy, and S. Sumski. Junction lasers which operate continuosly at room temperature. *Applied Physics Letters*, 17:109, 1970.

[13] H. L. Stover and W. H. Steier. Locking of laser oscillators by light injection. *Applied Physics Letters*, 8:91, 1966.

[14] A. E. Siegman. *Lasers.* University Science Books, 1986.

[15] R. Lang and K. Kobayashi. External optical feedback effects on semiconductor injection laser properties. *IEEE Journal of Quantum Electronics*, 16:347, 1980.

[16] F. T. Arecchi, R. Meucci, G. Puccioni, and J. Tredicce. Experimental evidence of sub-harmonic bifurcations, multistability, and turbulence in a q-switched gas laser. *Phys. Rev. Lett.*, 49:1217, 1982.

[17] J. Nishizawa and K. Ishida. Injection-induced modulation of laser light by the interaction of laser diodes. *Quantum Electronics, IEEE Journal of*, 11:515, 1975.

[18] P. Bhansali and J. Roychowdhury. Injection locking analysis and simulation of weakly coupled oscillator networks. In P. Li, L. M. Silveira, and P. Feldmann, editors, *Simulation and Verification of Electronic and Biological Systems*, page 71. Springer Netherlands, 2011.

[19] K. Otsuka and S. Tarucha. Theoretical studies on injection locking and injection-induced modulation of laser diodes. *Quantum Electronics, IEEE Journal of*, 17:1515, 1981.

[20] T. B. Simpson, J. M. Liu, A. Gavrielides, and P. M. Alsing. Period doubling route to chaos in a semiconductor laser subject to optical injection. *Applied Physics Letters*, 64:3539, 1994.

[21] T.B. Simpson, J.M. Liu, K.F. Huang, and K. Tai. Nonlinear dynamics induced by external optical injection in semiconductor lasers. *Quantum Semicl. Opt.*, 9:765, 1997.

[22] S. Wieczorek, B. Krauskopf, T.B. Simpson, and D. Lenstra. The dynamical complexity of optically injected semiconductor lasers. *Physics Reports*, 416:1, 2005.

[23] S. J. Eriksson and A. M. Lindberg. Observations on the dynamics of semiconductor laser subjected to external optical injection. *J. Opt. B: Quantum Semiclass.*, 4:149, 2002.

[24] S. Wieczorek, T. B. Simpson, B. Krauskopf, and D. Lenstra. Bifurcation transitions in an optically injected diode laser: theory and experiment. *Optics Communications*, 215:125, 2003.

[25] T. B. Simpson. Mapping the nonlinear dynamics of a distributed feedback semiconductor laser subject to external optical injection. *Optics Communications*, 215:135, 2003.

[26] R. Rajarshi. Communications technology: Chaos down the line. *Nature*, 438:298, 2005.

[27] R. Roy and K. S. Thornburg. Experimental synchronization of chaotic lasers. *Phys. Rev. Lett.*, 72:2009, 1994.

[28] T. Sugawara, M. Tachikawa, T. Tsukamoto, and T. Shimizu. Observation of synchronization in laser chaos. *Phys. Rev. Lett.*, 72:3502, 1994.

[29] S.-C. Chan, R. Diaz, and J.-M. Liu. Novel photonic applications of nonlinear semiconductor laser dynamics. *Optical and Quantum Electronics*, 40:83, 2008.

[30] C. I. Laidler and S. Eriksson. Microwave sidebands for atomic physics experiments by period one oscillation in optically injected diode lasers. *EPL.*, 96(53001), 2011.

[31] T.W. Hänsch and A.L. Schawlow. Cooling of gases by laser radiation. *Optics Communications*, 13:68, 1975.

[32] D. Wineland and H. Dehmelt. Proposed $10^{14}\delta\nu < \nu$ laser fluorescence spectroscopy on $t1^{+}$ mono-ion oscillator iii. *Bulletin of the American Physical Society*, 20:637, 1975.

[33] D. J. Wineland, R. E. Drullinger, and F. L. Walls. Radiation-pressure cooling of bound resonant absorbers. *Phys. Rev. Lett.*, 40:1639, 1978.

[34] W. Neuhauser, M. Hohenstatt, P. Toschek, and H. Dehmelt. Optical-sideband cooling of visible atom cloud confined in parabolic well. *Phys. Rev. Lett.*, 41:233, 1978.

[35] A. Ashkin. Trapping of atoms by resonance radiation pressure. *Phys. Rev. Lett.*, 40:729–732, 1978.

[36] S. V. Andreev, V. I. Balykin, V. S. Letokhov, and V. G. Minogin. Radiative slowing and reduction of the energy spread of a beam of sodium atoms to 1.5 K in a oppositely directed laser beam. *JETP Lett*, 34:442, 1981.

[37] W. D. Phillips and H. Metcalf. Laser deceleration of an atomic beam. *Phys. Rev. Lett.*, 48:596, 1982.

[38] J. Prodan, A. Migdall, W. D. Phillips, I. So, H. Metcalf, and J. Dalibard. Stopping atoms with laser light. *Phys. Rev. Lett.*, 54:992, 1985.

[39] Steven Chu, L. Hollberg, J. E. Bjorkholm, Alex Cable, and A. Ashkin. Three-dimensional viscous confinement and cooling of atoms by resonance radiation pressure. *Phys. Rev. Lett.*, 55:48, 1985.

[40] A. L. Migdall, J. V. Prodan, W. D. Phillips, T. H. Bergeman, and Harold J. Metcalf. First observation of magnetically trapped neutral atoms. *Phys. Rev. Lett.*, 54:2596, 1985.

[41] S. Chu, J. E. Bjorkholm, A. Ashkin, and A. Cable. Experimental observation of optically trapped atoms. *Phys. Rev. Lett.*, 57:314, 1986.

[42] C. J. Foot. *Atomic Physics.* Oxford University Press, 2005.

[43] E. L. Raab, M. Prentiss, A. Cable, S. Chu, and D. E. Pritchard. Trapping of neutral sodium atoms with radiation pressure. *Phys. Rev. Lett.*, 59:2631, 1987.

[44] C. Monroe, W. Swann, H. Robinson, and C. Wieman. Very cold trapped atoms in a vapor cell. *Phys. Rev. Lett.*, 65:1571, 1990.

[45] K. E. Gibble, S. Kasapi, and S. Chu. Improved magneto-optic trapping in a vapor cell. *Opt. Lett.*, 17:526, 1992.

[46] P. D. Lett, R. N. Watts, C. I. Westbrook, W. D. Phillips, P. L. Gould, and H. J. Metcalf. Observation of atoms laser cooled below the Doppler limit. *Phys. Rev. Lett.*, 61:169, 1988.

[47] J. P. Gordon and A. Ashkin. Motion of atoms in a radiation trap. *Phys. Rev. A*, 21:1606, 1980.

[48] R. J. Cook. Theory of resonance-radiation pressure. *Phys. Rev. A*, 22:1078, Sep 1980.

[49] D. J. Wineland and Wayne M. Itano. Laser cooling of atoms. *Phys. Rev. A*, 20:1521, 1979.

[50] J. Dalibard and C. Cohen-Tannoudji. Laser cooling below the Doppler limit by polarization gradients: simple theoretical models. *J. Opt. Soc. Am. B*, 6:2023, 1989.

[51] S. Salomon, J. Dalibard, W. D. Phillips, A. Clairon, and S. Guellati. Laser cooling of cesium atoms below 3 microkelvin. *EPL*, 12:683, 1990.

[52] D. Boiron, A. Michaud, P. Lemonde, Y. Castin, C. Salomon, S. Weyers, K. Szymaniec, L. Cognet, and A. Clairon. Laser cooling of cesium atoms in gray optical molasses down to 1.1μk. *Phys. Rev. A*, 53:R3734, 1996.

[53] M. H. Anderson, J. R. Ensher, M. R. Matthews, C. E. Wieman, and E. A. Cornell. Observation of Bose-Einstein condensation in a dilute atomic vapor. *Science*, 269:198, 1995.

[54] C. C. Bradley, C. A. Sackett, J. J. Tollett, and R. G. Hulet. Evidence of Bose-Einstein condensation in an atomic gas with attractive interactions. *Phys. Rev. Lett.*, 75:1687, 1995.

[55] K. B. Davis, M. O. Mewes, M. R. Andrews, N. J. van Druten, D. S. Durfee, D. M. Kurn, and W. Ketterle. Bose-Einstein condensation in a gas of sodium atoms. *Phys. Rev. Lett.*, 75:3969, 1995.

[56] A. Einstein. Quantum theory of the monoatomic ideal gas. http://www.condmat.uni-oldenburg.de/teachingsp/sp.html. *S. B. preuss. Akad. Wiss*, 22:261, 1924.

[57] Wolfgang Petrich, Michael H. Anderson, Jason R. Ensher, and Eric A. Cornell. Behavior of atoms in a compressed magneto-optical trap. *J. Opt. Soc. Am. B*, 11:1332, 1994.

[58] W. Petrich, M. H. Anderson, J. R. Ensher, and E. A. Cornell. Stable, tightly confining magnetic trap for evaporative cooling of neutral atoms. *Phys. Rev. Lett.*, 74:3352, 1995.

[59] J. J. Tollett, C. C. Bradley, C. A. Sackett, and R. G. Hulet. Permanent magnet trap for cold atoms. *Phys. Rev. A*, 51:R22, 1995.

[60] M. R. Andrews, C. G. Townsend, H.-J. Miesner, D. S. Durfee, D. M. Kurn, and W. Ketterle. Observation of interference between two Bose condensates. *Science*, 275:637, 1997.

[61] M.-O. Mewes, M. R. Andrews, D. M. Kurn, D. S. Durfee, C. G. Townsend, and W. Ketterle. Output coupler for Bose-Einstein condensed atoms. *Phys. Rev. Lett.*, 78:582, 1997.

[62] J. Fortagh, A. Grossmann, C. Zimmermann, and T. W. Hänsch. Miniaturized wire trap for neutral atoms. *Phys. Rev. Lett.*, 81:5310, 1998.

[63] J. Denschlag, D. Cassettari, A. Chenet, S. Schneider, and J. Schmiedmayer. A neutral atom and a wire: towards mesoscopic atom optics. *Applied Physics B: Lasers and Optics*, 69:291, 1999.

[64] E. A. Hinds, M. G. Boshier, and I. G. Hughes. Magnetic waveguide for trapping cold atom gases in two dimensions. *Phys. Rev. Lett.*, 80:645, 1998.

[65] H. Ott, J. Fortagh, G. Schlotterbeck, A. Grossmann, and C. Zimmermann. Bose-Einstein condensation in a surface microtrap. *Phys. Rev. Lett.*, 87:230401, 2001.

[66] W. Hansel, P. Hommelhoff, T.W. Hänsch, and J. Reichel. Bose-Einstein condensation on a microelectronic chip. *Nature*, 413:498, 2001.

[67] S. Du, M.B. Squires, L. Czaia, D.Z. Anderson, R.A. Saravanan, V.M. Bright, Y. Imai, J. Reichel, and T.W. Hänsch. Atom chip Bose-Einstein condensation in a portable vacuum cell. In *Quantum Electronics Conference, 2004. (IQEC). International*, page 1130, 2004.

[68] D. Cassettari, B. Hessmo, R. Folman, T. Maier, and J. Schmiedmayer. Beam splitter for guided atoms. *Phys. Rev. Lett.*, 85:5483, 2000.

[69] J. R. Abo-Shaeer, C. Raman, J. M. Vogels, and W. Ketterle. Observation of vortex lattices in Bose-Einstein condensates. *Science*, 292:476, 2001.

[70] C. Chin, R. Grimm, P. Julienne, and E. Tiesinga. Feshbach resonances in ultracold gases. *Rev. Mod. Phys.*, 82:1225, 2010.

[71] E.A. Donley, N. R. Claussen, S. T. Thompson, and C. E. Wiemann. Atom-molecule coherence in a BoseEinstein condensate. *Nature*, 417:529, 2002.

[72] R. Wynar, R. S. Freeland, D. J. Han, C. Ryu, and D. J. Heinzen. Molecules in a Bose-Einstein condensate. *Science*, 287:1016, 2000.

[73] B. DeMarco and D. S. Jin. Onset of Fermi degeneracy in a trapped atomic gas. *Science*, 285:1703, 1999.

[74] M. W. Zwierlein, C. A. Stan, C. H. Schunck, S. M. F. Raupach, S. Gupta, Z. Hadzibabic, and W. Ketterle. Observation of Bose-Einstein condensation of molecules. *Phys. Rev. Lett.*, 91:250401, 2003.

[75] M. Goreiner, C. A. Regal, and D. S. Jin. Emergence of a molecular BoseEinstein condensate from a Fermi gas. *Nature*, 426:537, 2003.

[76] S. Jochim, M. Bartenstein, A. Altmeyer, G. Hendl, S. Riedl, C. Chin, J. Hecker Denschlag, and R. Grimm. Bose-Einstein condensation of molecules. *Science*, 302:2101, 2003.

[77] G. Grynberg, B. Lounis, P. Verkerk, J.-Y. Courtois, and C. Salomon. Quantized motion of cold cesium atoms in two- and three-dimensional optical potentials. *Phys. Rev. Lett.*, 70:2249, 1993.

[78] A. Hemmerich, C. Zimmermann, and T.W. Hänsch. Sub-khz rayleigh resonance in a cubic atomic crystal. *Europhysics Letters*, 22:89, 1993.

[79] B. P. Anderson and M. A. Kasevich. Macroscopic quantum interference from atomic tunnel arrays. *Science*, 282:1686, 1998.

[80] A. Kastberg, W. D. Phillips, S. L. Rolston, R. J. C. Spreeuw, and P. S. Jessen. Adiabatic cooling of cesium to 700 nk in an optical lattice. *Phys. Rev. Lett.*, 74:1542, 1995.

[81] K. Günter, T. Stöferle, H. Moritz, M. Köhl, and T. Esslinger. Bose-Fermi mixtures in a three-dimensional optical lattice. *Phys. Rev. Lett.*, 96:180402, 2006.

[82] S. Dürr, T. Volz, A. Marte, and G. Rempe. Observation of molecules produced from a Bose-Einstein condensate. *Phys. Rev. Lett.*, 92:020406, 2004.

[83] J. P. Gaebler, J. T. Stewart, J. L. Bohn, and D. S. Jin. p-wave Feshbach molecules. *Phys. Rev. Lett.*, 98:200403, 2007.

[84] S. B. Papp and C. E. Wieman. Observation of heteronuclear Feshbach molecules from a ^{85}Rb$^{\smile}$^{87}Rb gas. *Phys. Rev. Lett.*, 97:180404, 2006.

[85] C. Ospelkaus, S. Ospelkaus, L. Humbert, P. Ernst, K. Sengstock, and K. Bongs. Ultracold heteronuclear molecules in a 3D optical lattice. *Phys. Rev. Lett.*, 97:120402, 2006.

[86] A.-C. Voigt, M. Taglieber, L. Costa, T. Aoki, W. Wieser, T. W. Hänsch, and K. Dieckmann. Ultracold heteronuclear Fermi-Fermi molecules. *Phys. Rev. Lett.*, 102:020405, 2009.

[87] D. DeMille. Quantum computation with trapped polar molecules. *Phys. Rev. Lett.*, 88:067901, 2002.

[88] X.-H. Bao, A. Reingruber, P. Dietrich, J. Rui, A. Dueck, T. Strassel, L. Li, N.-L. Liu, B. Zhao, and J.-W. Pan. Efficient and long-lived quantum memory with cold atoms inside a ring cavity. *Nature Physics*, 8:517, 2012.

[89] H. P. Specht, C. Nolleke, A. Reiserer, M. Uphoff, E. Figueroa, S. Ritter, and G. Rempe. A single-atom quantum memory. *Nature*, 473:190, 2011.

[90] Y. J Lin, K. Jimenez-Garcia, and I. B. Spielman. Spin-orbit-coupled BoseEinstein condensates. *Nature*, 471:83, 2011.

[91] L. W. Cheuk, A. T. Sommer, Z. Hadzibabic, T. Yefsah, W. S. Bakr, and M. W. Zwierlein. Spin-injection spectroscopy of a spin-orbit coupled Fermi gas. *Phys. Rev. Lett.*, 109:095302, 2012.

[92] J. M. Amini, H. Uys, J. H. Wesenberg, S. Seidelin, J. Britton, J. J. Bollinger, D. Leibfried, C. Ospelkaus, A. P. VanDevender, and D. J. Wineland. Toward scalable ion traps for quantum information processing. *New Journal of physics*, 12:03,3031, 2010.

[93] A. Rauschenbeutel, G. Nogues, S. Osnaghi, P. Bertet, M. Brune, J.M. Raimond, and S. Haroche. Coherent operation of a tunable quantum phase gate in cavity QED. *Physical Review Letters*, 83:5166, 1999.

[94] K. Maeda, G. Baym, and T. Hatsuda. Simulating dense QCD matter with ultracold atomic Boson-Fermion mixtures. *Phys. Rev. Lett.*, 103:085301, 2009.

[95] D. Sesko, C. G. Fan, and C. E. Wieman. Production of a cold atomic vapor using diode-laser cooling. *J. Opt. Soc. Am. B*, 5:1225, 1988.

[96] S. Panda. *Microelectronics and Optoelectronics technology.* University Science Press, 2009.

[97] C.H. Henry. Theory of the linewidth of semiconductor lasers. *Quantum Electronics*, 18:259, 1982.

[98] S. A. Anson, J. T. Olesberg, Michael E. Flatte, T. C. Hasenberg, and Thomas F. Boggess. Differential gain, differential index, and linewidth enhancement factor for a 4 μm superlattice laser active layer. *Journal of Applied Physics*, 86:713, 1999.

[99] T. B. Simpson and J. M. Liu. Phase and amplitude characteristics of nearly degenerate four-wave mixing in Fabry-Perot semiconductor lasers. *Journal of Applied Physics*, 73:2587, 1993.

[100] S.-C. Chan, S.-K. Hwang, and J.-M. Liu. Period-one oscillation for photonic microwave transmission using an optically injected semiconductor laser. *Opt. Express*, 15:14921, 2007.

[101] S.-C. Chan and J.-M. Liu. Frequency modulation on single sideband using controlled dynamics of an optically injected semiconductor laser. *Quantum Electronics, IEEE Journal of*, 42:699, 2006.

[102] S.-C. Chan. Analysis of an optically injected semiconductor laser for microwave generation. *Quantum Electronics, IEEE Journal of*, 46:421, 2010.

[103] F. Mogensen, H. Olesen, and G. Jacobsen. FM noise suppression and linewidth reduction in an injection-locked semiconductor laser. *Electronics Letters*, 21:696, 1985.

[104] T.B. Simpson, J.M. Liu, and A. Gavrielides. Bandwidth enhancement and broadband noise reduction in injection-locked semiconductor lasers. *Photonics Technology Letters, IEEE*, 7:709, 1995.

[105] J. Wang, M.K. Haldar, L. Li, and F.V.C. Mendis. Enhancement of modulation bandwidth of laser diodes by injection locking. *Photonics Technology Letters, IEEE*, 8:34, 1996.

[106] S. Piazzolla, P. Spano, and M. Tamburrini. Small signal analysis of frequency chirping in injection-locked semiconductor lasers. *Quantum Electronics*, 22:2219, 1986.

[107] R. B. M. Clarke, E. Riis, G. P. Barwood, P Gill, G Huang, and H. A. Klein. A sideband-injection locked extended cavity diode laser for interrogating cold trapped strontium ions. *Optics Communications*, 158:36, 1998.

[108] U. Schnemann, H. Engler, M. Zielonkowski, M. Weidemller, and R. Grimm. Magneto-optic trapping of lithium using semiconductor lasers. *Optics Communications*, 158:263, 1998.

[109] N. Kishi, M. Aga, and E. Yamashita. Microwave generation using laser heterodyne technique with independent controllability in frequency and phase. *Microwave Theory and Techniques, IEEE Transactions on*, 43:2284, 1995.

[110] A.J. Seeds, I.D. Blanchflower, N.J. Gomes, G. King, and S.J. Flynn. New developments in optical control techniques for phased array radar. In *Microwave Symposium Digest, 1988., IEEE MTT-S International*, page 905 vol.2, 1988.

[111] L.A. Johansson and A.J. Seeds. Generation and transmission of millimeter-wave data-modulated optical signals using an optical injection phase-lock loop. *Lightwave Technology, Journal of*, 21:511, 2003.

[112] S. Pajarola, G. Guekos, P. Nizzola, and H. Kawaguchi. Dual-polarization external-cavity diode laser transmitter for fiber-optic antenna remote feeding. *Microwave Theory and Techniques, IEEE Transactions on*, 47:1234, 1999.

[113] C. J. Myatt, N. R. Newbury, and C. E. Wieman. Simplified atom trap by using direct microwave modulation of a diode laser. *Opt. Lett.*, 18:649, 1993.

[114] J. Goldwin, S. B. Papp, B. DeMarco, and D. S. Jin. Two-species magneto-optical trap with ^{40}K and ^{87}Rb. *Phys. Rev. A*, 65:021402, 2002.

[115] M. Vangeleyn, P. F. Griffin, E. Riis, and A. S. Arnold. Single-laser, one beam, tetrahedral magneto-optical trap. *Opt. Express*, 17:13601, 2009.

[116] M. Vangeleyn, P. F. Griffin, E. Riis, and A. S. Arnold. Laser cooling with a single laser beam and a planar diffractor. *Opt. Lett.*, 35:3453, 2010.

[117] R. Kowalski, S. Root, S. D. Gensemer, and P. L. Gould. A frequency-modulated injection-locked diode laser for two-frequency generation. *Review of Scientific Instruments*, 72:2532, 2001.

[118] H. S. Moon, J. B. Kim, J. D. Park, B. K. Kwon, H. Cho, and H. S. Lee. Magneto-optic trap of Rb atoms with an injection-seeded laser that operates at two frequencies. *Appl. Opt.*, 35:5402, 1996.

[119] M. Bondiou, R. Gabet, G. M. Stéphan, and P. Besnard. Linewidth of an optically injected semiconductor laser. *Journal of Optics B: Quantum and Semiclassical Optics*, 2:41, 2000.

[120] D. Welford and A. Mooradian. Output power and temperature dependence of the linewidth of single? frequency cw (GaAl)As diode lasers. *App. Phys. Lett.*, 40:865, 1982.

[121] J. Fortagh, A. Grossmann, T. W. Hänsch, and C. Zimmermann. Fast loading of a magneto-optical trap from a pulsed thermal source. *Journal of Applied Physics*, 84:6499, 1998.

[122] U. D. Rapol, A. Wasan, and V. Natarajan. Loading of a Rb magneto-optic trap from a getter source. *Phys. Rev. A*, 64:023402, 2001.

[123] Jun Ye, Steve Swartz, Peter Jungner, and John L. Hall. Hyperfine structure and absolute frequency of the $^{87}rb\ 5p_{\frac{3}{2}}^{3}$ state. *Opt. Lett.*, 21(16):1280, 1996.

[124] S. Bize, Y. Sortais, M. S. Santos, C. Mandache, A. Clairon, and C. Salomon. High-accuracy measurement of the ^{87}rb ground-state hyperfine splitting in an atomic fountain. *Europhysics Letters*, 45(5):558, 1999.

[125] A. S. Arnold, J. S. Wilson, and M. G. Boshier. A simple extended-cavity diode laser. *Review of Scientific Instruments*, 69:1236, 1998.

[126] M. G. Littman and H. J. Metcalf. Spectrally narrow pulsed dye laser without beam expander. *Appl. Opt.*, 17:2224, 1978.

[127] C. Wieman and T. W. Hänsch. Doppler-free laser polarization spectroscopy. *Phys. Rev. Lett.*, 36:1170, 1976.

[128] C. P. Pearman, C. S. Adams, S. G. Cox, P.F.Griffin, D. A. Smith, and I. G. Hughes. Polarization spectroscopy of a closed atomic transition: applications to laser frequency locking. *J. Phys B: At. Mol. Opt. Phys.*, 35:5141, 2002.

[129] M. L. Harris, C. S. Adams, S. L. Cornish, I. C. McLeod, E. Tarleton, and I. G. Hughes. Polarization spectroscopy in rubidium and cesium. *Phys. Rev. A*, 73:062509, 2006.

[130] K.E. Chlouverakis, K.M. Al-Aswad, I.D. Henning, and M.J. Adams. Determining laser linewidth parameter from Hopf bifurcation minimum in lasers subject to optical injection. *Electronics Letters*, 39:1185, 2003.

[131] T. Stover, A. N. Steier, and R. P. Kovacich. Laser offset-frequency locking using a frequency-to-voltage converter. *Measurement Science and Technology*, 9:1635, 1998.

[132] U. Schunemann, H. Engler, R. Grimm, M. Weidemuller, and M. Zielonkowski. Simple scheme for tunable frequency offset locking of two lasers. *Review of Scientific Instruments*, 70:242, 1999.

[133] G. Ritt, G. Cennini, C. Geckeler, and M. Weitz. Laser frequency offset locking using a side of filter technique. *Applied Physics B: Lasers and Optics*, 79:363, 2004.

[134] M. Trupke, F. Ramirez-Martinez, E. A. Curtis, J. P. Ashmore, S. Eriksson, E. A. Hinds, Z. Moktadir, C. Gollasch, M. Kraft, G. Vijaya Prakash, and J. J. Baumberg. Pyramidal micromirrors for microsystems and atom chips. *Applied Physics Letters*, 88:071116, 2006.

[135] A. L. Marchant, S. Händel, T. P. Wiles, S. A. Hopkins, C. S. Adams, and S. L. Cornish. Off-resonance laser frequency stabilization using the Faraday effect. *Opt. Lett.*, 36:64, 2011.

[136] S.-C. Chan, S.-K. Hwang, and J.-M. Liu. Radio-over-fiber AM-to-FM upconversion using an optically injected semiconductor laser. *Opt. Lett.*, 31:2254, 2006.

[137] M. Kasevich and S. Chu. Laser cooling below a photon recoil with three-level atoms. *Phys. Rev. Lett.*, 69:1741, 1992.

[138] S.-C. Chan and J.-M. Liu. Tunable narrow-linewidth photonic microwave generation using semiconductor laser dynamics. *Selected Topics in Quantum Electronics, IEEE Journal of*, 10:1025, 2004.

[139] S. Ospelkaus, A. Pe'er, K. K. Ni, J. J. Zirbel, B. Neyenhuis, S. Kotochigova, P. S. Julienne, J. Ye, and D. S. Jin. Efficient state transfer in an ultracold dense gas of heteronuclear molecules. *Nature Physics*, 4:622, 2008.

[140] T. E. Wall, J. F. Kanem, J. J. Hudson, B. E. Sauer, D. Cho, M. G. Boshier, E. A. Hinds, and M. R. Tarbutt. Lifetime of the $a(v' = 0)$ state and Franck-Condon factor of the a-x(0-0) transition of caf measured by the saturation of laser-induced fluorescence. *Phys. Rev. A*, 78:062509, 2008.

[141] Á. Rapp, G. Zaránd, C. Honerkamp, and W. Hofstetter. Color superfluidity and "baryon" formation in ultracold Fermions. *Phys. Rev. Lett.*, 98:160405, 2007.

[142] K. P. Nayak and K. Hakuta. Single atoms on an optical nanofibre. *New Journal of physics*, 10:053003, 2008.

[143] G. Breit and I. I. Rabi. Measurement of nuclear spin. *Phys. Rev.*, 38:2082, 1931.

[144] C. J. Pethick and H. Smith. *Bose-Einstein Condensation in Dilute Gases.* Cambridge University Press, 2nd edition, 2008.

[145] P. Tierney. *Magnetic Trapping of an Ultracold $^{87}Rb - ^{133}Cs$ Atomic Mixture.* PhD thesis, Durham University, 2009.

[146] E. Gross. Structure of a quantized vortex in boson systems. *Il Nuovo Cimento (1955-1965)*, 20:454, 1961.

[147] L. P. Pitaevskii. Vortex lines in an imperfect Bose gas. *Soviet Physics JETP-USSR*, 13:451, 1961.

[148] M. Arndt, M. Ben Dahan, D. Guéry-Odelin, M. W. Reynolds, and J. Dalibard. Observation of a zero-energy resonance in Cs-Cs collisions. *Phys. Rev. Lett.*, 79:625–628, 1997.

[149] R. L. D. Campbell, R. P. Smith, N. Tammuz, S. Beattie, S. Moulder, and Z. Hadzibabic. Efficient production of large ^{39}K Bose-Einstein condensates. *Phys. Rev. A*, 82:063611, 2010.

[150] A. Ludewig. *Feshbach resonances in ^{40}K.* PhD thesis, University of Amsterdam, 2012.

[151] A. Marte, T. Volz, J. Schuster, S. Dürr, G. Rempe, E. G. M. van Kempen, and B. J. Verhaar. Feshbach resonances in rubidium 87: Precision measurement and analysis. *Phys. Rev. Lett.*, 89:283202, 2002.

[152] K. L. Corwin, Z.-T. Lu, C. F. Hand, R. J. Epstein, and C. E. Wieman. Frequency-stabilized diode laser with the zeeman shift in an atomic vapor. *Appl. Opt.*, 37:3295, 1998.

[153] A. Millett-Sikking, I.G. Hughes, P. Tierney, and S.L. Cornish. DAVLL lineshapes in atomic rubidium. *J. Phys. B*, 40:187, 2007.

[154] R. Wang, M. Liu, F. Minardi, and M. Kasevich. Reaching ^{7}Li quantum degeneracy with a minitrap. *Phys. Rev. A*, 75:013610, 2007.

[155] J. E. Bjorkholm. Collision-limited lifetimes of atom traps. *Phys. Rev. A*, 38:1599, Aug 1988.

[156] S. M. Spillane, G. S. Pati, K. Salit, M. Hall, P. Kumar, R. G. Beausoleil, and M. S. Shahriar. Observation of nonlinear optical interactions of ultralow levels of light in a tapered optical nanofiber embedded in a hot rubidium vapor. *Phys. Rev. Lett.*, 100:233602, 2008.

[157] J. M. Goldwin. *Quantum Degeneracy and Interactions in the $^{87}Rb -^{40} K$ Bose-Fermi Mixture.* PhD Thesis, 2009.

[158] H. A Wheeler. Simple inductance formula for radio coils. *Proceedings of the Institute of Radio Engineers*, 16:1398, 1928.

[159] O. Chubar, P. Elleaume, and J. Chavanne, 1997. Radia Software (Version 4.1) [Computer software]. Retrieved from http://www.esrf.eu/Accelerators/Groups/InsertionDevices/Software/Radia.

[160] C. Schaschke. *Fluid Mechanics: Worked Examples for Engineers.* Institute of Chemical engineers., 2nd edition, 2005.

[161] B. E. Larock, R. W. Jeppson, and G. Z. Watters. *Hydraulics of pipeline systems.* CRC Press, 2000.

[162] C. I. Laidler. *Laser frequency stabilisation and the study of rubidium D2 line, using polarisation spectroscopy and a dichroic atomic vapour laser lock, MPhys Thesis.* 2008. Swansea University - not published.

[163] R.J. Sewell. *Matter Wave Interference on an Atom Chip.* PhD Thesis, 2009. Imperial College London.

[164] J. M. Reeves, O. Garcia, and C. A. Sackett. Temperature stability of a dichroic atomic vapor laser lock. *Appl. Opt.*, 45:372, 2006.